Core reconstruction in pseudopotential calculations

Trail, John Robert

Award date:
1998

Awarding institution:
University of Bath

CORE RECONSTRUCTION IN PSEUDOPOTENTIAL CALCULATIONS

Submitted by John Robert Trail
for the degree of
Doctor of Philosophy
of the University of Bath
1998

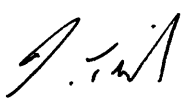

ProQuest LLC
789 East Eisenhower Parkway
P.O. Box 1346
Ann Arbor, MI 48106-1346

Dedicated to my mum

Abstract

Total energy pseudopotential methods are amongst the most powerful techniques currently available for the *ab initio* calculation of the properties of materials. These methods can handle significantly larger systems than other methods of comparable accuracy, and excel at structural optimisation. The pseudopotential approximation effectively describes electron behaviour between atoms accurately, but electrons close to atomic nuclei are either not present or are not represented correctly. An accurate knowledge of the behaviour of electrons in the vicinity of the atomic nuclei is vital for the description of hyperfine interactions and the results of modern spectroscopy techniques.

This thesis presents a new method for obtaining all-electron results from a pseudopotential calculation by carrying out a localised calculation in the region of an atomic nucleus. This is achieved using the embedding potential method of Inglesfield (1981). In this method the core region is *reconstructed*, and none of the simplifying approximations (such as spherical symmetry of the charge density/potential or frozen core electrons) that previous solutions to this problem have required are made.

In developing the embedding approach a new model calculation is presented for a 1D square well, and a new expression for the embedding potential itself is derived. The embedding method requires an accurate real space Green function, and an analysis of the errors introduced in constructing this from a set of numerical eigenstates is given. This is of particular importance since no account of a similar embedding calculations is available in the literature.

Core reconstructions are presented for Aluminium and Silicon, and for Silicon structure factors are obtained from the reconstruction and compared with extremely accurate experimental X ray diffraction and FLAPW results. The reconstruction results are as accurate as the FLAPW results, and reproduce the residual error between the theoretical and experimental results.

Contents

Acknowledgements vii

1 Introduction 1
- 1.1 *ab initio* methods . . . 2
- 1.2 Hyperfine Interactions . . . 4
  - 1.2.1 Electrostatic Hyperfine Interaction . . . 4
  - 1.2.2 Magnetic Hyperfine Interaction . . . 6
  - 1.2.3 Core Electron Effects . . . 8
  - 1.2.4 Why is a new calculation procedure necessary? . . . 8
- 1.3 Previous Work . . . 9
- 1.4 Embedding . . . 11
- 1.5 Core Reconstruction using Embedding . . . 13

2 The Embedding Method 15
- 2.1 An Embedding Potential . . . 18
  - 2.1.1 The Embedded Hamiltonian . . . 18
  - 2.1.2 Alternative Forms of the Embedding Potential . . . 22
- 2.2 Embedding Calculation for a $1D$ Square Well . . . 26
  - 2.2.1 Bound States . . . 28
  - 2.2.2 Propagating States and Resonance States . . . 31
  - 2.2.3 Embedding in a Kronig-Penney Potential . . . 35
- 2.3 Conclusion . . . 37

3 Green functions from Plane-wave Pseudopotential Calculations 39
- 3.1 Introduction . . . 39
- 3.2 Density Functional Theory and the Pseudopotential Method . . . 40
  - 3.2.1 The Local Density Approximation . . . 42
  - 3.2.2 Plane Wave Basis Set . . . 43
  - 3.2.3 Pseudopotential Methods . . . 43
  - 3.2.4 Total Energy Pseudopotential Calculation . . . 47
- 3.3 Obtaining the Green Function . . . 48
  - 3.3.1 Spectral Representation for Bloch States . . . 50
  - 3.3.2 The Pseudo-States Expanded in Spherical Harmonics . . . 51
- 3.4 Brillouin Zone Integration . . . 52
  - 3.4.1 Applying Symmetry to Reduce the Volume of Integration . . . 52
  - 3.4.2 Discretisation of the Integral over the Irreducible Wedge . . . 56
  - 3.4.3 Zero Order Integration Scheme . . . 57

3.4.4 Continuity in Energy Space: Linear Interpolation in **k** Space and the Spectral Function . . . 59
3.4.5 The Linear Analytic Tetrahedron Method . . . 61
3.4.6 Convergence with $n_{\mathbf{k}}$: Band Crossing and van Hove Singularities . . . 64
3.5 The Green Function from the Spectral Function . . . 68
3.5.1 The Convolution Integral . . . 68
3.5.2 Errors Due to the Polynomial Interpolation of $\mathcal{F}$ . . . 71
3.5.3 Convergence for a Free Electron Green Function . . . 72
3.6 Conclusions . . . 74

4 The Green Function and Embedding Potential 76
4.1 Introduction . . . 76
4.2 Completing the Incomplete Set of States . . . 77
4.2.1 Error Term for a Free Electron Gas . . . 77
4.2.2 Error Correction Term for the Incomplete Spectral Representation . . . 82
4.3 Convergence Properties . . . 84
4.3.1 The Total Energy Pseudopotential Calculation . . . 84
4.3.2 Energy Cutoff for Basis Set, E_{max} . . . 85
4.3.3 Number of **k** Points, $n_{\mathbf{k}}$ . . . 86
4.3.4 $\mathcal{G}$ from $\mathcal{F}$ - the Convolution Integral . . . 87
4.4 Embedding Potential from the Plane Wave Pseudopotential Calculations . . . 92
4.4.1 Γ from $\mathcal{G}$ . . . 92
4.4.2 Influence of Convergence of G on Γ . . . 93
4.4.3 Effect of Including Only a Subset of Bands . . . 99
4.4.4 Convergence with Matrix Dimension . . . 102
4.5 Conclusion . . . 104

5 Embedded All-Electron Calculation 105
5.1 Introduction . . . 105
5.2 The Embedded All-electron Calculation . . . 106
5.2.1 The Embedded Hamiltonian . . . 107
5.2.2 The Embedded Green function and Local Density of States . 110
5.2.3 The Charge Density . . . 110
5.2.4 Self Consistency . . . 113
5.3 Results . . . 116
5.3.1 Core Reconstruction for Aluminium and Silicon . . . 117
5.3.2 Embedding with a Pseudopotential . . . 124
5.3.3 Original Pseudo and Reconstructed DOS . . . 126
5.3.4 Core States . . . 127
5.3.5 Is an aspherical calculation necessary? . . . 128
5.4 Convergence . . . 129
5.4.1 Energy Cutoff . . . 130
5.4.2 Brillouin Zone Integral . . . 131

5.4.3 The Convolution Integral . . . 132
5.4.4 Size of Embedding Potential Matrix . . . 135
5.4.5 Effect of Including Only Low Energy Bands in Γ . . . 138
5.5 Silicon Structure Factors . . . 140
5.5.1 Structure Factors from Charge Densities . . . 140
5.5.2 Comparison with Experimental Results and FLAPW Calculations . . . 143
5.5.3 Static Structure Factors . . . 144
5.5.4 Experimental, FLAPW and Reconstructed Structure Factors 145
5.6 Conclusions . . . 150

6 Conclusions **152**
6.1 Overview . . . 152
6.1.1 Embedding Potential Method . . . 154
6.1.2 The Embedding Potential . . . 154
6.1.3 Reconstruction of Correct All Electron States . . . 155
6.1.4 Results . . . 156
6.1.5 Computational Cost and Applicability to Larger Systems . . 157
6.2 Applications . . . 159
6.3 Future Applications and Further Work . . . 159

A Symmetrisation Matrices **162**

Bibliography **164**

List of Figures

2.1 Region I embedded in substrate II. 15
2.2 Square well 26
2.3 Expectation value of the energy 29
2.4 Expectation value of the energy 30
2.5 Zeroes of the Wronskian 34
2.6 DOS within square well for deepening well. 36
2.7 Potential for substrate and embedded all-electron atom 38

3.1 DOS for Aluminium and Silicon 49
3.2 Band structure for Aluminium and Silicon 49
3.3 FCC Brillouin zone 49
3.4 Free electron $\mathcal{G}_{(00,00)}$ from the zero order method. 59
3.5 One tetrahedron used for the tetrahedron integration method. . . . 63
3.6 Band structure near a degeneracy. 65
3.7 Free electron spectral function for bands ordered by energy or by associated reciprocal lattice vector. 66
3.8 Moments of the Hilbert kernel. 70
3.9 Free electron Green function from tetrahedron method. 72
3.10 Convergence of free electron Green function with $n_{\mathbf{k}}$. 73

4.1 Spatial variation of the normal derivative of the free electron Green function. 78
4.2 Error in Green function due to finite E_{cut}. 80
4.3 Error in normal derivative of Green function due to finite E_{cut}. . . . 80
4.4 Error in free electron Green function as a function of E_{max}. 81
4.5 Region of reciprocal space occupied by basis set 82
4.6 Convergence of Aluminium Green function with cutoff energy . . . 85
4.7 Convergence of Aluminium Green function with $n_{\mathbf{k}}$. 86
4.8 Convergence of Silicon Green function with $n_{\mathbf{k}}$. 87
4.9 Convergence of Aluminium Green function with ΔE. 88
4.10 Convergence of Silicon Green function with ΔE. 88
4.11 Silicon Green function for linear and cubic interpolation of spectral function. 89
4.12 Aluminium Green function for analytic and numerical 'topping up'. 90
4.13 Aluminium $\Gamma_{(00,00)}$ for different E_{max} 95
4.14 Convergence of Aluminium embedding potential with cutoff energy 95
4.15 Convergence of Aluminium embedding potential with $n_{\mathbf{k}}$ 96

4.16 Convergence of Silicon embedding potential with $n_{\mathbf{k}}$ 97
4.17 Convergence of Aluminium embedding potential with ΔE. 98
4.18 Convergence of Silicon embedding potential with ΔE. 98
4.19 Silicon embedding potential for linear and cubic interpolation of spectral function. 99
4.20 Convergence of Aluminium embedding potential with number of bands included 102
4.21 Convergence of Silicon embedding potential with number of bands included 102
4.22 Convergence of embedding potential with matrix dimension 103

5.1 Embedding region 107
5.2 Contour paths for integral over occupied states. E_0 is below the bottom of the 1^{st} band, and E_f is the Fermi energy. 111
5.3 Valence charge densities for all-electron reconstruction. 120
5.4 Valence charge densities for all-electron reconstruction. 120
5.5 Unit cells for Al and and Si. 121
5.6 Valence charge densities for pseudopotential reconstruction. 125
5.7 Valence charge densities for pseudopotential reconstructions 125
5.8 Reconstructed and original DOS 127
5.9 Silicon core charge densities. 127
5.10 Charge density isosurfaces. 129
5.11 Convergence of $\rho(\mathbf{r})$ with E_{max}. 130
5.12 Convergence of $\rho^{val}(\mathbf{r})$ with $n_{\mathbf{k}}$ for Al. 131
5.13 Convergence with sampling of spectral function. 133
5.14 Convergence with sampling of spectral function, $\mathcal{F}$, at higher energies. 135
5.15 Convergence of charge density with l_{top} of its expansion. 136
5.16 Contributions to DOS within r_s from different diagonal parts of the Green function matrix. 137
5.17 Convergence with l_{max}. 138
5.18 Convergence with n_{bands} for Si. 139
5.19 Difference between static form factors calculated by reconstruction and FLAPW methods, and the difference between static form factors calculated by pseudo+core and FLAPW methods. 145
5.20 Residual error of FLAPW and reconstructed dynamic form factors, with error bars of experimental data shown. 149
5.21 Residual error of reconstructed dynamic form factors using the spherical part of the reconstructed charge density within the embedding sphere, $f^{recon,spherical} - f^{exp}$. 150

List of Tables

3.1 Moments of the Hilbert kernel. 70

4.1 Number of plane waves/bands for each energy cutoff 85
4.2 Size of **k** point sets in Brillouin zone integration 86

5.1 Parameters used for 'standard' calculation of the embedding potential. 118
5.2 Parameters used for 'standard' reconstruction calculation. 118
5.3 Total charge within embedding sphere, q, for original pseudopotential and reconstruction calculation. 119
5.4 Errors in charge density. 123
5.5 Errors contributed by each l component. 123
5.6 Errors in self consistent potential resulting from reconstruction calculation. 123
5.7 Errors in reconstructed $\rho(\mathbf{r})$ using pseudopotential for reconstruction. 124
5.8 Errors in ignoring aspherical part of ρ. 128
5.9 Errors in ρ for different **k** point sets used to calculate embedding potential - Aluminium. 131
5.10 Number of $\mathcal{F}$ sample points ($\Delta E_1 = 0.1$ eV). 134
5.11 Form factors from reconstruction, FLAPW and pseudopotential calculations. 146
5.12 Dynamic form factors from experiment, reconstruction, FLAPW and Pseudopotential calculation. 148

Acknowledgements

I would like to thank Professor David Bird; his enthusiasm and knowledge have been an inspiration, and I could not have hoped for a better supervisor. Many thanks also to Dr Simon Crampin for providing the original code that the all-electron calculation evolved from, and useful discussions on the embedding method.

I would like to express my gratitude to the EPSRC for funding this PhD.

Thanks to all the theory boys, and everybody else on level 5 for the coffee, the beer and the talk (some of which was even about physics), and finally, a big thank you to Linda for her support and smiles.

embed or sometimes **imbed** *im-bed*, *vb* to place, set or plant firmly in a mass of matter (also *fig*); to lay, as in a bed; to enclose deeply or snugly. - *n* **embedding** (*biol*) the technique in which specimens are embedded in a supporting medium, such as paraffin wax or epoxy resin, in preparation for sectioning with a microtome. - *n* **embedment** the act of embedding; the state of being embedded. [**em-** (from **en-**)]

The Chambers English Dictionary, 1994

Chapter 1

Introduction

The accurate description and prediction of quantum phenomena is becoming increasingly important for the interpretation of a large range of experimental work, and for the development of technologies based on this work. New methods and refinements of existing methods for probing the behaviour of matter on the quantum scale place ever increasing demands on the theoretical models required to explain these experimental results. Another way to view this is that accurate experimental data allows the validation of theoretical methods for the calculation of properties of materials, giving confidence to further predictions made from theory.

As a consequence of this the development of flexible and powerful methods for the *ab initio* calculation of complex systems is vital to increase the understanding and control of these new systems. Examples of fields requiring the development of new theoretical methods include the accurate description of defects in semiconductor physics (this is becoming especially important since the size of semiconductor devices is approaching the quantum scale), surfaces and their catalytic properties, Scanning Tunnelling Microscopy (STM), and a whole host of spectroscopic methods.

A powerful experimental tool for probing solid state materials is to examine the interaction of the atomic nuclei within the materials with the electrons - the *hyperfine interaction.* The energy levels of the nucleus of an atom are shifted by this interaction, and this shift can be measured accurately. Since this is a *local* interaction, this yields information about the local structure of the material and can provide vital information about the nature of defects in a material, or defects and adsorbed atoms on a surface. The combination of accurate experimental and

theoretical methods for this type of problem would improve our understanding of catalysis and the role that defects play in solid state physics generally.

Examples of the experimental methods for probing this hyperfine structure include (see Kaufmann and Vianden, 1979):

- Mössbauer spectroscopy. Recoilless gamma-ray emission from a radioactive nucleus (there is a finite probability of this occurring) implies that the emitted gamma-ray has the energy of the nuclear transition, with no deficit due to nuclear recoil. This transition energy can then be measured.
- Nuclear Quadrupole Resonance (NQR), and Nuclear Magnetic Resonance (NMR). The absorption profiles for a radio frequency electromagnetic field can be directly measured, yielding information on the shifts in the nuclear energy levels due to hyperfine interactions. This method requires sensitive spectroscopy, and a large number of target nuclei are required for accurate measurements, hence is not applicable to characterising defects and adsorbates at their normal concentrations.
- Perturbed Angular Correlation (PAC). A set of methods relying on the anisotropic scattering properties of spin aligned atomic nuclei, which are influenced by the hyperfine interaction.
- Electron Nuclear Double Resonance (ENDOR). A more complex method involving the interaction of excited electron spin states and nuclear spin states (Gemperle and Schweiger, 1991).

1.1 *ab initio* methods

The exponential growth in available computing power, and the development of efficient and fast methods has increased the range of problems addressable using *ab initio* methods. Pseudopotential methods and total energy minimisation calculations (Payne et al, 1992) have dominated in many fields, and provide a flexible and powerful tool for handling large complex systems theoretically. These methods allow the forces within a lattice to be calculated cheaply, so have become the standard method for structural optimisation. They also are not limited to crystalline materials, since they are powerful enough to handle other structures (surfaces,

adsorbates, isolated atoms) using super-cell methods. Typically the total energy pseudopotential methods can accurately handle systems at least $\sim 10\times$ larger than other methods, for a given accuracy.

An important deficiency of the pseudopotential approach is that although it describes the interaction between atomic nuclei, the description of the electrons near atomic nuclei is hopelessly incorrect (no core electrons are included and the valence electrons have a different structure in this region). This appears to prevent the application of this approach to the prediction of hyperfine interactions (these effects are strongly dependent on the local environment of the nuclei) and preclude the accurate calculation of hyperfine structure for large systems. This also prevents the use of pseudopotential methods to predict properties of materials that depend on the spatial distribution of electrons, such as structure factors resulting from X-ray diffraction experiments.

Other methods are available that calculate the states of *all* the electrons in the system, such as the Full-potential Linearised Augmented-Plane-Wave (FLAPW) method (Anderson, 1975; Koelling and Arbman, 1975). FLAPW provides the states for all-electrons present in the system accurately, but is considerably more computationally expensive than the pseudopotential method. A host of other all-electron methods are available, such as Linear Muffin Tin Orbital (LMTO) (Anderson, 1975), KKR Green function (Korringa, 1947; Kohn and Rostocker, 1954) and Tight Binding (TB) (Goringe et al, 1997) methods, but these are limited in their accuracy and generally only provide sufficiently accurate results for a small class of problems and materials - they tend to be specialised methods. FLAPW not withstanding all of these methods are less accurate that the pseudopotential method.

Recently new generalisations of existing methods have been developed that could well bridge the gap between the all-electron and pseudopotential methods. Blöchl (1994) describes a Projector Augmented Plane wave method, a generalisation of both the pseudopotential and FLAPW methods (in the sense that both of these can be obtained from the PAW methods as approximations to it), that provides the all-electron wave-functions for significantly less computational effort than the FLAPW methods, and retains much of the analytic simplicity of the pseudopotential method. This has been implemented by Holzwarth et al (1997) for a number of simple materials, and provides an accuracy as good or better than equivalent FLAPW and pseudopotential results. A full potential implementation of

the LMTO method (LMTO-FP) has also been implemented by Methfessel et al (1989) for Si, and this appears to perform well (again in comparison with FLAPW and pseudopotential results). In addition the LMTO-FP method allows limited structural optimisation, which cannot be included within the normal formulation of the LMTO method. However, for both of these methods the only comparisons reported in the literature are of structural parameters (cohesive energy, equilibrium lattice constants and bulk moduli) hence it is difficult to draw conclusions about how generally applicable these methods are, and the accuracy of the electron structure predicted from them. The scaling behaviour with system size has also not been investigated, hence it seems likely that these methods will be fairly limited in their application until they have been properly validated. In view of the fact that the pseudopotential method is known to provide accurate results for a large range of materials, and the conditions under which the approximation breaks down are well understood, it is desirable to extend the applicability of the pseudopotential method to all-electron systems.

1.2 Hyperfine Interactions

Past work on predicting hyperfine interactions has generally relied on cluster calculations for ionic systems and the LMTO method (either the TB formulation or using the Atomic Sphere Approximation (ASA) - the ASA is the approximation removed by the LMTO-FP approach (see Methfessel et al, 1989)) for metals and semiconductors. FLAPW methods have also recently been applied to these problems. In this section a brief review of hyperfine interactions is given, and expressions presented for the nuclear energy level shifts. Some typical examples of previous work on predicting hyperfine interactions are also described.

1.2.1 Electrostatic Hyperfine Interaction

Atomic nuclei generally are not spherical, and so possess an electrostatic quadrupole moment, Q. Due to this an interaction occurs between the nucleus and the electric field it is placed within (due to the rest of the system) and splitting of the energy levels of the nucleus occurs. This splitting only takes place if the gradient of the electric field (a second order traceless symmetric tensor) is non-zero at the nuclear site. Due to symmetry considerations this can only occur for non-cubic point group

symmetry (Kaufmann and Vianden, 1979). As a consequence of this sensitivity to the symmetry and local environment of the ion, the energy shift provides information about the structure of point defects in materials where the symmetry is broken locally, information about defects and adsorbates on surfaces, and for non-cubic systems a direct method for measuring the quadrupole moment of the nucleus (provided the local electric field is known).

This splitting corresponds to a transition frequency, ν_q given by

$$\nu_q = \frac{eQ|V_{zz}|}{2h}\sqrt{1+\frac{\eta^2}{3}} \tag{1.1}$$

where e is the electronic charge and h is Planck's constant (see Seeger et al, 1996). The parameters V_{zz} and η describe the electric field gradient tensor - the traceless tensor has components

$$V_{zz} > V_{yy} > V_{xx} \tag{1.2}$$

(the axes are chosen for the tensor to be symmetric and for this ordering to be true) and η is defined as

$$\eta := (V_{xx} - V_{yy})/V_{zz}. \tag{1.3}$$

Since the tensor is traceless it is entirely characterised by V_{zz} and η. The field gradient tensor can be expressed in terms of the charge density as

$$\begin{aligned} V_{ij} &= \frac{\partial^2 V}{\partial x_i \partial x_j} \\ &= \int \rho(\mathbf{r})\left(\frac{3x_i x_j}{r^5} - \frac{\delta_{ij}}{r^3}\right) d^3\mathbf{r} \end{aligned} \tag{1.4}$$

which depends only on the $l = 2$ components of the charge density. It should be noted that the charge density in equation (1.4) includes the contribution from the nuclei around the nucleus of interest.

From this it is apparent that to obtain the EFG tensor accurate knowledge of the $l = 2$ part of the charge density is required. Past methods used to obtain the EFG have fallen into two main classes. For ionic materials the point ion approach can be applied, where the EFG is approximated as a sum of contributions from the surrounding ions within the system. Wei and Zunger (1997) have shown that this gives inaccurate results even for strongly ionic systems, with up to 95 % of the EFG being due to the charge density close to the ion and not taken into account by the point ion approach. This method can be extended by carrying out a cluster

calculation for a manageable number of atoms, and surrounding this with point ions. This is the approach taken by Petrilli and Frota-Pessôa (1990) for HCP Zr, and has the advantage of being applicable to aperiodic systems. However, the method is a Linear Muffin Tin Orbital (LMTO) tight binding method so is limited to systems described well by a tight binding Hamiltonian and cannot approach the accuracy of pseudopotential methods. A similar approach has been taken by Mitchell et al (1996) to assess the EFG at ionic sites in the spinels $ZnAl_2O_4$ and $ZnFe_2O_4$, where a Hartree-Fock method was employed for the cluster. Both these approaches are limited in their accuracy.

The current state of the art calculations appear to be Full-potential Linearised Augmented-Plane-Wave (FLAPW) calculations. Dufek et al (1995) present the EFG obtained for a number of ^{57}Fe compounds using FLAPW methods, and by comparison with the results of Mössbauer spectroscopy give a new estimate for the quadrupole moment of the nucleus (significantly different from the previously accepted value). Blaha et al (1996) has carried out FLAPW calculations for a different range of ^{57}Fe compounds using this revised quadrupole moment to compare the FLAPW and experimental EFG. The EFG for a number of ^{100}Rh and ^{77}Se compounds are also compared with experimental results. There results show good agreement with the experimental data, indicating the validity and flexibility of the FLAPW method.

1.2.2 Magnetic Hyperfine Interaction

As well as possessing a quadrupole moment, nuclei also possess spin and this interacts with the spin of electrons in the vicinity of the nucleus, again causing splitting of the previously degenerate nuclear energy levels. For this to occur there must be some spin polarisation present in the electron population (for the nuclear spin to have something to interact with) hence the splitting will depend on the parameters of the nuclear spin, and the spin polarisation of the electron population. The Hamiltonian for this interaction is made up of two distinct parts - an isotropic part (the contact interaction), and an anisotropic part. The general expression for the spin interaction Hamiltonian of an electron at $\mathbf{r}$ with a nucleus at $\mathbf{R}$ is

$$\mathcal{H} = \mathbf{S}^e \cdot \mathbf{A} \cdot \mathbf{S}^I \tag{1.5}$$

where $\mathbf{S}^I$ and $\mathbf{S}^e$ are the spin operators for the nucleus and electron, and $\mathbf{A}$ is the hyperfine interaction tensor which describes the coupling between the electron and nuclear spin at site $\mathbf{R}$. The components of $\mathbf{A}$ are given by $A_{ij} = a\delta_{ij} + b_{ij}$, where

$$\begin{aligned} a &= \frac{8\pi}{3}\mu_0 g_e \mu^e g_I \mu^I \rho^s(\mathbf{R}) \\ b_{ij} &= \mu_0 g_e \mu^e g_I \mu^I \int \rho^s(\mathbf{r}) \left(\frac{3x_i x_j}{r^5} - \frac{\delta_{ij}}{r^3} \right) d^3\mathbf{r}. \end{aligned} \tag{1.6}$$

μ_0 is the susceptibility of free space, g_e and g_I are the g-factors for the electron and nucleus, and μ^e and μ^I are the electronic and nuclear magneton respectively. The spin charge density, $\rho^s(\mathbf{r})$ is given by $\rho^s(\mathbf{r}) = \rho_\uparrow(\mathbf{r}) - \rho_\downarrow(\mathbf{r})$, the difference between the charge density of spin-up and spin-down electrons. Equation (1.6) tell us that provided there is spin polarisation at the nucleus, we can calculate the contact hyperfine interaction, and that provided we know the $l = 2$ part of the spin charge density we can calculate the anisotropic part.

There is a good deal of similarity between this and the nuclear quadrupole interaction, and measuring the magnetic hyperfine interaction is useful for the same reasons. Measuring the magnetic hyperfine interaction is particularly applicable to systems where local spin polarisation of electrons occurs, such as for transition metal impurities in semiconductors.

Much of the previous work to calculate the magnetic hyperfine interaction has concentrated on LMTO methods. Weihrich and Overhof (1996) use an LMTO method for Silicon, then add an interstitial Fe via a Green function technique employing Dyson's equation, and Illgner and Overhof (1996) have also applied the LMTO method to group 4 donors, vacancies and cation self interstitials in II-VI compound semiconductors. Battoceli et al (1996) use KKR-LMTO methods to obtain the hyperfine interactions in ferromagnetic Fe, Co and Ni. They compared the results using different approximations for the exchange-correlation potential, finding little or no influence on the calculated hyperfine field. All of these LMTO calculations are limited to only being accurate for a small number of systems, if at all, as described for the EFG calculations. Some calculations have also been carried using FLAPW within the LSDA approximation, such as Katayama-Yoshida and Hamada (1987), but these suffer the same constraints as for the EFG calculations.

1.2.3 Core Electron Effects

Another area of interest for the *ab initio* description of materials are core electron effects. The core states of the atoms that make up a structure are often presumed to be frozen to the free atom states - this is the starting point for many calculational procedures including the LMTO and pseudopotential methods, and many applications of the FLAPW method. However for real systems the core may relax, and the energy of the core states shift (relative to one another) from the free atom values. This can be a useful tool for the investigation of complex systems where information of the local environment of the atom is required.

For example, Ganduglia-Pirovano et al (1997) perform some fully core relaxed LMTO calculations to obtain the difference in core level energies for transition metals forming a clean surface and a surface alloy. They find a correlation between shifts in the d band and core electron energy level shifts, which is important since the position of the d band can be a key factor in determining the chemical reactivity of the surface. Compton scattering is another area where accurate all-electron states for a material are vital to reproduce experimental results. Bellaiche and Kunc (1997) have derived Compton profiles for LiH by pseudopotential methods, and by an all-electron plane wave basis calculation (feasible for this small system). The all-electron calculation results agree well with experimental data, whereas the pseudopotential results do not. Another approach tested by the same workers was to orthogonalise the valence electron states to the free electron core states before deriving the Compton profile from these states. Although this improved agreement it still did not come close to reproducing the accuracy of the all-electron calculation, which they attributed to deficiencies in the pseudopotential method. They also found that significant core relaxation did occur, for this system at least.

1.2.4 Why is a new calculation procedure necessary?

None of the methods described above can come close to handling systems as large as pseudopotential methods, and most have additional deficiencies. All of these methods (FLAPW and LMTO-FP notwithstanding) make assumptions about the physics of the system that, in many cases, cannot be justified (such as a spherical potential in the core region, the TB approximation or the ASA). The FLAPW and LMTO-FP are generally applicable, but are too computationally expensive for larger systems and do not allow efficient structural optimisation to be implemented.

In view of this it is desirable to extend the pseudopotential method by adding an extra step after the pseudo-system has been solved. This would allow all the strengths of the total energy pseudopotential method to be exploited, but still provide all-electron (in other words full potential) results. Once an accurate pseudopotential total energy calculation has been performed it would be desirable to choose the atom for which we require the core and correct valence states, and *reconstruct* the correct states. Since one atom is a simple system to solve, it would be hoped that solving for one atom with different boundary conditions on a sphere surrounding it (this is what the problem reduces to) would be fairly straightforward. However, a number of difficulties quickly present themselves. The purpose of this thesis is to describe and validate a new procedure for carrying out this *core reconstruction* that makes the same *physical* approximations as the FLAPW method (so could be expected to provide the same accuracy).

1.3 Previous Work

Reconstructing the correct eigenstates from pseudo-states has been addressed by several workers. In their paper Gardner and Holzworth (1986) reconstruct the correct states for an isolated atom from the pseudo-atom, by applying direct integration, effectively 'inverting' the pseudopotential (Si and Ru are the atoms they choose). They obtain good results, showing that this reconstruction approach is at least possible. However, the situation for reconstructing states for an atom in a lattice is considerably more complex. For an isolated atom only discrete states are present, but for the atom within a lattice the valence states form a continuum, so the reconstruction must be fitted into the band structure of the lattice. In addition to this, for an isolated atom the potential is spherically symmetric, whereas for an atom within a lattice this is not the case. In their reconstruction they have also assumed that the core is frozen, an approximation that it would be preferable to avoid.

Vackář and Šimůnek (1994) describe a method for reconstructing the states for a pseudo-atom within a lattice. Again this relies on direct integration and assumes the charge density, boundary conditions and self-consistent potential are spherically symmetric, although the core states are allowed to relax. The errors in the resulting eigenfunctions are fairly large, although they do obtain the correct nodal form for the eigenstates. It should also be noted that the wavefunctions calcu-

lated are not Bloch wavefunctions, but atomic-like wavefunctions corresponding to a charge density that matches the crystalline charge density at a certain radius, hence the physical interpretation of the reconstruction is unclear.

Kuzmiak et al (1991) perform a pseudopotential calculation, and orthogonalise the resultant pseudo-states to the original core states. This would work perfectly for the original formulation of pseudopotential methods, where the pseudopotential was defined in this way, but for modern pseudopotentials this does not give the correct solution to the problem and the errors present are difficult to control or even quantify.

The most complete solution to the problem presented so far is that due to Meyer et al (1995). In their method the correct states are reconstructed within a reconstruction sphere (a spherical region centred on the atom of interest that contains the region where the all-electron and pseudo valence states differ) by direct integration, but taking boundary conditions for both the potential and electron states into account correctly. In order to decouple the radial wave equations for the reconstruction calculation they do make the assumption of spherical symmetry of the self consistent potential, but asymmetric boundary conditions for the valence states are allowed. Within their scheme the core is still frozen.

With the exception of Vackář and Šimůnek, all of these methods require the reconstruction to be performed for each $\mathbf{k}$ point in the Brillouin zone and for each band (in other words for each Bloch state), in order to construct the charge density required for the EFG or hyperfine interaction parameters. This is computationally expensive, and none allow relaxation of the core electrons. This thesis describes a new method for performing this kind of core reconstruction that does not make any of the arbitrary assumptions of the methods developed before - these assumptions have generally been made only to allow the problem to be reduced to a simpler form that can be solved with existing methods, and can only be justified *a posteriori*. The method presented here follows a completely different path to achieving the reconstruction, and:

- Does not require spherical averaging of the self-consistent potential.
- Provides an aspherical charge density (vital for the description of hyperfine interactions).
- Does not assume a frozen core - core states are relaxed.

- Does not require construction of individual states for each **k** point within the Brillouin zone.

Provided the reconstruction is carried out to sufficient numerical accuracy and the pseudopotential method is valid, the reconstruction method given in this thesis should be as good as FLAPW calculations (the *physical* approximations made in each method are very similar), whilst allowing all the advantages of the pseudopotential method to be exploited.

1.4 Embedding

The approach taken in this thesis is the *embedding* approach, as formulated by Inglesfield (1981). The idea can best be illustrated by an example. Consider the problem of solving for the electronic states of a vacancy within a crystal lattice. For a periodic lattice the electronic states can be found with familiar **k** space methods, but the introduction of a vacancy by removing an atom destroys this periodicity, so these methods are no longer valid. However, if we could solve for the states of the perfectly periodic system and then carry out a separate localised calculation at the vacancy *that takes into account the potential in the rest of the lattice in some way using the eigenstates of the perfect lattice*, then we would have achieved something. This 'divide and conquer' approach has reduced the solution of one difficult problem to that of two simpler problems [1]. In this example the vacancy is *embedded* into the periodic lattice (the *substrate*).

This kind of problem could of course be solved using perturbation theory if the difference between the potential at the vacancy and the atom it replaced was small enough, but this is unlikely to be the case. Embedding methods essentially provide a means to carry out this breakdown of the problem exactly, with no approximations necessary (until the method is actually implemented). It should be noted that embedding does not correspond to matching logarithmic derivatives of wave functions in the trial region with the previously calculated wavefunctions of the substrate region - these substrate wavefunctions are unlikely to still be eigenvalues of the whole system when part of the substrate potential has been replaced within the embedded region. Embedding corresponds to matching the

[1] For a real system the relaxation of the lattice around the vacancy would also have to be considered.

wavefunctions within the embedded region to a *generalised logarithmic derivative* that is defined for all energies of the wavefunction.

Inglesfield (1981) developed a method of solving exactly this kind of embedding problem for any shape or size of embedding region embedded in a substrate by deriving an *energy dependent embedding potential* for the substrate. This is simply a potential that, when added to the Hamiltonian for the localised embedded region, entirely takes into account all of the combined system outside of the embedded region. Chapter 2 describes this in some detail with particular emphasis on the physical interpretation of the method. In addition to this a new analytic form for the embedding potential itself is presented. It should be emphasised that the embedding approach can be applied to many different problems, for instance a surface can be created by embedding semi-infinite free space into a crystalline substrate, or if a surface is available an adsorbate could be embedded onto the surface.

The main difficulty in implementing this method is obtaining the embedding potential of the substrate system. This requires the time independent single particle Green function of the substrate system to be known accurately in real space (representations using finite basis sets are not directly applicable - this point will be discussed further in chapters 2 and 4). Although it is straightforward to extract the Green function from some solid state methods (eg KKR-Green function methods - see Miller et al (1985) and Inglesfield (1981)) these are the least accurate methods, and for more modern methods the step from calculated eigenstates to accurate real space Green function is not trivial. It for this reason that the majority of studies using the embedding method have used a jellium substrate where the analytic form of the Green function is known (Montalenti et al, 1996; Andriotis, 1990), or arbitrary model Green functions constructed to possess some of the same analytic properties as real systems (Ness and Fisher (1997)).

One notable exception to this is the construction of a surface for the study of surface states. Crampin et al (1992) and Ishida (1997) describe how surface states can be constructed using the embedding method for realistic systems, using an *ab initio* embedding potential to implement a self consistent iterative method.

The only application of the embedding potential method using *ab initio* methods are the KKR calculations of Miller and Inglesfield (the Green function is readily available for these systems) and the surface calculations of Crampin and Ishida (the geometry helps to simplify the calculation). In view of this it is apparent that

obtaining the accurate real space Green function from a plane wave pseudopotential calculation may well be difficult.

1.5 Core Reconstruction using Embedding

The recipe used here to reconstruct the core states proceeds along the following path:

- Carry out a plane wave pseudopotential calculation for the material being investigated.
- From the resulting eigenstates construct an embedding potential surrounding the atom of interest within the material - any atom within the unit cell can be chosen for the reconstruction.
- Carry out a *localised* all-electron calculation with the embedding potential to obtain the correct (non-pseudo) solution.
- Use the results of this embedded calculation to predict the quantity of interest - structure factor, EFG etc.

The method as implemented here does not make any arbitrary assumptions about spherical symmetry of potentials or charge densities, does not rely on a frozen core and is fairly efficient computationally (obtaining the all-electron charge density for bulk Si takes $\sim$ 2 hours from start to finish on a modest workstation). The computational cost of the method should also scale well with increasing system size, although this has not yet been demonstrated.

Chapter 2 concentrates on the embedding method itself, and a new study of a simple model system is presented. Chapters 3 and 4 describe the calculation of the embedding potential from the original plane wave pseudopotential calculation. A number of techniques applied to other problems in the literature are brought together and used to construct the Green function, and an analysis of the errors introduced by the method and corrections for these errors are also presented. This provides a scheme for the accurate calculation of Green functions and embedding potentials from plane wave basis eigenstates. The convergence behaviour of both

the Green function and embedding potentials are also examined for bulk Al and Si.

Finally, in chapter 5 the embedded core reconstruction calculation itself is described, with results presented for Aluminium and Silicon. Again, the convergence and accuracy of these results is analysed. The reconstructed Si core region is then used to calculate structure factors for comparison with data from X-ray diffraction experiments (for Si extremely accurate values are available in the literature) and with recent FLAPW results.

The method presented provides an accurate and consistent application of pseudopotential methods to all-electron problems, with an accuracy as good as FLAPW methods. In addition to solving the core reconstruction problem, the methodology developed for the construction of the Green function from plane wave eigenstates could be applied to other problems, and the whole structure of the core reconstruction calculation is a good starting point for solving other problems using embedding, such as defects in semiconductors and alloys, and adsorbates on surfaces.

Chapter 2

The Embedding Method

A powerful set of methods that rely heavily on the properties of Green functions are *embedding methods.* An embedding method can be described as solving for the system in a subdomain of space (whether real space or Hilbert space) where the influence of the system outside of this subdomain is taken into account from a previous solution, and is *not* recalculated. Expressing this more succinctly and introducing a few terms, it can described as follows - figure 2.1 shows the geometry.

- A substrate system is solved over all space. This is chosen to be some system that can be solved for, whereas the combined system cannot.
- This region is divided into two regions - the embedding region I and region II.

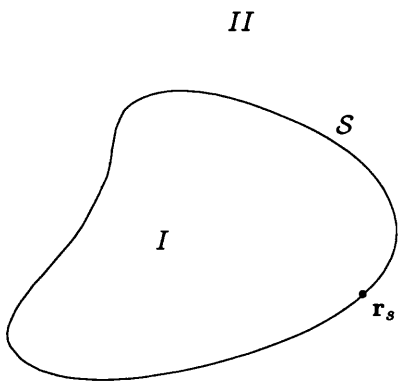

Figure 2.1: Region I embedded in substrate II.

• The solution in region I is then calculated for this region being different from the original region I (for a different potential in this region) whilst taking into account the unchanged potential in region II.

An example of an application would be calculating the states of a local defect in a crystal lattice. First a calculation would be carried out for the perfect crystal using the well established and accurate methods available for this problem. A defect would then be introduced within the embedding region I and the electron states calculated within this sub-domain.

Another application would be to obtain surface states from a bulk lattice calculation. For this case region I would be a semi-infinite vacuum region stretching to infinity, and region II the bulk lattice.

Embedding methods have a strong advantage over more standard super-cell and cluster calculations. Cluster calculations do not produce continuum states as an infinite system is not actually being solved for, and super-cell methods inherently result in continuum states as a localised perturbation is modelled as a periodic lattice of perturbations. For cluster calculations this can require unrealistically large clusters to approximate states of the real infinite system, limiting their applicability. For super-cell calculations this causes no problem provided the super-cells are big enough (the 'discrete' states are represented by extremely narrow bands), but this is often impractical due to computational cost.

The embedding technique gives the solution of an infinite system with a localised perturbation exactly, and this perturbation need not be small - it need only be localised. However, the major limiting factor in the applicability of embedding methods is that the embedding region I must be large enough to encompass any change caused by the embedded perturbation. Changes in the external potential that an electronic gas is subjected to may be localised but the relaxation of the charge density can be more widespread. This may extend some way out from the defect or into the surface, and if this disturbance spreads outside of the embedding region then the substrate system will have changed if the potential is dependent on the charge density as is the case for density functional methods.

A number of different schemes for performing embedded calculations have been presented in the literature. These are based on the application of Dyson's equation within the embedding region (e.g. Braspenning et al, 1984) or a partitioning of the Hamiltonian into 'subspaces' (e.g. Allen and Mennon, 1986). A full discussion

of methods of embedding for surface and defect problems is given by Fisher (1988) where a review is given of available methods and their advantages and deficiencies.

In this work Inglesfield's *embedding potential* method is employed (Inglesfield, 1981). In this method an 'embedding potential' is obtained from the substrate system, and added to the Hamiltonian for the embedding region (defined only within this region). This 'embedding potential' ensures that the states of the system in the embedding region satisfy the correct boundary conditions. As has been shown by Fisher (1988) this method does in fact correspond to an exact application of Dyson's equation to the system despite appearances to the contrary.

Inglesfield's method has the advantage that it requires knowledge of the properties of the substrate system *only on the surface separating the embedded and substrate regions.* It also provides an exact solution for the embedded system - for the specified potentials in regions I and II (as mentioned above this is not assured if self consistency between the potential and the charge density is required). Inglesfield's method has been applied by many workers to a number of different problems, in the areas of construction of surfaces (Crampin et al, 1992; Benesh and Inglesfield, 1984; Ishida, 1997), defects in simple metals (Inglesfield, 1981; Andriotis, 1990) and semiconductors (Miller et al, 1985) and adsorbates on simple metal surfaces (Trioni et al, 1994; Trioni et al 1996; Montalenti et al, 1996; Ness and Fisher, 1997).

In this thesis Inglesfield's embedding method is applied to the problem of gaining information on the electron states in the core region of an atom from a pseudopotential calculation of a system containing the atom. Total energy pseudopotential methods provide accurate lattice structures and accurate valence electron states in the region between atoms, but within the core region near the atoms the valence states are incorrect and no core states are available. This core region is taken as the embedding region (region I in the above description) and an embedded all-electron calculation in this region (with the core electrons taken as localised) 'reconstructs' the correct valence and core electron states in this region.

In the first part of this chapter the Embedding potential is described and expressions for this potential in terms of the substrate Green function are given. Following this a $1D$ square well potential is examined using the method to investigate how it works for an example system. This is particularly important for energy ranges where the eigenfunctions of the combined (I and II) system form a continuum.

2.1 An Embedding Potential

The extended 'substrate' system is solved for given boundary conditions, and the limited region is then introduced into the substrate system (region I in figure 2.1). The states of a system that has the same potential as the substrate system in region II, but a *different* potential in region I can be obtained via the embedding potential that is calculated from the original substrate system. To obtain the states for region I the embedding potential is added to the Hamiltonian for this region (with the different potential) and the states are obtained for this embedded Hamiltonian. The embedding potential ensures that the appropriate boundary conditions are satisfied at the I-II interface, $\mathcal{S}$. It should be noted that the solutions calculated in I are solutions for the combined system $I + II$.

The embedding potential is a non-local, energy dependent potential and non-zero only on the surface $\mathcal{S}$ of the embedding region. It is calculated from the Green function of the original substrate system.

In what follows a brief description of the derivation of the embedding potential is given, concentrating on the steps important to the rest of this chapter. The complete derivation can be found in the literature (Inglesfield, 1981).

2.1.1 The Embedded Hamiltonian

The derivation of this embedding potential proceeds by finding the expectation value of the energy of a wavefunction $\Phi(\mathbf{r})$, defined in II as the solution of the Schrödinger equation for the substrate at some energy ε, $\psi(\mathbf{r})$, and in I as a trial function $\phi(\mathbf{r})$. This energy is then expressed in a form that is dependent only on ϕ within region I and the Green function in region II with its spatial variables constrained to the surface $\mathcal{S}$.

The variational principle is then applied to the expectation value for the energy to obtain a Schrödinger equation which gives a solution in the region I that correctly matches onto the solution in region II. This is a normal Schrödinger equation with the addition of a potential that acts only at the surface $\mathcal{S}$.

The equation for $\psi(\mathbf{r})$ in II is

$$(-\nabla^2 + V(\mathbf{r}) - \varepsilon)\psi(\mathbf{r}) = 0 \quad \mathbf{r} \in II, \tag{2.1}$$

so the expectation value of the energy (Schiff, 1955) is then given by

$$E = \int d^3\mathbf{r}\Phi^* H\Phi / \int d^3\mathbf{r}\Phi^*\Phi \tag{2.2}$$

where H is the Hamiltonian and the spatial variable is suppressed. Introducing the two functions that make up $\Phi(\mathbf{r})$ explicitly gives

$$E = \frac{\int_I d^3\mathbf{r}\phi^* H\phi + \varepsilon \int_{II} d^3\mathbf{r}\psi^*\psi + \int_S d^2\mathbf{r}_s \left(\psi^*(\mathbf{r}_s)\left.\frac{\partial\phi}{\partial n_s}\right|_{\mathbf{r}=\mathbf{r}_s} - \phi^*(\mathbf{r}_s)\left.\frac{\partial\psi}{\partial n_s}\right|_{\mathbf{r}=\mathbf{r}_s}\right)}{\int_I d^3\mathbf{r}\phi^*\phi + \int_{II} d^3\mathbf{r}\psi^*\psi} \tag{2.3}$$

where the surface integral in the numerator is a consequence of the discontinuity in $\Phi(\mathbf{r})$ at $\mathcal{S}$ and Green's theorem. This surface term can be interpreted as the contribution to the kinetic energy from this discontinuity. Equation (2.3) has been used to allow the application of the variational method with basis functions that are discontinuous over a surface in space (Brownstein, 1995), but here the solution in region II is chosen to match the trial function in amplitude at the surface $\mathcal{S}$, hence

$$\phi(\mathbf{r}_s) = \psi(\mathbf{r}_s) \tag{2.4}$$

is an additional condition used for this derivation. It should be noted that no reduction in generalisation is introduced by requiring this condition to be satisfied since the solution in II is not explicitly described at any point in the derivation.

In order to carry out a calculation localised to region I all explicit dependence of this energy on ψ must be removed. To do this expressions for the integral of ψ over region II and the derivative of ψ at surface $\mathcal{S}$ are required. These can be expressed in terms of the trial function in I (ϕ) on the surface $\mathcal{S}$ and the substrate Green function on $\mathcal{S}$ only, and this is the heart of the embedding potential method.

The first step in doing this is to express $\left.\frac{\partial\psi}{\partial n_s}\right|_{\mathbf{r}=\mathbf{r}_s}$ in terms of $\psi(\mathbf{r}_s)$. This is accomplished using the Green function for region II, defined by

$$(-\nabla_r^2 + V(\mathbf{r}) - \varepsilon)G(\mathbf{r},\mathbf{r}';\varepsilon) = \delta(\mathbf{r}-\mathbf{r}') \quad \mathbf{r},\mathbf{r}' \in II. \tag{2.5}$$

Equation (2.1) is then multiplied by $G(\mathbf{r},\mathbf{r}')$, equation (2.5) by $\psi(\mathbf{r}')$, and the

former subtracted from the latter. Integrating this over II results in

$$\psi(\mathbf{r}') = \int_{II} d^3\mathbf{r} \left(G(\mathbf{r},\mathbf{r}')\nabla^2\psi(\mathbf{r}) - \psi(\mathbf{r})\nabla^2 G(\mathbf{r},\mathbf{r}') \right) \tag{2.6}$$

where the energy dependence of G has been suppressed. By swapping $\mathbf{r}$ and $\mathbf{r}'$ and applying the reciprocity relationship $G(\mathbf{r},\mathbf{r}') = G(\mathbf{r}',\mathbf{r})$ and Green's theorem gives

$$\psi(\mathbf{r}) = -\int_{\mathcal{S}} d^2\mathbf{r}_s \left(G(\mathbf{r},\mathbf{r}_s)\frac{\partial\psi(\mathbf{r}_s)}{\partial n_s} - \psi(\mathbf{r}_s)\frac{\partial G(\mathbf{r},\mathbf{r}_s)}{\partial n_2} \right) \tag{2.7}$$

where the normal derivative of G is with respect to $\mathbf{r}'$ and outward from region I to II.

This can by simplified by choosing the Green function in region II that satisfies the von Neumann boundary condition of zero normal derivative on $\mathcal{S}$, denoted by G_0. This gives

$$\psi(\mathbf{r}_s) = -\int_{\mathcal{S}} d^2\mathbf{r}'_s G_0(\mathbf{r}_s,\mathbf{r}'_s)\frac{\partial\psi(\mathbf{r}'_s)}{\partial n_s}. \tag{2.8}$$

Choosing this particular boundary condition is entirely arbitrary and is made to simplify the derivation. In the next subsection the apparent limitations of this choice are removed. Equation (2.8) can be inverted to give the relation

$$\frac{\partial\psi(\mathbf{r}_s)}{\partial n_s} = -\int_{S} d^2\mathbf{r}'_s G_0^{-1}(\mathbf{r}_s,\mathbf{r}'_s)\psi(\mathbf{r}'_s) \tag{2.9}$$

where G_0^{-1} is defined as satisfying

$$\int_{S} d^2\mathbf{r}''_s G_0^{-1}(\mathbf{r}_s,\mathbf{r}''_s)G_0(\mathbf{r}''_s,\mathbf{r}'_s) = \delta(\mathbf{r}_s - \mathbf{r}'_s) \tag{2.10}$$

and is the inverse of the Green function over the surface $\mathcal{S}$.

Since $\psi(\mathbf{r_s}) = \phi(\mathbf{r_s})$ at the surface, equation (2.9) gives the gradient of the solution in II in terms of the solution in I (both evaluated on $\mathcal{S}$)

$$\frac{\partial\psi(\mathbf{r}_s)}{\partial n_s} = -\int_{\mathcal{S}} d^2\mathbf{r}'_s G_0^{-1}(\mathbf{r}_s,\mathbf{r}'_s)\phi(\mathbf{r}'_s) \tag{2.11}$$

as required. Substituting this in equation (2.3) (and, again $\psi(\mathbf{r}_s) = \phi(\mathbf{r}_s)$) gives an expression for E dependent on region II only in the normalisation factor in the denominator, so the next step is to express this volume integral in terms of a surface integral.

This can be accomplished by a similar application of Green's theorem (see Inglesfield, 1981) to give the expression

$$\int_{II} d^3\mathbf{r}|\psi(\mathbf{r})|^2 = \int_S d^2\mathbf{r}_s \left[\psi^*(\mathbf{r}_s)\frac{\partial}{\partial\varepsilon}\frac{\partial\psi(\mathbf{r}_s)}{\partial n_s}\right]. \tag{2.12}$$

With equations (2.4),(2.11) and (2.12), E can be expressed in terms of the trial function in I and the quantity G_0^{-1} (at the surface $\mathcal{S}$ only) to give

$$E = \left[\int_I d^3\mathbf{r}\phi^*(\mathbf{r})H\phi(\mathbf{r}) - \varepsilon\int_S d^2\mathbf{r}_s\int_S d^2\mathbf{r}'_s\phi^*(\mathbf{r}_s)\frac{\partial G_0^{-1}(\mathbf{r}_s,\mathbf{r}'_s;\varepsilon)}{\partial\varepsilon}\phi(\mathbf{r}'_s) + \right.$$

$$\left.\int_S d^2\mathbf{r}_s\phi^*(\mathbf{r}_s)\frac{\partial\phi(\mathbf{r}_s)}{\partial n_s} + \int_S d^2\mathbf{r}_s\int_S d^2\mathbf{r}'_s\phi^*(\mathbf{r}_s)G_0^{-1}(\mathbf{r}_s,\mathbf{r}'_s;\varepsilon)\phi(\mathbf{r}'_s)\right]\Big/$$

$$\left[\int_I d^3\mathbf{r}\phi^*(\mathbf{r})\phi(\mathbf{r}) - \int_S d^2\mathbf{r}_s\int_S d^2\mathbf{r}'_s\phi^*(\mathbf{r}_s)\frac{\partial G_0^{-1}(\mathbf{r}_s,\mathbf{r}'_s;\varepsilon)}{\partial\varepsilon}\phi(\mathbf{r}'_s)\right]. \tag{2.13}$$

When E is at a minimum with respect to variations in $\phi(\mathbf{r})$ then the function Φ (ϕ in I and a solution of equation (2.1) that matches ϕ at $\mathcal{S}$) is the best approximation to the actual minimum (an eigenvalue of the Hamiltonian). If E is then minimised with respect to ε then Φ is the *exact* solution of the Schrödinger equation in I and II of energy $E = \varepsilon$.

The condition that E is stationary with respect to small changes $\delta\phi$ gives the equation

$$\left(H + \delta(\mathbf{r}-\mathbf{r}_s)\frac{\partial}{\partial n_s}\right)\phi(\mathbf{r}) +$$

$$\delta(\mathbf{r}-\mathbf{r}_s)\int_S d^2\mathbf{r}'_s\left(G_0^{-1}(\mathbf{r}_s,\mathbf{r}'_s;\varepsilon) + (E-\varepsilon)\frac{\partial G_0^{-1}(\mathbf{r}_s,\mathbf{r}'_s;\varepsilon)}{\partial\varepsilon}\right)\phi(\mathbf{r}'_s)$$

$$= E\phi(\mathbf{r}) \quad \mathbf{r}\in I. \tag{2.14}$$

for ϕ. This equation takes the form of a normal Schrödinger equation with three additional terms - the derivative term and the two surface integrals on the left hand side. These extra terms take the form of a potential that acts only at the surface $\mathcal{S}$.

In deriving equation (2.14) the energy E has not been minimised with respect to variations in ε, hence ε still appears in the effective Schrödinger equation as a free parameter. As a consequence of this the $\frac{\partial G_0^{-1}(\mathbf{r}_s,\mathbf{r}'_s;\varepsilon)}{\partial\varepsilon}$ term is present, a first order correction to the energy at which the Green function is evaluated (for $E = \varepsilon$ this

term is zero). This *embedded Schrödinger equation* will give the ϕ in region I that is continuous with a solution in region II (of energy ε) such that the combined trial function has the lowest expectation value of energy. If the expectation value of the energy is further minimised with respect to ε, then the combined trial function will be the eigenfunction of the complete system of eigenenergy $E = \varepsilon$. In practice this requires the eigenenergy of the solution to be known before the equation can be directly solved, or iterative methods applied.

Within a continuum the equation takes a simpler form as the energy of the state required can be chosen from the outset, and the first order correction is zero ($\varepsilon = E$). In this case the embedded Hamiltonian corresponding to equation (2.14) and for a state of energy E can be written

$$H_{emb}(E) = H_I + \delta(\mathbf{r}_s - \mathbf{r}) \left[\frac{\partial}{\partial n_s} - \Gamma(\mathbf{r}_s, \mathbf{r}'_s; E) \right] \tag{2.15}$$

where $H_{emb}(E)$ is the embedded Hamiltonian that yields the states with correct boundary conditions, H_I is the normal Hamiltonian for region I (the sum of kinetic and potential energy operators) and $\Gamma(\mathbf{r}_s, \mathbf{r}'_s; E) = -G_0^{-1}(\mathbf{r}_s, \mathbf{r}'_s; E)$ is the embedding potential. The symbol $\Gamma(\mathbf{r}_s, \mathbf{r}'_s; E)$ is introduced here as alternative forms for the embedding potential are introduced in the next section. $\Gamma(\mathbf{r}_s, \mathbf{r}'_s; E)$ acting on a function denotes the integration over the surface $\mathcal{S}$ in equation (2.14).

2.1.2 Alternative Forms of the Embedding Potential

In this section more general expressions for the embedding potential are presented. These allow the embedding potential to be obtained from Green functions satisfying arbitrary boundary condition at the surface $\mathcal{S}$. To simplify the notation, the surface integrals present in the defining equations are presented as matrix multiplications. This implies a matrix representation of the spatial dependence of the functions in terms of a set of basis functions that are orthogonal over the surface of the embedding region - the surface integral itself corresponds to the basis being delta functions on the surface. It is straightforward to show that for this representation the matrix product corresponds to the integration over the surface $\mathcal{S}$, and inversion over the surface corresponds to matrix inversion.

In this notation equation (2.7) takes the form

$$\psi = -\mathcal{G}.\frac{\partial \psi}{\partial n_s} + \frac{\partial \mathcal{G}}{\partial n_2}.\psi \tag{2.16}$$

where $\mathcal{G}$ (ψ) is the matrix (vector) representation of the Green function (wavefunction of region II) on the surface $\mathcal{S}$. The normal derivative of the Green function is taken with respect to the second spatial variable, as denoted by the subscript, and in this expression $\mathcal{G}$ is a Green function that satisfies any boundary condition on the surface $\mathcal{S}$.

The embedding potential as required for the embedded Schödinger equation (2.15) is the operator that gives the normal derivative of a wavefunction on $\mathcal{S}$ in terms of its value on $\mathcal{S}$, or

$$\frac{\partial \psi}{\partial n_s} = \Gamma.\psi \tag{2.17}$$

where Γ is the matrix representation of the embedding potential operator[1]. In the previous section this was obtained from equation (2.7) (equation (2.16) in matrix notation) and a Green function with zero normal derivative on $\mathcal{S}$, but more general expressions can be derived with less stringent requirements on the boundary condition of the Green function. This is desirable since it widens the applicability of the method.

Two general expressions for the embedding potential can be obtained, each resulting in the *same* embedding potential as that given in the previous section.

Rearranging equation (2.16) gives

$$\frac{\partial \psi}{\partial n_s} = -\mathcal{G}^{-1}.\left(\mathcal{I} - \frac{\partial \mathcal{G}}{\partial n_2}\right)\psi \tag{2.18}$$

leading to

$$\Gamma = -\mathcal{G}^{-1}.\left(I - \frac{\partial \mathcal{G}}{\partial n_2}\right). \tag{2.19}$$

This general expression for Γ is the same as that originally derived by Green function matching techniques (Inglesfield, 1981; Garcia-Moliner and Rubio, 1969;

[1]Equation (2.17) defines the embedding potential, provided it is remembered that it must be valid for ψ of *any* energy. This expression can be used in place of equation (2.11) in the previous section, and gives the same embedded Schrödinger equation but with $-\mathcal{G}_0$ replaced with Γ.

Inglesfield, 1971) and for von Neumann boundary conditions reduces to

$$\Gamma = -\mathcal{G}^{-1} \text{ for } \frac{\partial \mathcal{G}}{\partial n_2} = 0 \tag{2.20}$$

immediately.

A second expression may be obtained by taking the normal derivative of equation (2.16) with respect to the 1^{st} spatial variable to give

$$\frac{\partial \psi}{\partial n_s} = -\frac{\partial \mathcal{G}}{\partial n_1} \cdot \frac{\partial \psi}{\partial n_s} + \frac{\partial^2 \mathcal{G}}{\partial n_1 \partial n_2} . \psi. \tag{2.21}$$

Rearranging this as before gives a second expression for the embedding potential in terms of a Green function satisfying general boundary conditions on the surface $\mathcal{S}$,

$$\Gamma = \left(I + \frac{\partial \mathcal{G}}{\partial n_1} \right)^{-1} \cdot \frac{\partial^2 \mathcal{G}}{\partial n_1 \partial n_2}, \tag{2.22}$$

an alternative and equally valid expression to equation (2.19) for the embedding potential in terms of a Green function satisfying arbitrary boundary conditions on $\mathcal{S}$.

As a special case this reduces to the form given by Fisher (Fisher, 1990),

$$\Gamma = \frac{\partial^2 \mathcal{G}}{\partial n_1 \partial n_2} \text{ for } \frac{\partial \mathcal{G}}{\partial n_1} = 0. \tag{2.23}$$

Fisher derives this form for the Green function satisfying the Dirichlet boundary condition

$$\mathcal{G} = 0 \text{ for } \mathbf{r} \text{ or } \mathbf{r}' \in \mathcal{S} \tag{2.24}$$

which implies the boundary condition in (2.23) since both $\mathbf{r}$ and $\mathbf{r}'$ are on $\mathcal{S}$.

Equations (2.19) and (2.22) give two distinct formulations of the embedding potential in terms of a Green function satisfying general boundary conditions on the surface $\mathcal{S}$.

This is exactly what is required to obtain Γ from the Green function calculated in chapters 3 and 4, whose value on $\mathcal{S}$ is not constrained. The choice of expression to use is discussed in chapter 4.

Is the Green function necessary for the construction of an embedding potential?

The embedding method requires the embedding potential, an operator that acts on the wavefunction ψ in region II at the surface $\mathcal{S}$ to give the normal derivative of ψ (equation (2.17), the defining equation). So far two distinct expression have been presented for Γ in terms of the Green function defined in region II. Provided the Green function is available this causes no problem, however for numerical calculations the Green function can be difficult to evaluate as its construction requires knowledge of the full eigenstate spectrum of the substrate (this will become more apparent in chapter 3). In view of this an important question is whether Γ can be constructed without recourse to the Green function, using only a subset of the eigenstates of the substrate system.

At first this seems reasonable since the embedding potential is essentially a logarithmic derivative of the wavefunction at the surface, so there is a possibility of deriving it directly from the eigenstates. Unfortunately this is not enough information to uniquely define the embedding potential - any number of different operators would possess this property for a given eigenstate. Another problem is that the Γ must be defined for energies where eigenstates are not present for the variational arguments used in the derivation (section 2.1.1) to be valid.

Another possibility is the use of the imaginary part of the Green function, or the *Spectral function* which depends only on states at the energy the function is evaluated. This would be an advantage since this quantity is far easier to calculate than the Green function itself. This is given by (Economou, 1990)

$$f(\mathbf{r},\mathbf{r}';E) = \int_{E'} dE' \psi^*_{E'}(\mathbf{r}')\psi_{E'}(\mathbf{r})\delta(E-E') \tag{2.25}$$

where f is the spectral function and $\psi_{E'}(\mathbf{r})$ is an eigenfunction of energy E'. This quantity satisfies the Schrödinger equation

$$(-\nabla^2_r + V(\mathbf{r}) - \varepsilon) f(\mathbf{r},\mathbf{r}';\varepsilon) = 0 \quad \mathbf{r},\mathbf{r}' \in II. \tag{2.26}$$

Taking this and the Schrödinger equation for the wavefunction in region II (equation (2.1)) allows Green's theorem to be àpplied in the same way as in the previous section to produce an equation similar to (2.7). Expressing this in the matrix no-

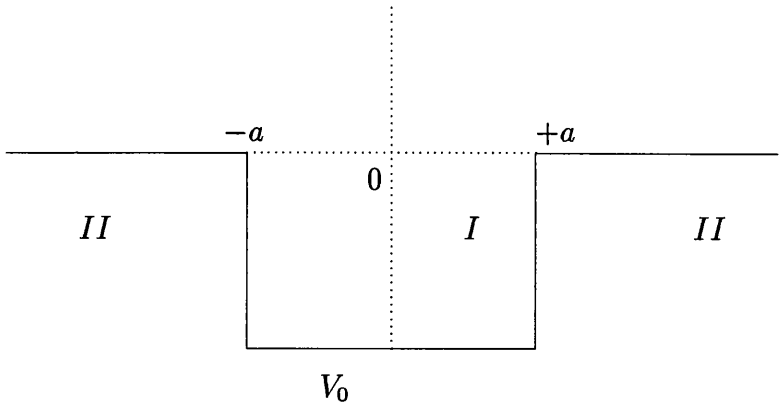

Figure 2.2: Square well embedded in a free electron potential.

tation used above, with $\mathcal{F}$ the matrix representation of f on the surface, gives

$$0 = -\mathcal{F}.\frac{\partial\psi}{\partial n_s} + \frac{\partial\mathcal{F}}{\partial n_1}.\psi \tag{2.27}$$

leading to

$$\Gamma = \mathcal{F}^{-1}.\frac{\partial\mathcal{F}}{\partial n_1}. \tag{2.28}$$

This expression is not strictly wrong, but it *only provides the correct embedding potential at the energies of discrete eigenstates on the real axis, and is completely inapplicable to embedding calculations.* In other words it is not valid between discrete eigenstates on the real axis, as is required, and is also not valid within a continuum of states *at all.* The root of the failure of these attempts to present a more numerically accessible expression for the embedding potential is that the method requires the defining equation to be true throughout the complex energy plane - that Γ is an analytic function. The reason for this is described in the following sections, where an example calculation is carried out for a system simple enough for analytic solution in order to illustrate the properties of the embedding method.

2.2 Embedding Calculation for a $1D$ Square Well

In this section the embedding method is applied to the square well shown in figure 2.2. A free electron is the chosen starting point, since this has the equivalent potential in region II and the potential in region I has no influence (this is the region that is replaced in the embedding calculation). The Green function for a

free electron in $1D$ with the boundary conditions at infinity of outward flowing waves (the retarded Green function) is

$$G(x,x';\varepsilon) = \frac{i}{2k}e^{ik|x-x'|} \tag{2.29}$$

where ε is the energy and $k = \sqrt{\varepsilon}$ (Economou, 1990). To obtain the embedding potential at the 'surface' $\mathcal{S}$ shown in figure 2.2 the outward gradient and values of the Green function at the two boundary points are required. It is then possible to represent the Green functions on the surface by using delta functions at $x = -a, a$ so that the magnitude and derivative take the matrix representations

$$\mathcal{G} = \frac{i}{2k}\begin{pmatrix} 1 & e^{2ika} \\ e^{2ika} & 1 \end{pmatrix} \tag{2.30}$$

and

$$\frac{\partial \mathcal{G}}{\partial n_2} = \frac{1}{2}\begin{pmatrix} 1 & -e^{2ika} \\ -e^{2ika} & 1 \end{pmatrix}. \tag{2.31}$$

In real space the quantity that takes the value of the Green function at the surface when integrated over the surface is given by

$$\delta(x-x_s)\delta(x'-x_s)G(x,x') = \begin{bmatrix} \delta(x-a) & \delta(x+a) \end{bmatrix} \mathcal{G} \begin{bmatrix} \delta(x'-a) \\ \delta(x'+a) \end{bmatrix} \tag{2.32}$$

and similarly for the normal derivative and embedding potential itself. This gives the required surface integral when an energy expectation value is calculated from the embedded Hamiltonian.

Placing these in equation (2.19), the first expression for the embedding potential in terms of a Green function with general boundary conditions (equation (2.22) would give the same result) gives

$$\delta(x-x_s)\Gamma(x,x';\varepsilon) = -ik\left[\delta(x+a)\delta(x'+a) + \delta(x-a)\delta(x'-a)\right] \tag{2.33}$$

as the required embedding potential. As before this should be understood as a surface integral operator.

To illustrate how the method works this embedding potential is used to solve for the states of a square well potential. There are two types of states - the bound states and the propagating states. In what follows these are dealt with distinctly.

2.2.1 Bound States

In this section the bound states are obtained directly from the variational method (as used to derive the embedded Schrödinger equation). In the region of negative energy the embedding potential (2.33) can be written as

$$\delta(x-x_s)\Gamma(x,x';\varepsilon) = -\lambda\left[\delta(x+a)\delta(x'+a)+\delta(x-a)\delta(x'-a)\right] \tag{2.34}$$

where $\lambda = \sqrt{-\varepsilon}$. Employing the trial function

$$\phi(x) = b_1 \cos kx + b_2 \sin kx \tag{2.35}$$

where k is (for now) a variational parameter, gives an expression for the expectation value of the energy of this function in the embedded Hamiltonian. Although this trial function will give the correct bound states for the appropriate b_1, b_2 and k this is not assumed to be the case in what follows.

Using equation (2.13) (or (2.14)) gives

$$E = \frac{(k^2+V_0)\langle\phi|\phi\rangle + \varepsilon\langle\phi|\delta(x-x_s)\frac{\partial\Gamma}{\partial\varepsilon}|\phi\rangle + \langle\phi|\delta(x-x_s)(\frac{\partial}{\partial n_s}-\Gamma)|\phi\rangle}{\langle\phi|\phi\rangle + \langle\phi|\delta(x-x_s)\frac{\partial\Gamma}{\partial\varepsilon}|\phi\rangle}. \tag{2.36}$$

The problem then reduces to a minimisation problem; the minimisation of E with respect to the variational parameters b_1, b_2, k and ε.

In what follows the variation of E is examined around the known solutions of this problem to examine exactly how the extra terms in the Hamiltonian introduce the minima. From basic quantum theory the eigenfunctions of this system are given by

$$\begin{aligned} \tan ka &= \tfrac{\lambda}{k} \quad b_2 = 0 \\ \tan ka &= -\tfrac{k}{\lambda} \quad b_1 = 0 \end{aligned} \tag{2.37}$$

the even and odd solutions respectively. Taking the first even solution and denoting its energy E_1 (and the first odd solution E_2) the effect of variations in the trial function parameters can be examined. For $V_0 = -5$ Ryd and $a = 1$ au two eigenstates are present, $E_1 = -3.852$ Ryd and $E_2 = -0.931$ Ryd.

Firstly the variation of E with the energy, ε, of the embedding potential is illustrated. Taking equation (2.36) with a trial function corresponding to the 1^{st} even eigenstate of the square well gives the energy E as a function of ε, the energy of

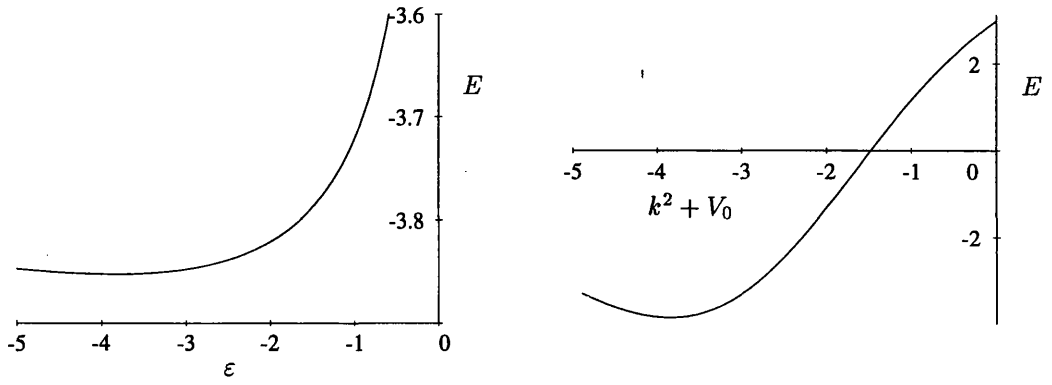

a) $E(\varepsilon)$, $k^2 + V_0 = E_1$ b) $E(k^2 + V_0)$, $\varepsilon = E_1$

Figure 2.3: Expectation value of the energy, E, for an *even* trial function.

the embedding potential (ie $k^2 + V_0 = E_1$, $b_2 = 0$ and $E = E(\varepsilon)$). This function is shown in figure 2.3a, for $V_0 = -5$ Ryd and $a = 1$ au, and possesses a minimum at $\varepsilon = E_1$ where E takes the value E_1, as expected.

Next the variation of E with the trial function itself is shown. Equation (2.6) is evaluated for an even trial function of arbitrary energy, with the embedding potential evaluated at the eigenenergy of the 1^{st} even state (ie $\varepsilon = E_1$ $b_2 = 0$ and $E = E(k)$). In figure 2.3b the variation of E with the parameter k of the trial function is examined, again for $V_0 = -5$ Ryd and $a = 1$ au. E is shown as a function of $k^2 + V_0$, and as in figure 2.3a a minimum is present at $k^2 + V_0 = E_1$, where $E = E_1$. In each of the above cases letting b_2 take non-zero values increases the E value at the minima.

Variations in E with the form of the trial function can be examined by evaluating the embedding potential and the trial wave function at the same energy. Setting $\varepsilon = k^2 + V_0$ in equation (2.36) results in the simpler expression

$$E = \varepsilon + \frac{\langle\phi|\delta(x - x_s)(\frac{\partial}{\partial n_s} - \Gamma)|\phi\rangle}{\langle\phi|\phi\rangle + \langle\phi|\delta(x - x_s)\frac{\partial\Gamma}{\partial\varepsilon}|\phi\rangle}. \tag{2.38}$$

Figure 2.4 shows the value of this expression as a function of ε for an even, odd and mixed trial function, for $V_0 = -5$ Ryd and $a = 1$ au. It should be noted that the algebraic expression depends on the coefficients only through the ratio of their moduli squared, or that the relative phase of b_1 and b_2 has no influence on E. Figure 2.4 clearly shows the minima at the 1^{st} (even) solution and the 2^{nd} (odd) solution at $\varepsilon = E_1$ and $\varepsilon = E_2$ respectively, and the energy expectation value at

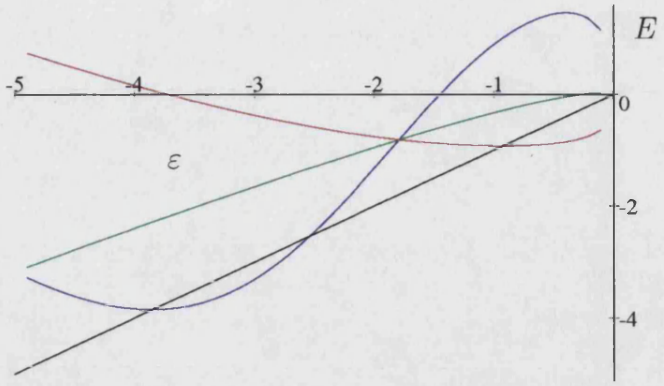

— $|b_1| = 0$, — $|b_2| = 0$, — $|b_1| = |b_2|$, — $E = \varepsilon$

Figure 2.4: Expectation value of the energy, E, as a function of $\varepsilon = k^2 + V_0$.

these minima is equal to ε. For the mixed trial function $|b_1| = |b_2|$ no minimum is present.

Looking at equation (2.38) it is apparent that at these minima the fractional term on the RHS is zero, and at these minima the trial function matches decaying solutions outside of the square well. However, this term can be zero for other values (between E_1 and E_2 for the even function - see figure 2.4 for $E = \varepsilon$) and the normalisation term in the denominator is important in ensuring that minima are present only at the eigenvalues.

So, to sum up, the embedding method provides a variational scheme to calculate the bound states of a system. The eigenstates are the solutions that provide a stationary $\langle\phi|H_{emb}|\phi\rangle$ with respect to variations in

- the trial function
- the energy that Γ is evaluated at.

This stationary solution is a correct bound state of the system that consists of region II outside of the boundary region (and region I inside) - the combined embedded and substrate system.

2.2.2 Propagating States and Resonance States

The embedding method can also be applied to obtain the continuum spectrum of the square well system, the states with eigenenergies greater than zero. If the obvious extension of the bound state method is applied a number of problems are encountered.

- The Hamiltonian is complex - the expectation value of the energy is complex for $k^2 + V_0$ and ε real (the embedding potential is complex).

- There is no minimum present with respect to the variational parameters *for real energies.*

In the original derivation of the embedding method Inglesfield (1981) approaches continuum states in terms of the Green function for the system. The validity of the embedding potential method for continuum states is proved by showing that the Green function for the complete system and the Green function for the embedded Hamiltonian have the same poles and residues at these poles, hence they are the same Green function.

The eigenstates that the complete and embedded system share are *resonance* states that correspond to the same boundary conditions satisfied by the bound states - that is on the left of the square well the wavefunction takes the form of a wave propagating to the left, and on the right hand side of a wave propagating to the right (in what follows the states are found to decay and propagate) [2].

These states possess *complex* eigenvalues and are the eigenstates of the embedded Hamiltonian (which is non-Hermitian), and also corresponding to the minima of the expectation value of the energy of a trial function in I.

The fact that the discrete eigenstates of the system with complex eigenvalues (the complex eigenenergy resonance states) are the same for both systems is the reason that the Green functions are equivalent. Since this is the case the properties of the propagating states are implicitly included in the embedded system (they can be obtained from the Green function for instance) even though these states are *not*

[2]The two types of states that are discussed here are the resonance/bound states that propagate and/or decay as $x \to \infty$ for $x > 0$ and $x \to -\infty$ for $x < 0$, and the propagating states that propagate and/or decay in one direction only (as $x \to \infty$ or $x \to -\infty$). For instance the bound states of a square well are of the first type, and the plane waves of free space are of the second type.

eigenvalues of the embedded Hamiltonian.

Another way to view this problem is that for the complete extended system, the states in $1D$ exist as pairs of degenerate eigenstates at each energy in the continuum. To reproduce these states the embedding scheme would somehow have to provide a minimum in the expectation energy of a trial function that was a general linear superposition of these propagating solutions. In order to illustrate these points and to illustrate the resolution of this apparent inconsistency the Green function of the square well is derived via the embedding method.

The Green function in region I is defined by the equation

$$\left[H + \delta(x - x_s)\left(\frac{\partial}{\partial n_s} - \Gamma\right) - E\right] G(x, x'; E) = \delta(x - x') \tag{2.39}$$

for x and x' in I. Note that the embedding operators (the derivative and the potential itself) give a non-zero result only at the boundary between regions I and II. Within region I this equation is simply the familiar inhomogeneous Schrödinger equation. Since the potential in region I is flat the Green function takes the form of a linear superposition of a free electron Green function and an appropriate solution of the corresponding homogenous equation (these are the complimentary function and particular integral)

$$G(x, x'; E) = \frac{i}{2\alpha} e^{i\alpha|x-x'|} + h(x, x'; E) \tag{2.40}$$

where $\alpha^2 + V_0 = E$ and h takes the general form

$$h(x, x'; E) = a_1(x'; \alpha) e^{i\alpha x} + a_2(x'; \alpha) e^{-i\alpha x}. \tag{2.41}$$

With this expression, finding the Green function reduces to the problem of finding the functions $a_1(x'; \alpha)$ and $a_2(x'; \alpha)$. Substituting equation (2.40) in (2.39) yields the expression

$$\delta(x - x_s)\left(\frac{\partial}{\partial n_s} - \Gamma(E)\right)\left(\frac{i}{2\alpha} e^{i\alpha|x-x'|} + h(x, x'; E)\right) = 0 \tag{2.42}$$

where the LHS may be non-zero only at the border between regions I and II (due to the δ function). Equation (2.33) gives the explicit form for the embedding potential, and placing this in (2.42) with (2.41) leads to the requirement that a_1

and a_2 satisfy

$$\begin{pmatrix} (k+\alpha)e^{i\alpha a} & (k-\alpha)e^{-i\alpha a} \\ (k-\alpha)e^{-i\alpha a} & (k+\alpha)e^{i\alpha a} \end{pmatrix} \begin{pmatrix} a_1(x';\alpha) \\ a_2(x';\alpha) \end{pmatrix} = \frac{k+\alpha}{2i\alpha} \begin{pmatrix} e^{i\alpha(a-x')} \\ e^{i\alpha(a+x')} \end{pmatrix}. \quad (2.43)$$

Solving (2.43) for a_1 and a_2 leads to the Green function for the $1D$ square well with x and x' in I

$$G(x,x';E) = \frac{1}{\Delta} y_1(x_>) y_2(x_<) \quad (2.44)$$

where

$$\begin{aligned} y_1(x) &= (\alpha-k)e^{i\alpha(a-x)} + (\alpha+k)e^{-i\alpha(a-x)} \\ y_2(x) &= y_1(-x). \end{aligned} \quad (2.45)$$

$\Delta = y_1 y_2' - y_1' y_2$ is the Wronskian of y_1 and y_2, and $x_>$ and $x_<$ are the larger and smaller of x and x' respectively. This is a standard form for a one dimensional Green function (Morse & Feshbach, 1953). The function $y_1(x)$ takes the form of a wave propagating outwards for $x > a$, and continuous in amplitude and derivative across the step at $x = a$. Similarly, $y_2(x)$ is a wave propagating to the left for $x < -a$, and continuous in amplitude and derivative across the step at $x = -a$.

When the Wronskian is zero y_1 and y_2 are not linearly independent, and an eigenstate occurs. This Wronskian is given explicitly by

$$\Delta = 8i\alpha^2 k \cos^2 \alpha a \left(\tan \alpha a + \frac{ik}{\alpha}\right)\left(\tan \alpha a + \frac{i\alpha}{k}\right) \quad (2.46)$$

and the zeroes of Δ are shown in figure 2.5. In this figure the blue lines correspond to a zero real Δ and the red lines to a zero imaginary Δ. Zeroes of the Wronskian are present where these lines cross (marked by circles), and these are the energies where eigenstates exist. For $E < 0$ the eigenstates are the bound states, and for $E > 0$ the eigenstates are the *resonance* states.

Examining the residue of the Green function at each of these poles reveals that the resonance states take the same analytic form as the bound states (cos and sin functions), and are the states that would arise from solving the square well problem by matching the solutions within I with plane waves in II propagating outward from I. This means they are also eigenstates of the embedded+substrate system, and it is the equivalence of these sets of eigenstates that leads to the equivalence of the Green functions for the two systems.

These complex eigenvalues occur due to the analytic continuation of the Schrödinger

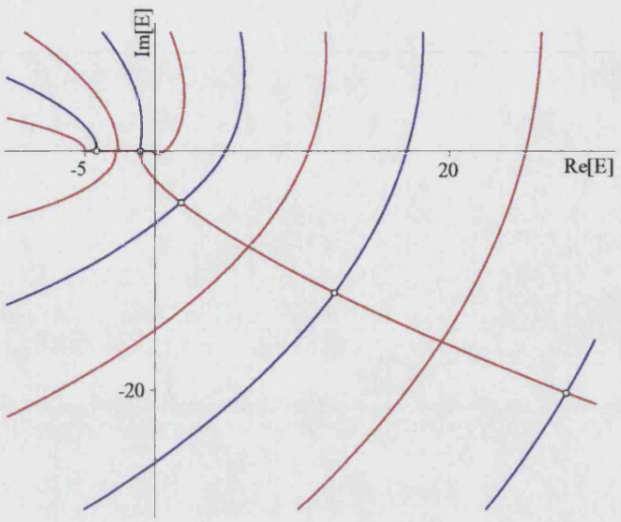

— $Re[\Delta] = 0$, — $Im[\Delta] = 0$ and ∘ denote $\Delta = 0$

Figure 2.5: Zeroes of the Wronskian.

equation (or the Green functions) onto the non-physical sheet of the complex energy plane. This corresponds to the analytic continuation of the Green function at energies in the upper half complex plane to the lower half plane with no branch cut. These solutions appear in scattering theory methods (Taylor, 1972; Yaris, 1978), dilatation transformation methods (Simon, 1972) and others (Andriotis, 1992).

Since the Green functions (for the embedded and complete system) are equivalent in the upper half complex energy plane, then on the real axis the embedded Green function should be expected to represent a set of extended propagating states implicitly, even if they are not eigenstates of the embedded Hamiltonian.

To show this we examine the imaginary part of the Green function on the real axis, and through simple but tedious algebra, the form

$$Im\left[G(x,x';E)\right] = \frac{k}{2}\left(\frac{\cos\alpha x\cos\alpha x'}{\alpha^2\cos^2 ka + k^2\sin^2 ka} + \frac{\sin\alpha x\sin\alpha x'}{k^2\cos^2 ka + \alpha^2\sin^2 ka}\right) \tag{2.47}$$

is obtained (E is now real).

This imaginary part is given by the expression (Economou, 1990)

$$Im\left[G(x,x';E)\right] = \pi\sum_i \phi_i(x)\phi_i^*(x')\delta(E-E_i) \tag{2.48}$$

where $\phi_i(x)$ is an eigenfunction of energy E_i. Applying (2.48) to the degenerate pairs of functions

$$\phi_E^{(1)} = \left(\frac{\alpha k}{2\pi}\right)^{\frac{1}{2}} \frac{\cos \alpha x}{\alpha \cos ka + ik \sin ka},$$

$$\phi_E^{(2)} = \left(\frac{\alpha k}{2\pi}\right)^{\frac{1}{2}} \frac{\sin \alpha x}{k \cos ka + i\alpha \sin ka} \tag{2.49}$$

gives equation (2.47) (where as before $E = \alpha^2 + V_0 = k^2$). As expected the influence of the substrate system is felt only in the *normalisation* of these states. It is this that provides the structure of the Green function and density of states within the square well, and propagating solutions can be constructed from an appropriate linear superposition of these two solutions.

The density of states within the embedding region (region I) obtained from the relation (Economou, 1990)

$$n(E) = \frac{1}{\pi} \int_{-a}^{a} dx Im\left[G(x, x; E)\right] \tag{2.50}$$

is shown in figure 2.6 for increasing well depth. This clearly shows the contribution to the DOS from the poles in the complex energy plane, with a pole becoming closer to the real axis for increasing well depth. For $V_0 = -10$ Ryd the lowest energy resonance is almost bound, and for $V_0 = -12$ Ryd this resonance has become a bound state.

2.2.3 Embedding in a Kronig-Penney Potential

In this thesis the embedding method is applied to a periodic potential, and in view of this it seems appropriate to briefly examine the case of a periodic lattice of square wells (Kronig-Penney) to see if anything is fundamentally different from the single square well investigated above.

The potential chosen for the substrate system is a lattice of square wells $2a$ wide and separated by $2a$, a lattice constant of $4a$. The first step is to construct the Green function for the substrate system.

For a periodic potential this will take the general form (Noguera, 1990)

$$G(x, x'; E) = \frac{1}{\Delta} \Psi_k(x_>) \Psi_{-k}(x_<) \tag{2.51}$$

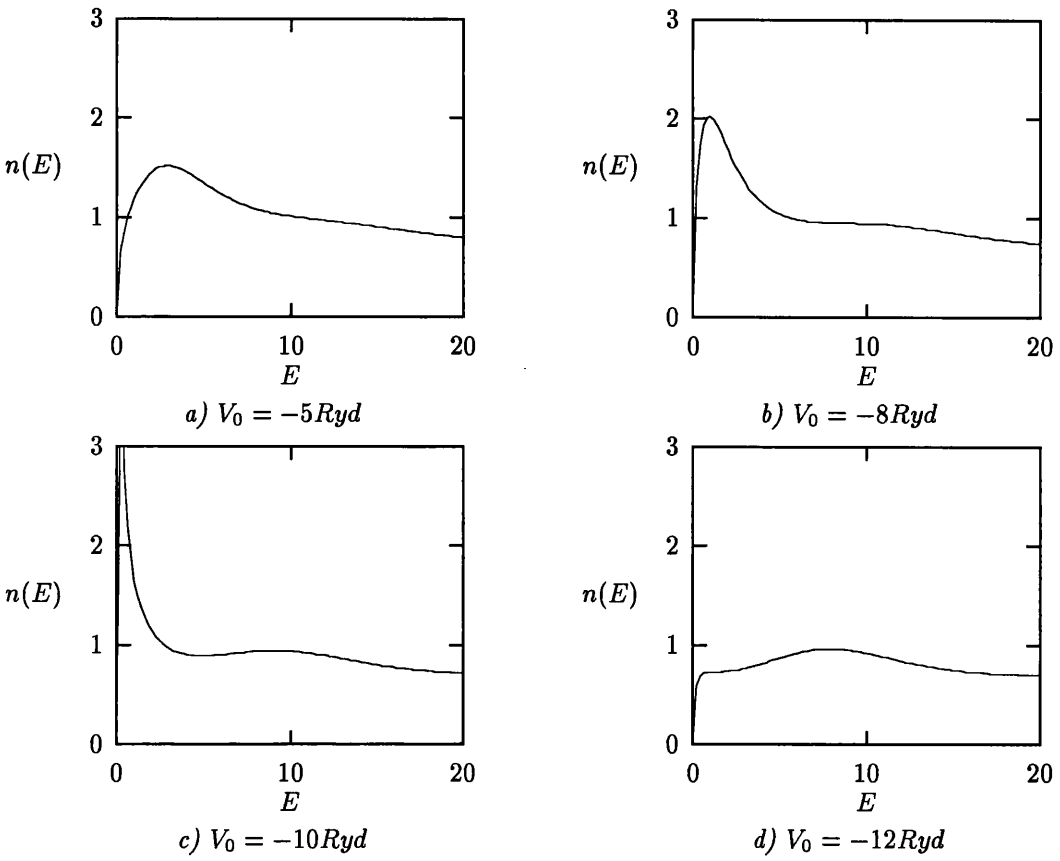

Figure 2.6: DOS within square well for deepening well.

where Ψ_k and Ψ_{-k} are Bloch functions of the same energy $E = E_k$, and $\Delta = \Psi_k\Psi'_{-k} - \Psi'_k\Psi_{-k}$ is the Wronskian. For energies within a band gap Ψ_k decays with increasing x, and the Ψ_{-k} decays for decreasing x. In order to evaluate the Green function in the complex plane the Bloch functions must be available in a form that can be analytically continued into the complex plane.

Using this Green function the embedding potential for a 'surface' at the edges of a square well can be constructed as with the square well potential. The surface $\mathcal{S}$ is at $x = a, -a$ as before, and encompasses a square well within the lattice. The embedding potential is then given by (in analogy to equation (2.33))

$$\delta(x-x_s)\Gamma(x,x';\varepsilon) = -\frac{\Psi'_k(a)}{\Psi_k(a)}\delta(x-a)\delta(x'-a) - \frac{\Psi'_{-k}(-a)}{\Psi_{-k}(-a)}\delta(x+a)\delta(x'+a) \quad (2.52)$$

which reduces to (2.33) for the free electron case (Ψ_k a positive propagating plane wave).

From the discussion in the previous section it is apparent that the eigenstates of an embedded Hamiltonian with this embedding potential will not possess real

eigenvalues. The eigenstate in region I will match the function $\Psi_k(x)$ at $x = a$ and $\Psi_{-k}(x)$ at $x = -a$, so the only eigenstates on the real axis will be states with energies in the band gaps and any other states will be resonance states as in the square well case.

2.3 Conclusion

In this chapter the embedding method of Inglesfield (1981) has been briefly presented as it is central to the work carried out in the rest of this thesis. In order to apply this method to a particular problem an embedding potential must be derived that describes the system outside of the embedding region (region I in figure (2.1)). Two different expressions (one new) for the embedding potential expressed in terms of the substrate system Green function were derived, both giving the same embedding potential.

The rest of the chapter was concerned with finding the states of a square well using the embedding method (and a brief discussion of the Kronig-Penny lattice) to illustrate the properties of the embedding method. The most important single property of the embedded Hamiltonian that the method revolves around is that although it reproduces the discrete states exactly, it possesses no continuum eigenstates. Where a continuum is expected, the embedded Hamiltonian (which is non-Hermitian) possesses only eigenstates of complex energy, corresponding to an analytic continuation of the bound states. These *resonance* states are also eigenstates of the complete system, and it is due to this that the embedded Green function and the complete system Green function are identical (in the upper half complex plane at least).

A brief discussion of the $1D$ Kronig-Penney lattice is also presented since periodic potentials provide the substrate system for the rest of this thesis, and a reasonable argument is given that the same resonance states will be present for the periodic potential.

In the next three chapters the problem to be solved takes the form of an embedding calculation, entirely analogous to the example carried out in this chapter. First the pseudo-states are obtained for a lattice of atoms described by a pseudopotential (see figure 2.7a), then an embedding surface is selected that encompasses the core region of an atom. An embedding potential is obtained on this surface, and then an

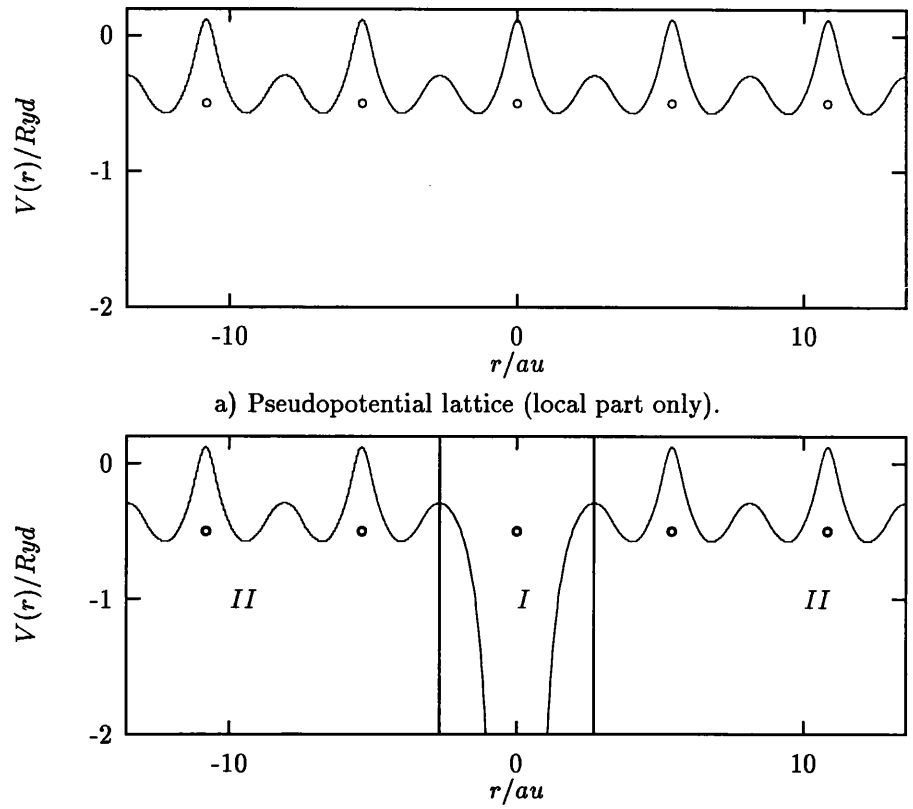

a) Pseudopotential lattice (local part only).

b) Pseudopotential lattice with embedded all-electron atom.

Figure 2.7: Self consistent potential for substrate and embedded all-electron atom.

embedded Hamiltonian is constructed within this surface, including core-electrons that are not included in the original pseudopotential system. This Hamiltonian is then solved within the embedding region (region *I* in figure 2.7b) to give the all-electron states in this region. Another way to view the final solution is a solution in the potential given in figure 2.7b - a lattice of pseudo-atoms with one all-electron atom at its centre. The valence electrons at this atom take the correct structure since they satisfy correct boundary conditions at the surface (pseudo and all-electron states are equal here), and the core electrons are bound by the depth of the potential in the all-electron atom (for an all-electron lattice, the core electrons would be very nearly bound and localised to each atom - this is one of the reasons for the success of the pseudopotential approximation in the first place).

Chapter 3

Green functions from Plane-wave Pseudopotential Calculations

3.1 Introduction

This chapter begins with a brief overview of density functional theory and the local density approximation, the basic framework of theory of all the calculations performed in this thesis from this point on. Following this is a brief description of the pseudopotential approximation and total energy pseudopotential calculations with a plane wave basis. It is these calculations that provided the pseudo-states of the substrate system used to construct the Green function, and so the embedding potential.

The rest of the chapter is devoted to the Green function of the substrate system - the method for reconstructing the core states from the pseudopotential calculation given in this thesis relies heavily on the properties of the single particle time independent Green function (Economou, 1990). This Green function characterises both the spectral properties of the system (the Hamiltonian) and the boundary conditions of the system. In view of this, it is vital to obtain an accurate approximation to the Green function of the pseudopotential system. This approximation must possess the correct analytic form and the physical quantities obtained from it must be realistic (for example the states should form a continuum where they are expected to).

In sections 3.4 and 3.5, approximation methods using the spectral representation to

obtain the pseudo-Green function from the pseudo-states are investigated. These sections describe how the spectral representation can be evaluated most efficiently for a finite number of **k** points in the Brillouin Zone. The method chosen gives an approximation to the Green function with a continuum of states within bands.

From the previous chapter it is apparent that an embedding surface must be defined. It is within this surface that the reconstruction will be carried out, and on this surface that the embedding potential is defined (and pseudo-Green function required). This surface is chosen as a sphere centred on an atomic site with a radius greater than the radius at which the pseudo and real states agree (ie $> r_c$, the core radius of the pseudopotential). To perform the surface inversion discussed in the previous chapter, basis functions are required that are orthogonal over the surface of this sphere, and the spherical harmonics are employed here. For this basis the Green function on the surface is represented as a matrix of expansion coefficients. If a different embedding surface was required the same method could be applied provided a set of basis functions could be found that are orthogonal over the surface (only the symmetrisation of the Brillouin zone integral would need much attention - section 3.4)

Using the plane wave basis set for the initial total-energy calculation is also not a requirement of the application of this method. Exactly the same scheme could be applied provided the eigenstates could be expanded in spherical harmonics.

3.2 Density Functional Theory and the Pseudopotential Method

To solve the system of an infinite number of electrons interacting with an infinite number of atomic nuclei is a formidable many body problem. In order to make this system soluble a number of well established techniques are available. The many body nature of the problem is dealt with using *Density Functional Theory*, which effectively 'decouples' the electrons and reduces the system to an equivalent independent particle problem.

The basis of the Density Functional (DF) (Parr and Yang, 1989) approach is the central theorem that the ground state energy of an interacting system of electrons in a given potential can be expressed as a unique functional of the charge density

due to these electrons, and that this energy is at a minimum when the charge density is that of the ground state of the electrons in the potential.

This total energy functional can be written as

$$E_{tot}[\rho(\mathbf{r})] = T_s[\rho(\mathbf{r})] + V_H[\rho(\mathbf{r})] + V_{ext}[\rho(\mathbf{r})] + E_{XC}[\rho(\mathbf{r})] \tag{3.1}$$

where the first term on the RHS is the contribution from the kinetic energy, the second term the contribution from the Coulomb interaction between the electrons, the third term the contribution from the external potential (due to the nuclei for a lattice of atoms) and the fourth from the exchange-correlation interaction of the electrons. The first three terms of this expression have natural classical analogues, but the exchange-correlation energy is purely quantum in nature.

To find the minimum of this total energy functional, E_{tot}, with respect to variations in ρ, requires knowledge of the functional itself. Unfortunately no simple analytic form exists for this functional (specifically the kinetic energy and exchange-correlation parts) so this can not be directly achieved. However, the problem can be solved in terms of the states of non-interacting electrons in an effective potential due to all the other electrons as was shown by Hohenberg, Kohn and Sham (Hohenberg and Kohn, 1964; Kohn and Sham, 1965). The Schrödinger equation for these states is

$$\left[-\frac{\hbar^2}{2m}\nabla^2 + V_{ext}(\mathbf{r}) + V_H(\mathbf{r}) + V_{XC}(\mathbf{r})\right]\psi_i(\mathbf{r}) = \varepsilon_i\psi_i(\mathbf{r}) \tag{3.2}$$

where V_{ext} is the external potential (here due to the nuclei), V_H is the Coulomb potential due to the charge density of the electron gas given by

$$V_H(\mathbf{r}) = e^2 \int d^3\mathbf{r}' \frac{\rho(\mathbf{r}')}{|\mathbf{r} - \mathbf{r}'|}, \tag{3.3}$$

and V_{XC} is the potential due to exchange-correlation interactions, given as the functional derivative

$$V_{XC} = \frac{\delta E_{XC}[\rho(\mathbf{r})]}{\delta\rho(\mathbf{r})}. \tag{3.4}$$

The charge density due to these states is

$$\rho(\mathbf{r}) = 2\sum_i |\psi_i(\mathbf{r})|^2 \tag{3.5}$$

where the sum is over the occupied states. These are referred to as the *Kohn-*

Sham equations. The minimum of the total energy functional (and so the correct ground state) can be shown to occur when this equation is consistent, when the ψ_i resulting from the solution of the Kohn-Sham equation for a given potential results in the same potential. It should be stressed that this is an exact result, involving no approximations to the many body nature of the problem.

3.2.1 The Local Density Approximation

Using this formulation the ground state charge density (and total energy) can be calculated by iteration, provided the exchange-correlation potential can be evaluated. The exchange-correlation functional is not known, and some approximation must be made to perform actual calculations. In this work the approximation employed is the *Local Density Approximation* (LDA) (Kohn and Sham, 1965). If E_{XC} is expressed as

$$E_{XC}[\rho(\mathbf{r})] = \int \epsilon_{XC}[\rho(\mathbf{r})]\rho(\mathbf{r})d^3\mathbf{r} \tag{3.6}$$

where $\epsilon_{XC}[\rho(\mathbf{r})]$ is the exchange-correlation energy contribution from the charge at $\mathbf{r}$, then it is reasonable to assume that this contribution depends only on the form of the charge distribution in the vicinity of $\mathbf{r}$.

This suggests approximating this quantity by the exchange-correlation energy per electron for a homogeneous electron gas with the equivalent charge density at $\mathbf{r}$, denoted $\epsilon_{XC}^{hom}(\rho)$ This is the local density approximation (LDA). The exchange-correlation potential is then approximately given by

$$V_{XC}(\mathbf{r}) = \frac{\partial}{\partial\rho(\mathbf{r})}\left[\epsilon_{XC}^{hom}(\rho(\mathbf{r}))\rho(\mathbf{r})\right] \tag{3.7}$$

which can be expected to be a good approximation for smooth charge densities and involves no functional derivatives. The exchange-correlation energy for the homogeneous electron gas can be found accurately using Quantum Monte Carlo methods. Using these results accurate parameterisation can be constructed, and many parameterisations are available in the literature (Wigner, 1938; Kohn and Sham, 1965; Hedin and Lundquvist, 1971; Vosko et al, 1980; Perdew and Zunger, 1981; Ceperly and Alder, 1980).

Since the introduction of this approximation it has been found to provide an extremely successful approximation to the exchange-correlation potential for a wide range of systems even if the charge density is not particularly uniform, and it is

the standard approximation used within DFT (see Jones and Gunnarsson, 1989 for a discussion). All of the calculations carried out within this thesis are performed using the LDA. In the rest of this thesis where the terms electron states, the Schrödinger equation or the self-consistent potential are used they refer to the Kohn-Sham states, equation and self-consistent potential respectively.

3.2.2 Plane Wave Basis Set

As described above DFT and the LDA provide a description of an interacting electron gas in a given external potential, accurately taking into account the electron-electron interactions. For a periodic lattice a reasonable choice of basis set is the plane wave basis set since this has useful analytic properties. Since the solutions in the periodic potential are Bloch waves this gives the form (Payne et al, 1992)

$$\Psi^n_{\mathbf{k}}(\mathbf{r}) = \sum_{\mathbf{g}} C^n_{\mathbf{g}}(\mathbf{k}) e^{i(\mathbf{k}+\mathbf{g}).\mathbf{r}} \tag{3.8}$$

for the Bloch states. Substituting this into equation (3.2) and taking account of the potentials being periodic gives the equation

$$\sum_{\mathbf{g}'} \left[\frac{\hbar^2}{2m} |\mathbf{k}+\mathbf{g}|^2 \delta_{\mathbf{g}\mathbf{g}'} + V_{ext}(\mathbf{g}-\mathbf{g}') + V_H(\mathbf{g}-\mathbf{g}') + V_{XC}(\mathbf{g}-\mathbf{g}') \right] C^n_{\mathbf{g}'}(\mathbf{k})$$

$$= \varepsilon^n(\mathbf{k}) C^n_{\mathbf{g}}(\mathbf{k}) \tag{3.9}$$

where the kinetic energy part is diagonal and the potentials appearing in this expression are the Fourier transforms of the potentials in equation (3.2). The V_{ext} is the potential due to the periodic lattice of nuclei.

3.2.3 Pseudopotential Methods

Solving equation 3.9 for the eigenfunctions and eigenvalues at each $\mathbf{k}$ in the 1^{st} Brillouin zone results in the band structure of the electrons in a periodic lattice of atomic nuclei (in fact the eigenstates of the equivalent Kohn-Sham system within the LDA). Enough reciprocal lattice vectors must be included for the solutions (or the total energy) to have converged. For an all-electron calculation, with V_{ext} the sum of the potentials of the nuclei, this requires an exorbitantly large number of plane waves (Payne et al, 1992). This is a consequence of the rapid oscillations in

the wave functions near the nucleus caused by the depth of the potential in this region responsible for binding the core states. This makes the plane wave basis set completely unsuitable for electronic structure calculations involving nuclear potentials.

A solution to this problem is provided by the *pseudopotential* approximation (Bachelet et al, 1982) which allows convergence to be achieved with a considerably smaller number of plane waves. First the electrons present in the system are divided into two classes - the higher energy valence electrons which propagate freely throughout the lattice and the localised core electrons which are localised around each atomic site. Physical properties of the lattice are dominated by the valence electrons since these are the electrons that take part in the interaction between atoms in the lattice, whereas the core electrons show very little interaction between atoms.

The pseudopotential approximation replaces the all-electron system in the potential of a lattice of atomic nuclei with a related system of only the valence electrons in a potential consisting of a lattice of pseudopotentials centred at each atomic site. This pseudopotential should satisfy the conditions that:

- The eigenvalues in the pseudopotential system are the same as the eigenvalues of the valence electrons in the all-electron system.
- The eigenfunctions in the pseudopotential system are the same as the eigenfunctions of the all-electron system in the region between the atomic sites (where core states are not significant) and smoothly varying (node-less) near the atomic sites.

Another way to view this is that the pseudopotential reproduces the valence electron scattering properties of the nucleus+core electrons system outside a certain radius (denoted r_c). Provided a pseudopotential can be found that satisfies these criteria far fewer plane waves will be required to solve a secular equation for the lattice, since the node-less pseudo-wave functions are smooth near the atomic sites, and the core states are not present.

At first it appears that this prescription requires knowledge of the states in the core regions of the lattice to calculate the pseudopotential, however this is not the case. The usefulness of the pseudopotential is a consequence of the important property of *transferability*, described below.

If the radial Schrödinger equation for a given potential is solved at an energy ε_l to give a solution $\phi_l(r)$, then this solution satisfies the identity (Bachelet et al, 1982)

$$-\left[(r\phi_l)^2 \frac{d}{d\varepsilon_l}\frac{d}{dr}\ln\phi_l\right]_R = \int_0^R \phi_l^2 r^2 dr, \tag{3.10}$$

or that the radial logarithmic derivative of $\phi_l(r)$ at radius R depends to first order on the charge within R associated with $\phi_l(r)$ (this is a special case of equation (2.12)).

Consider two different potentials that yield solutions at energy ε_l that match outside of a given radius and possess the same charge within this radius. Equation (3.10) states that the variation with energy of the scattering properties (the radial logarithmic derivative is directly related to the scattering phase shift - (Schiff, 1955)) of the two potentials are equal to first order in energy. Provided this agreement to first order is sufficient then a potential that reproduces the valence states for a *free* atom will accurately reproduce the states for an atom involved in bonding. This requirement that the charge associated with ϕ_l within r_c is conserved is referred to as *norm conservation.* A brief description of the prescription to find a norm conserving pseudopotential is given below. The specific method used for the calculations carried out in this thesis is that introduced by Kerker (1980).

Firstly a self-consistent all-electron atomic calculation for the atom of interest is performed within the framework of the LDA as described above, resulting in a self consistent potential for the free atom. The eigenstates of this potential are then divided into core and valence states, and the valence states alone are used to construct the pseudopotential. Close to the core (within the radius r_c) the valence eigenfunctions are replaced with a smooth, nodeless function that conserves the charge associated with each eigenfunction within r_c. The Schrödinger equation is then inverted for each of these pseudo atomic valence state to give the potential that would result in these pseudo states at the appropriate eigenenergies (this potential is different for each state within r_c). This l dependent potential is then 'unscreened' to remove the Coulomb and exchange-correlation interactions associated with the pseudo states. This yields an l dependent 'ionic' potential, $V_l^{pseud}(r)$, which when used in place of the nuclear potential for an atomic calculation yields the same valence eigenvalues, and valence eigenstates identical to the all-electron eigenstates outside of the core region but with a different, node-less structure inside the core radius. In addition to this, because the solutions are norm conserving the potential is transferable - the scattering properties of the potential are reproduced to first

order at energies differing from the eigenenergies of the free atom.

It should be noted that the 'unscreening' is effectively a linearisation of the exchange-correlation potential, and although exact for the free atom for a different system the exchange-correlation potential is taken as a sum of the potential due to the core electrons alone (included within the pseudopotential) and that due to the pseudo-electrons (Fuchs et al, 1998).

The pseudopotential can be applied to a non-spherical system by projecting the state into l components, applying the pseudopotential and expanding back out, so that the potential becomes the non-local operator

$$V^{pseud} = \sum_{lm} |lm\rangle V_l^{pseud}(r)\langle lm| \tag{3.11}$$

where the projection and expansion correspond to multiplication by the lm spherical harmonic and integration over all angles, and summation over all lm respectively. In practice one component of the pseudopotential is generally defined as local (l independent) and the non-local parts defined in relation to this (as differences).

With the plane wave basis set (see equation 3.8) and applying the pseudopotential to the valence electrons only gives

$$\sum_{\mathbf{g}'} \left[\frac{\hbar^2}{2m} |\mathbf{k}+\mathbf{g}|^2 \delta_{\mathbf{g}\mathbf{g}'} + V_{pseud}(\mathbf{g},\mathbf{g}') + V_H(\mathbf{g}-\mathbf{g}') + V_{XC}(\mathbf{g}-\mathbf{g}') \right] C^n_{\mathbf{g}'}(\mathbf{k})$$

$$= \varepsilon^n(\mathbf{k}) C^n_{\mathbf{g}}(\mathbf{k}) \tag{3.12}$$

as the secular equation for the pseudo-states expanded in plane waves. Note that the external potential is no longer a function of the difference between reciprocal lattice vectors since the pseudopotential is non-local.

With the LDA and pseudopotential approximation, DFT can be applied to a wide range of large systems. Pseudo-states and total energies can be converged with this formulation for a far smaller number of plane waves within the basis set than for the full electron calculation - for LiH, a material with a relatively shallow potential, a 400 eV cutoff is required for a pseudopotential calculation, as opposed to 3300 eV for an all-electron calculation (Bellaiche and Kunc, 1997).

3.2.4 Total Energy Pseudopotential Calculation

The theory outlined above is the basis of the CAmbridge Serial Total Energy Package (CASTEP), which is employed in this thesis to calculate the pseudo-states for Aluminium and Silicon. These pseudo states are then used to obtain the Green function for the pseudo-system required to apply the embedding method described in chapter 2. In performing the calculation self-consistency is achieved by directly minimising the total energy of the system without resorting to direct matrix diagonalisation. This avoids a computationally costly matrix diagonalisation that yields all the available bands when only the occupied or partially occupied bands contribute to the charge density (see Payne et al, 1992).

However, to investigate the convergence of the Green function constructed from these pseudo-states with the number of bands included in its construction, it is desirable to have all of the states available for a given basis set. In view of this the states are obtained in two steps. Firstly the self-consistent potential is obtained using the standard iterative total-energy minimisation techniques. Secondly, this self-consistent potential is used to construct the associated secular equation, and the eigenstates obtained by matrix diagonalisation.

A plane wave basis set is chosen for this matrix diagonalisation that is characterised by the parameter E_{max}, so that the pseudo-states take the form

$$\Psi^n_{\mathbf{k}}(\mathbf{r}) = \sum_{|\mathbf{g}|^2 < E_{max}} C^n_{\mathbf{g}}(\mathbf{k}) e^{i(\mathbf{k}+\mathbf{g}).\mathbf{r}} \tag{3.13}$$

where $C^n_{\mathbf{g}}(\mathbf{k})$ are the eigenvector coefficients, and the same number of bands as reciprocal lattice vectors satisfying the condition of the sum are calculated[1]. The eigenvalues are denoted $E_n(\mathbf{k})$. It should be noted that the diagonalisation must be carried out for each $\mathbf{k}$ point so only a finite sampling of the band structure in $\mathbf{k}$ space is possible.

Properties of the band structure are important to the development of approximations to the Green function, as discussed in the rest of this chapter and chapter 4. In view of this the density of states and band structure resulting from the matrix

[1]This choice of plane wave basis set differs from the set used for determination of the self consistent potential and normally used for this type of calculation, $|\mathbf{k}+\mathbf{g}|^2 < E_{max}$. This choice is made to allow the application of the methods described in the rest of this chapter and chapter 4, such as the Brillouin zone integration (section 3.4.5) and the correction discussed in section 4.2.

diagonalisation for Al and Si (the materials core reconstruction is applied to) are shown in figures 3.1 and 3.2 for the FCC unit cell. The position of the critical points in the Brillouin zone are shown in figure 3.3. Parameters for the calculation are those given in chapter 4, where convergence of the Green function itself is discussed.

3.3 Obtaining the Green Function

Having presented the basis of theory on which the work rests, the next step is to establish how the Green function can be calculated from the Bloch states of equation (3.13).

The Green function associated with the Hamiltonian $\mathcal{H}$ is generally obtained either by solution of the defining equation

$$(\mathcal{H} - E)G(\mathbf{r}, \mathbf{r}'; E) = \delta(\mathbf{r} - \mathbf{r}') \tag{3.14}$$

through direct integration, or by applying the spectral representation

$$G(\mathbf{r}, \mathbf{r}'; E) = \sum_n \frac{\phi_n(\mathbf{r})\phi_n^*(\mathbf{r}')}{E - E_n} \tag{3.15}$$

where the sum is over all states in the complete set, ϕ_n, with eigenvalues E_n (Economou, 1990). This spectral representation is the result of expanding the Green function in the complete orthonormal set of eigenfunctions of the Hamiltonian. For a continuum of states this sum becomes an integral, usually carried out analytically by contour integration.

The Green function is analytic in the complex plane except where E is equal to the eigenvalues of the Hamiltonian. For discrete states $G(\mathbf{r}, \mathbf{r}'; E)$ possesses a simple pole, and for continuous states $G(\mathbf{r}, \mathbf{r}'; E)$ possesses a *branch cut* on the real axis. At this branch cut the Green function possesses two limiting values - the limit from the upper half plane gives the retarded Green function $G^+(\mathbf{r}, \mathbf{r}'; E)$ and from the lower half plane the advanced Green function $G^-(\mathbf{r}, \mathbf{r}'; E)$ (Economou, 1990).

The defining equation (3.14) has an important consequence for the spatial behaviour of the Green function. Due to the delta function on the RHS of the equation integration of the equation leads to a step function in the derivative, and

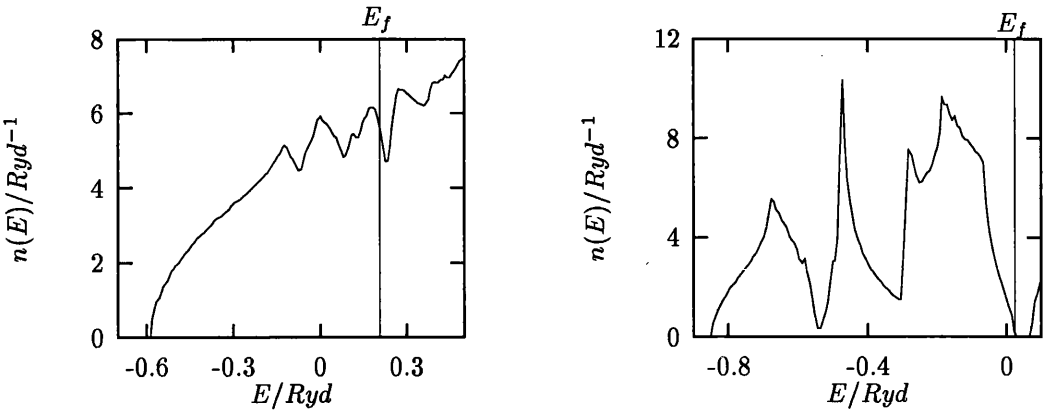

Figure 3.1: DOS for Aluminium and Silicon

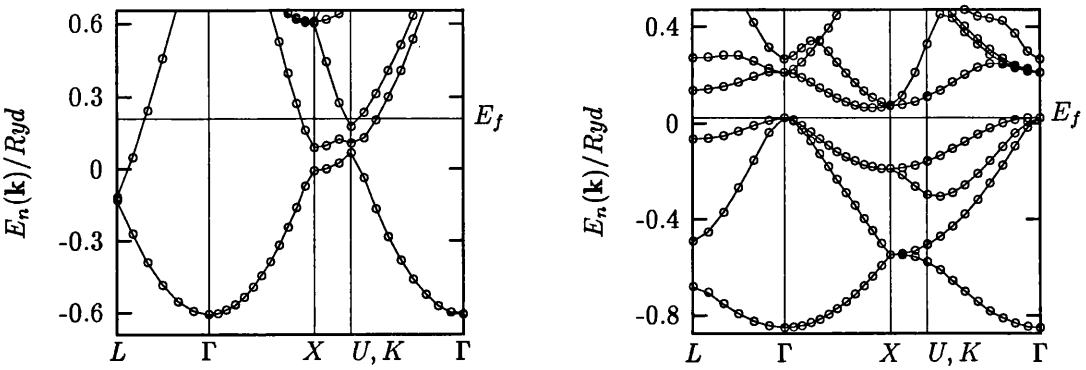

Figure 3.2: Band structure for Aluminium and Silicon

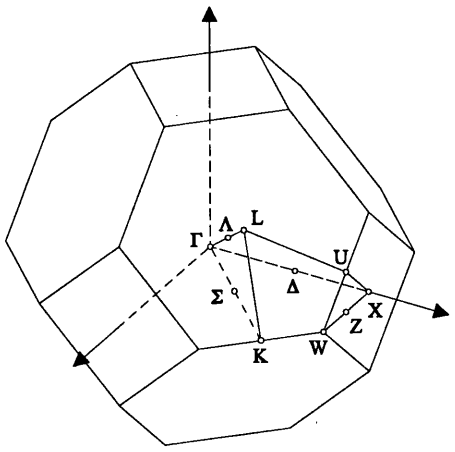

Figure 3.3: FCC Brillouin zone

so to a cusp in the function itself. This is not immediately apparent from the spectral representation, and for the spectral representation to possess this cusp the set of eigenstates in the sum must be complete. Ensuring this is the case when approximating the function is dealt with in chapter 4.

In the rest of this chapter, and the following chapter, the spectral representation is applied to obtain an approximation to the Green function from the eigenstates produced by a total energy pseudopotential calculation. The total energy calculations of interest are for periodic systems, so the eigenstates form an infinite number of continuum bands. It is the numerical evaluation of the spectral representation for this continuum of states that is addressed.

3.3.1 Spectral Representation for Bloch States

For the periodic system the states are characterised by two quantum numbers, the discrete band index n and the continuous crystal momentum $\mathbf{k}$. Since $\mathbf{k}$ is limited to the 1st Brillouin zone and is continuous, and there are an infinite number of bands, the spectral representation takes the form

$$G(\mathbf{r},\mathbf{r}';E) = \sum_n \int_{BZ} \frac{\Psi^n_{\mathbf{k}}(\mathbf{r})\Psi^{n*}_{\mathbf{k}}(\mathbf{r}')}{E - E_n(\mathbf{k})} d^3\mathbf{k} \tag{3.16}$$

where $\Psi^n_{\mathbf{k}}(\mathbf{r})$ is the Bloch state, $E_n(\mathbf{k})$ is its eigenenergy and E is complex. For a discrete set of states the spectral representation is easily applied as a sum (admittedly over an infinite number of states for a complete set, but the important fact is that these states have a finite separation in energy). Unfortunately for the periodic lattice not only is the number of states infinite, but within a given energy interval (within a band) there is also an infinite number of states - hence the Brillouin zone integral. This is a problem since any calculation can only provide states at a finite number of $\mathbf{k}$ points, and a finite number of bands.

In view of these limitations in the avaliable states the approximation of the spectral representation falls naturally into two parts - approximating the Brillouin zone integral from a finite number of points, and approximating the infinite band sum. Finding a good approximation to the integral present in the spectral representation (equation(3.16)) is the main concern of this chapter, with the approximation to the infinite sum the subject of chapter 4.

At this point the explicit form of the Green function expanded in spherical harmonics is presented. This is defined by the equation

$$G(\mathbf{r},\mathbf{r}';E) = \sum_{LL'} Y^*_{L'}(\hat{\mathbf{r}}')\mathcal{G}_{L,L'}(r,r';E)Y_{L'}(\hat{\mathbf{r}}) \tag{3.17}$$

where Y_L is the spherical harmonic of index $L = (lm)$, and $\mathcal{G}_{L,L'}(r,r';E)$ is the matrix representation of the Green function at radii r and r' and energy E.

The next few sections describe the calculation of this matrix by the following steps:

- Expansion of the Bloch states from the total energy pseudopotential calculation ($\Psi^n_{\mathbf{k}}(\mathbf{r})$) in spherical harmonics (section 3.3.2).
- Evaluation of the imaginary part of the Green function on the real axis, referred to in what follows as the *spectral function* (section 3.4).
- Performing a numerical Hilbert transform on the spectral function to obtain the Green function at the required energies on the surface of a sphere as a spherical harmonic expansion in the form of equation (3.17) (section 3.5).

The reasoning leading to this method is also given, together with a comparison with a far simpler method for performing the integral. The major factors that effect convergence of the Brillouin zone integral are also discussed.

3.3.2 The Pseudo-States Expanded in Spherical Harmonics

The set of pseudo-states are obtained from the self consistent potential by direct diagonalisation at the required $\mathbf{k}$, and are in the form

$$\Psi^n_{\mathbf{k}}(\mathbf{r}) = \sum_{\mathbf{g}} C^n_{\mathbf{g}}(\mathbf{k})e^{i(\mathbf{k}+\mathbf{g}).\mathbf{r}} \tag{3.18}$$

where $C^n_{\mathbf{g}}(\mathbf{k})$ are the expansion coefficients, n is the band index and $\mathbf{k}$ is the crystal momentum. As these are the result of matrix diagonalisation the number of bands is equal to the number of reciprocal lattice vectors. The coefficients of

the expansion in terms of spherical harmonics,

$$\Psi^n_{\mathbf{k}}(\mathbf{r}) = \sum_L \alpha^{(n)}_L(r,\mathbf{k}) Y_L(\hat{\mathbf{r}}) \tag{3.19}$$

where $L = (lm)$, the combined index of the spherical harmonic Y_L, can be found using the identity (Morse & Feshbach, 1953)

$$e^{i\mathbf{q}.\mathbf{r}} = 4\pi \sum_L i^l j_l(qr) Y^*_L(\hat{\mathbf{q}}) Y_L(\hat{\mathbf{r}}) \tag{3.20}$$

hence

$$\alpha^{(n)}_L(r,\mathbf{k}) = 4\pi i^l \sum_{\mathbf{g}} j_l(|\mathbf{k}+\mathbf{g}|r) Y^*_L(\widehat{\mathbf{k}+\mathbf{g}}) C^n_{\mathbf{g}}(\mathbf{k}). \tag{3.21}$$

The outward normal derivative of this will also be required since the derivative of the Green function is required (see section 2.1.2). This is just the derivative of this expression with respect to r. Using this expansion and the spectral representation (equation(3.16)), the matrix elements of the Green function become

$$\mathcal{G}_{L,L'}(r,r';E) = \sum_n \int_{BZ} \frac{\alpha^{(n)}_L(r,\mathbf{k}) \alpha^{(n)*}_L(r',\mathbf{k})}{E - E_n(\mathbf{k})} d^3\mathbf{k}. \tag{3.22}$$

3.4 Brillouin Zone Integration

The evaluation of the Brillouin zone integral in equation (3.22) is now addressed. In what follows the sum over band states is included in all expressions for the Green function, but the problem of evaluating this sum over the infinite number of bands is not addressed until the next chapter.

3.4.1 Applying Symmetry to Reduce the Volume of Integration

Obtaining the band states at each $\mathbf{k}$ point is computationally expensive, so it is desirable to be as efficient as possible in the use of the states calculated from the total-energy calculation. In view of this the integral over the whole Brillouin zone in equation (3.22) is reduced to an integral over a subsection of the Brillouin zone, using the symmetry of the lattice. The complete integral is obtained from

this reduced integral, allowing the number of **k** points to be kept to a minimum. The subdomain that is related to the whole Brillouin zone is referred to as the *irreducible wedge* and the symmetry properties employed are those of the Bloch states and eigenfunctions, described by the *space group* of the crystal (Wigner, 1959). The space group is the group of spatial transformations that map the atoms of the lattice onto themselves - they leave the lattice unchanged. The FCC Brillouin zone and irreducible wedge (as appropriate for bulk Al and Si, which are the materials investigated in chapter 4 and 5) are shown in figure 3.3.

The basic idea is to take the state at one **k** point and to obtain the states at all the points related to this by the symmetry of the Brillouin zone - these are the *equivalent points* of the Brillouin zone. This allows the integral over the irreducible wedge to be related to the complete integral.

For a given unit cell a general space group operator can be denoted (Altmann, 1991)

$$\{P|\mathbf{w}\}\mathbf{r} = P\mathbf{r} + \mathbf{w} \tag{3.23}$$

where P is a unitary transformation (it leaves one point in the unit cell invariant) and $\mathbf{w}$ is a vector (translation by a vector within the unit cell). All space group operators can be written in this form, and for symmorphic space groups $\mathbf{w} = 0$. The group of transformations P form the *point group*, and the space group and point group are equivalent for a symmorphic space group.

To find the expression for the states at equivalent points in **k** space the symmetry of the Bloch eigenfunctions in real space must be related to the symmetry in reciprocal space. These are related by (Altmann, 1991)

$$\{P|\mathbf{w}\}\Psi^n_{\mathbf{k}} = \Psi^n_{P\mathbf{k}} \tag{3.24}$$

and the energies of the states by

$$E_n(\mathbf{k}) = E_n(P\mathbf{k}). \tag{3.25}$$

This states that eigenvalues at the equivalent points of the Brillouin zone are equal, but the eigenstates need more work.

To obtain the $\Psi^n_{P\mathbf{k}}$ from the above expression we shall examine the explicit form of the Bloch states obtained using the plane wave basis set. After the relations for this expansion are derived the associated relationship for the states expanded in

spherical harmonics follows directly.

Taking the plane wave representation of the Bloch states,

$$\Psi^n_{\mathbf{k}} = \sum_{\mathbf{g}} C^n_{\mathbf{g}}(\mathbf{k}) e^{i(\mathbf{k}+\mathbf{g}).\mathbf{r}}, \tag{3.26}$$

and using equation (3.24) leads to

$$\Psi_{\mathbf{k}} = \{P|\mathbf{w}\}^{-1}\Psi_{P\mathbf{k}} \tag{3.27}$$

or

$$\Psi_{\mathbf{k}} = \{P^{-1}| - P^{-1}\mathbf{w}\}\sum_{\mathbf{g}} C_{\mathbf{g}}(P\mathbf{k}) e^{i(P\mathbf{k}+\mathbf{g}).\mathbf{r}} \tag{3.28}$$

with the inverse expressed in a slightly different form (substitution proves the expression for the inverse space group operator). The space group transformation acting on the real space variable gives

$$\Psi_{\mathbf{k}} = \sum_{\mathbf{g}} C^n_{\mathbf{g}}(P\mathbf{k}) e^{i(P\mathbf{k}+\mathbf{g}).P^{-1}(\mathbf{r}-\mathbf{w})}. \tag{3.29}$$

If each vector in the dot product is premultiplied by P (unitary transformation of two vectors does not effect their dot-product) and $\mathbf{g}$ is replaced with $P\mathbf{g}$ (this does not effect the sum) then we obtain

$$\Psi_{\mathbf{k}} = \sum_{\mathbf{g}} C^n_{P\mathbf{g}}(P\mathbf{k}) e^{iP^2(\mathbf{k}+\mathbf{g}).(\mathbf{r}-\mathbf{w})}. \tag{3.30}$$

If this is expanded in the form

$$\Psi^n_{\mathbf{k}'} = \sum_{\mathbf{g}'} C^n_{\mathbf{g}'}(\mathbf{k}') e^{i(\mathbf{k}'+\mathbf{g}').\mathbf{r}} \tag{3.31}$$

then the coefficients are given by

$$C^n_{\mathbf{g}'}(\mathbf{k}') = C^n_{P\mathbf{g}}(P\mathbf{k}) e^{-iP^2(\mathbf{k}+\mathbf{g}).\mathbf{w}} \delta\left[P^2(\mathbf{k}+\mathbf{g}) - (\mathbf{k}'+\mathbf{g}')\right]. \tag{3.32}$$

From this the coefficients for a state at $P\mathbf{k}$ in terms of the coefficients of a state at $\mathbf{k}$ are given by

$$C^n_{P\mathbf{g}}(P\mathbf{k}) = C^n_{\mathbf{g}}(\mathbf{k}) e^{-iP(\mathbf{k}+\mathbf{g}).\mathbf{w}}. \tag{3.33}$$

The next step is to find the coefficients of the spherical harmonic expansion of the

state at $P\mathbf{k}$, $\alpha_L^{(n)}(r, P\mathbf{k})$. This is easily achieved by using equation (3.33) in the expansion of the state in spherical harmonics, equation (3.21), to give

$$\alpha_L^{(n)}(r, P\mathbf{k}) = 4\pi i^l \sum_{\mathbf{g}} j_l(|\mathbf{k}+\mathbf{g}|r_s) Y_L^*[\widehat{P(\mathbf{k}+\mathbf{g})}] C_{\mathbf{g}}^n(\mathbf{k}) e^{-iP(\mathbf{k}+\mathbf{g}).\mathbf{w}}. \tag{3.34}$$

Since the set of spherical harmonics with one l value form a *complete representation* of the three dimensional unitary transformation group (Altmann, 1991), the point group operator, P, acting on a spherical harmonic Y_{lm} can be expressed as a linear superposition of spherical harmonics of the same l,

$$Y_L(P\hat{\mathbf{r}}) = \sum_{L'} \mathcal{U}_{LL'}^{(P)} Y_{L'}(\hat{\mathbf{r}}) \tag{3.35}$$

where $\mathcal{U}^{(P)}$ is the matrix representation of the point group operator P in the basis of spherical harmonics, and is block diagonal (zero for $l \neq l'$).

From this we can see that equation (3.34) becomes

$$\alpha_L^{(n)}(r, P\mathbf{k}) = \sum_{L'} 4\pi i^{l'} \sum_{\mathbf{g}} j_{l'}(|\mathbf{k}+\mathbf{g}|r_s) \mathcal{U}_{LL'}^{(P)} Y_{L'}^*(\widehat{\mathbf{k}+\mathbf{g}}) C_{\mathbf{g}}(\mathbf{k}) e^{-iP(\mathbf{k}+\mathbf{g}).\mathbf{w}}. \tag{3.36}$$

The matrices $\mathcal{U}^{(P)}$ can be constructed from standard formulae, and a description of how this is achieved is given in appendix A.

Symmorphic Space Group

For the symmorphic space group ($\mathbf{w} = 0$ for all symmetry operations) obtaining the coefficients at $P\mathbf{k}$ is simply a matter of matrix multiplication, so

$$\alpha_L^{(n)}(r, P\mathbf{k}) = \sum_{L'} \mathcal{U}_{LL'}^{(P)} \alpha_L^{(n)}(\mathbf{k}). \tag{3.37}$$

If $\mathcal{G}^{IW}$ is the spectral representation of the Green function matrix including contributions from the irreducible wedge only,

$$\mathcal{G}_{LL'}^{IW} = \sum_n \int_{IW} d^3\mathbf{k} \frac{\alpha_L^{(n)}(\mathbf{k}) \alpha_{L'}^{(n)*}(\mathbf{k})}{E - E_n(\mathbf{k})} \tag{3.38}$$

then the integral over the whole Brillouin zone can be written as a double matrix

multiplication

$$\mathcal{G}_{LL'} = \sum_{P} \sum_{NN'} \mathcal{U}^{(P)}_{LN} \mathcal{U}^{(P)*}_{L'N'} \mathcal{G}^{IW}_{NN'} \tag{3.39}$$

where the sum over P denotes a sum over the point group of the structure (the sum provides the contribution from all the equivalent points). This is the required expression for the symmorphic case.

Non-Symmorphic Space Group

For a non-symmorphic space group the $\mathbf{w}$ dependent phase factor in equation (3.36) complicates the situation. In this case the process can be reduced to calculating functions (normally a few) of the form

$$\alpha^{(n)}_L(r, P\mathbf{k}) = 4\pi i^l \sum_{\mathbf{g}} j_l(|\mathbf{k}+\mathbf{g}|r_s) Y^*_L(\widehat{\mathbf{k}+\mathbf{g}}) C^n_{\mathbf{g}}(\mathbf{k}) e^{-iP\mathbf{g}.\mathbf{w}}. \tag{3.40}$$

where the $\mathbf{k}$ vector in the dot product does not need to be included as it cancels in the spectral representation. The same procedure as that given for the symmorphic case is followed for each of these, summing over only those point group operations associated with the $\mathbf{w}$ vector. These are then summed to give the complete spectral representation.

Only a small number of expressions of the form equation (3.40) need be evaluated as the phase factor generally reduces to a simple form - for Si two such expressions are necessary.

This method reduces the volume over which the integration must be made by a significant factor (48 for a FCC unit cell) and reduces the required number of $\mathbf{k}$ points by a similar factor.

3.4.2 Discretisation of the Integral over the Irreducible Wedge

Discretisation of the integral in equation (3.38) consists of choosing a set of $\mathbf{k}$ points in the irreducible wedge and replacing the integral with a sum of the value

of the integrand at these points with appropriate weighting, ie

$$G^{IW}(\mathbf{r},\mathbf{r}';E) \approx \sum_n \sum_j W_j \frac{\Psi^n_{\mathbf{k}_j}(\mathbf{r})\Psi^{n*}_{\mathbf{k}_j}(\mathbf{r}')}{E - E_n(\mathbf{k}_j)} \tag{3.41}$$

where $\mathbf{k}_j$ are the chosen $\mathbf{k}$ points, and W_j are the chosen weights.

Two different schemes (corresponding to different $\mathbf{k}$ point sets and weights) are investigated in what follows. The first of these is a simple zero-order method which weights the contribution from each $\mathbf{k}$ point by the volume in $\mathbf{k}$ space associated with it. For the second method the numerator and denominator of the integrand are interpolated between $\mathbf{k}$ points and the integral carried out using this interpolating function. This corresponds to the weights in equation (3.41) being functions of the complex energy E.

3.4.3 Zero Order Integration Scheme

The properties of different $\mathbf{k}$ point sets for Brillouin zone integration has received attention in the literature (Monkhorst and Pack, 1976; Chadi and Cohen 1973). Monkhorst and Pack provide a method of selecting a set of *special points* within the irreducible wedge that are optimised for the description of the electron states. Firstly a brief description of the set of points described by Monkhorst and Pack is given, and then this is applied to the evaluation of the Brillouin Zone integral for a free electron.

If the sequence of numbers

$$u_r = (2r - q - 1)/2q \quad r = 1 \ldots q \tag{3.42}$$

is defined, where q is an integer parameter (this will control the size of the set of points), then a set of points $\mathbf{k}_j$ is given by

$$\mathbf{k}_j = u_r\mathbf{b}_1 + u_s\mathbf{b}_2 + u_t\mathbf{b}_3 \tag{3.43}$$

where $j = r + (s-1)q + (t-1)q^2$, and the basis vectors are the reciprocal lattice unit vectors. This defines a set of $N_k = q^3$ points that evenly cover the Brillouin zone and possess the point group symmetry of the lattice. This set of points has no members at the origin or on the Brillouin zone faces.

To find the integral over the irreducible wedge only the points in this set that are within the irreducible wedge (or on its boundaries) are required. The weights of each point are taken to be proportional to the *volume* associated with each point. This gives the set of weights

$$W_j = w_j \frac{\mathbf{b}_1.\mathbf{b}_2 \times \mathbf{b}_3}{q^3} \tag{3.44}$$

where the triple product gives the volume of the parallelepiped surrounding $\mathbf{k}_j$ (the sum of these volumes fill the Brillouin zone exactly). The term w_j takes into account the fact that the integration is over the irreducible wedge only and is the fraction of the parallelepiped volume within the wedge. For $\mathbf{k}$ outside the irreducible wedge $w_j = 0$, for $\mathbf{k}$ inside it $w_j = 1$ and for $\mathbf{k}$ on the surface of the irreducible wedge an appropriate value is obtained from the geometry (eg for $\mathbf{k}$ on a plane surface $w_j = \frac{1}{2}$).

Using this set of $\mathbf{k}$ points and this weighting scheme gives

$$\mathcal{G}^{IW}_{LL'}(r, r'; E) \approx \sum_n \sum_j W_j \frac{\alpha^{(n)}_L(r, \mathbf{k}_j)\alpha^{(n)*}_{L'}(r', \mathbf{k}_j)}{E - E_n(\mathbf{k}_j)} \tag{3.45}$$

a straightforward approximation of the integral.

Unfortunately this method possesses a major drawback. Since the weights are energy independent the approximation to the Green function given by this expression has the same analytic form as a Green function for a system with only discrete states - in other words it consists of poles on the real energy axis at the eigenvalues of the available states and does not possess a branch cut. Although this converges to a continuum in the limit $n_{\mathbf{k}} \to \infty$, the convergence is slow and for finite $n_{\mathbf{k}}$ gives a 'spiky' approximation to the Green function.

In order to demonstrate this a jellium Green function is calculated using this approximation for an empty lattice. Figure 3.4 shows the real and imaginary parts of the $(L, L') = (00, 00)$ element of a free electron Green function calculated with

$$\begin{aligned} C^n_{\mathbf{g}}(\mathbf{k}) &= \delta(\mathbf{g} - \mathbf{g}_n) \\ E_n(k) &= |\mathbf{k} + \mathbf{g}_n|^2 - V_0 \end{aligned} \tag{3.46}$$

where g_n is a reciprocal lattice vector associated with band n and V_0 is the bottom of the first band.

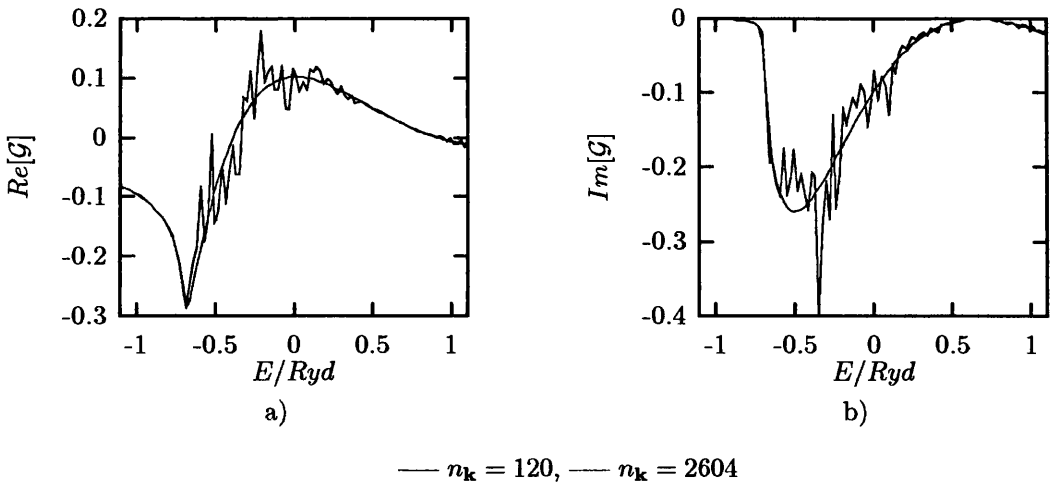

Figure 3.4: Free electron $\mathcal{G}_{(00,00)}$ from the zero order method.

A simple cubic lattice was used with a lattice spacing of $a = 4.05\mathring{A}$ (the value for Aluminium) and $q = 8$ (120 points within the irreducible wedge), and the imaginary part of the energy E, denoted ε, is 0.1 eV. The other parameters take the values $V_0 = -9.365$ eV, $r = r' = a_0\sqrt{2}/4$ the FCC touching spheres radius and $E_{max} = 100$ eV. A converged result (for this ε) is also shown corresponding to $q = 24$ (2604 points in the IW).

The sum does converge faster for increasing imaginary parts of the energy (good convergence is achieved when the imaginary part of E is greater than the largest energy difference between the eigenvalues in a band) however the Green function is required for imaginary energies around 0.1 eV (this will be justified chapter 5).

3.4.4 Continuity in Energy Space: Linear Interpolation in k Space and the Spectral Function

An improved method for the calculation of the spectral representation should take into account continuity of the band structure. It is the disregard of this property that gives the physically unrealistic approximation of the zero order method. In addition it would be desirable to apply a higher order scheme to the variation of the eigenfunctions themselves. Expressed in terms of the weights in the discretisation (equation (3.41)) this implies that the weights W_j are functions of the complex energy E.

The basis of the method is to perform a linear interpolation of the numerator (the

product of the two Bloch states) over **k** space and a similar linear interpolation of the denominator (the band structure). Integration of this continuous bilinear function would then provide the weights required. Lambin and Vigneron (1984) applied exactly this approach to obtain the energy dependent weights.

An alternative method of evaluating this integral using linear interpolation in **k** space is given here. This involves two steps. First the imaginary part of the Green function on the real axis is evaluated, hereafter referred to as the spectral function. This quantity is easier to evaluate than the Green function integral itself as its value at a given energy depends only on the band structure at that energy. The Green function at the required complex energies are derived from this using a convolution integral - the Hilbert transform that relates the real and imaginary parts of a Green function (Economou, 1990) and allows the Green function at any complex energy to be obtained from the imaginary part of the Green function on the real axis.

The spectral function is obtained from the eigenstates by a 3D linear interpolation in the Brillouin zone. The value of this function at a given energy depends only on the states of that energy (unlike the real part of the Green function, or the imaginary part at complex energy). As a consequence of this locality of the energy dependence the Brillouin zone integral takes the form of a surface integral, which can be evaluated in a straightforward manner.

This spectral density function, $f(\mathbf{r},\mathbf{r}';E) = Im\,[G(\mathbf{r},\mathbf{r}';E)]$ is given generally by the expression (Economou, 1990)

$$f(\mathbf{r},\mathbf{r}';E) = \sum_i \langle \mathbf{r}|\Psi_i\rangle\langle\Psi_i|\mathbf{r}'\rangle\delta(E_i - E) \tag{3.47}$$

where E_i is the eigenvalue of state Ψ_i, and i is the quantum number of the state. The local value ($\mathbf{r} = \mathbf{r}'$) of f is the local density of states, and E is on the real axis.

This density function is related to the Green function by the integral equation

$$G(\mathbf{r},\mathbf{r}';E+i\varepsilon) = \int_{-\infty}^{\infty} dE' \frac{f(\mathbf{r},\mathbf{r}';E')}{E+i\varepsilon-E'}. \tag{3.48}$$

Equation (3.47) can be written as an integral over a surface of constant energy in **k** space due to the delta function. This gives the form (with $\mathcal{F}_{LL'}$ the matrix

coefficients of f expanded in spherical harmonics)

$$\mathcal{F}_{LL'}(E) = \sum_n \int_{E=E_n(\mathbf{k})} \frac{\alpha_L^{(n)}(r,\mathbf{k})\alpha_{L'}^{(n)*}(r',\mathbf{k})}{|\nabla_{\mathbf{k}} E|} dS \tag{3.49}$$

where the $|\nabla_{\mathbf{k}} E|$ results from the integration element changing from a volume element to a surface element (Lehmann & Taut, 1972).

This integration can be approximated from a finite number of $\mathbf{k}$ points by interpolating both the product of wavefunctions, and the eigenvalues between the available $\mathbf{k}$ points. Surface integration is then carried out using this interpolated function. This interpolation and integration is the linear analytic tetrahedron method (Jepson & Anderson, 1971; Lehmann & Taut, 1972; MacDonald, 1979; Rath & Freeman, 1975; Kaprzyk and Mijnarends, 1986).

3.4.5 The Linear Analytic Tetrahedron Method

In order to evaluate the surface integral an appropriate set of $\mathbf{k}$-points must be chosen, and the interpolating functions must be derived.

For a mesh of points in 3-dimensions with data values defined at each point a continuous interpolating function can only be constructed for a linear interpolation. The data values at each point take the form of the band energy, $E_n(\mathbf{k})$ and the product of the Bloch states in the integrand of equation (3.49). For this case the interpolating function at a general point is defined by the 4-mesh points nearest to it. Another way to view this is that the irreducible wedge is divided into tetrahedra with a linear interpolation of the functional values carried out between the 4 corners of each tetrahedron, giving a continuous function throughout the mesh. Higher order methods are available, but these have the drawback that the interpolated function is not continuous and it is not clear that anything would be gained from using these techniques. There is significant increase in the geometrical complexity in moving to a higher order scheme and, although higher order techniques have been applied to the calculation of density of states, the generalisation to the calculation of the spectral function required here is not trivial (Methfessel et al, 1987).

An appropriate set of $\mathbf{k}$ points for this method would divide the irreducible wedge

into tetrahedra that entirely fill the wedge. A suitable mesh of points is given by

$$u_r = (2r - q - 1)/2(q - 1) \quad r = 1 \ldots q$$

$$\mathbf{k}_j = u_r \mathbf{b}_1 + u_s \mathbf{b}_2 + u_t \mathbf{b}_3 \tag{3.50}$$

where the basis vectors are the reciprocal lattice vectors. This set of vectors has members on the surface of the Brillouin zone, and for q odd $\mathbf{k}$ points fall at the origin and along the major axes of the reciprocal lattice. As a consequence of this the BZ can be subdivided into tetrahedra, and (for the simple cubic and FCC case at least) the irreducible wedge can be subdivided into tetrahedra.

The surface integral in equation (3.49) is approximated as a sum of contributions from each tetrahedron in the Brillouin zone and each band (suppressing the matrix indices for clarity)

$$\mathcal{F}_{LL'}(E) = \sum_n \sum_t i_t^n(E) \tag{3.51}$$

where t is the index of a tetrahedron in the irreducible wedge and $i_t^n(E)$ is the contribution from the n^{th} band and the t^{th} tetrahedron.

The contribution from each tetrahedron (and band) is dependent only on the interpolating functions within that tetrahedron, so i takes the form (suppressing the band and tetrahedron indices)

$$i(E) = \int_{E=E(\mathbf{k})} \frac{\mu(\mathbf{k})}{|\nabla_{\mathbf{k}} \varepsilon(\mathbf{k})|} dS. \tag{3.52}$$

where the integral is taken to be non-zero only inside the tetrahedron. The numerator $\mu(\mathbf{k})$ is the interpolant of the *product* of the wavefunctions ($\alpha_L^{(n)} \alpha_{L'}^{(n)*}$) and $\varepsilon(\mathbf{k})$ is the interpolant of the eigenvalues within the tetrahedron.

These interpolating functions are the next consideration. If the corners of the tetrahedron are indexed $\mathbf{k}_0$ to $\mathbf{k}_3$ then the values of μ and ε at the corners are given by

$$\mu_i = \alpha_L^{(n)}(\mathbf{k}_i) \alpha_{L'}^{(n)*}(\mathbf{k}_i) \tag{3.53}$$

and

$$\varepsilon_i = E_n(\mathbf{k}_i) \tag{3.54}$$

where from here on it is assumed that the indices are ordered in increasing energy, $\varepsilon_0 < \varepsilon_1 < \varepsilon_2 < \varepsilon_3$ (see figure 3.5).

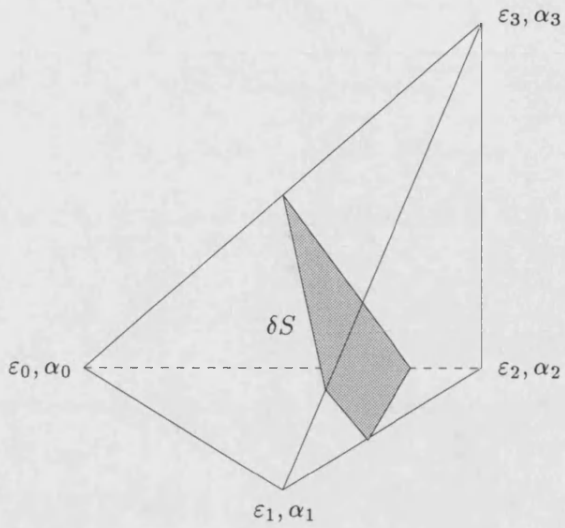

Figure 3.5: One tetrahedron spanned out by the vectors $\mathbf{0}$, $\mathbf{k}_1$, $\mathbf{k}_2$ and $\mathbf{k}_3$. δS is a plane of constant energy.

The interpolating functions are obtained from the μ_i and ε_i values and can be written as

$$\mu(\mathbf{k}) = a_0 + \mathbf{a}.\mathbf{k} \tag{3.55}$$

and

$$\varepsilon(\mathbf{k}) = b_0 + \mathbf{b}.\mathbf{k} \tag{3.56}$$

with a_0, $\mathbf{a}$, b_0 and $\mathbf{b}$ parameters. These parameters are obtained by solving the simultaneous equations

$$\mu_i = a_0 + \mathbf{a}.\mathbf{k}_i \quad i = 0 \ldots 3 \tag{3.57}$$

for $\mathbf{a}$ and a_0, and

$$\varepsilon_i = b_0 + \mathbf{b}.\mathbf{k}_i \quad i = 0 \ldots 3 \tag{3.58}$$

for $\mathbf{b}$ and b_0.

If $\mathbf{k}_0$ is taken to be the origin (this simplifies the notation and the origin can transformed back following the derivation, keeping this general) and the vectors

$$\mathbf{r}_1 = \frac{\mathbf{k}_2 \times \mathbf{k}_3}{\mathbf{k}_1.\mathbf{k}_2 \times \mathbf{k}_3}, \quad \mathbf{r}_2 = \frac{\mathbf{k}_3 \times \mathbf{k}_1}{\mathbf{k}_1.\mathbf{k}_2 \times \mathbf{k}_3}, \quad \mathbf{r}_3 = \frac{\mathbf{k}_1 \times \mathbf{k}_2}{\mathbf{k}_1.\mathbf{k}_2 \times \mathbf{k}_3} \tag{3.59}$$

are defined, then the interpolation parameters (the solutions of equations (3.57)

and (3.58)) are given by

$$\begin{aligned} a_0 &= \mu_0, \quad \mathbf{a} = \textstyle\sum_i (\mu_i - \mu_0)\mathbf{r}_i \\ b_0 &= \varepsilon_0, \quad \mathbf{b} = \textstyle\sum_i (\varepsilon_i - \varepsilon_0)\mathbf{r}_i. \end{aligned} \tag{3.60}$$

With these the parameters equation (3.52) can be evaluated, leading to

$$i(E) = \frac{a_0}{|\mathbf{b}|} \int_{E=E(\mathbf{k})} 1 dS + \frac{1}{|\mathbf{b}|} \mathbf{a}. \int_{E=E(\mathbf{k})} \mathbf{k} dS \tag{3.61}$$

where the integral is over the plane of constant energy within the tetrahedron. For $\varepsilon_0 < \varepsilon < \varepsilon_1$ and $\varepsilon_2 < \varepsilon < \varepsilon_3$ this plane is a triangle, and for $\varepsilon_1 < \varepsilon < \varepsilon_2$ it is a quadrilateral (see figure 3.5).

The first integral in equation (3.61) is the area of this surface, and the second is the 1^{st} moment of this surface (Lehmann & Taut, 1972) so this integral is equivalent to the expression

$$i(\varepsilon) = \frac{1}{|\mathbf{b}|} (\text{ Area surface } \delta S) \, [\mu_0 + \mathbf{a}.(\text{centroid of } \delta S)] \tag{3.62}$$

where δS is the surface shown in figure 3.5. The area and 1^{st} moment can be calculated from geometry, and this integral is of course non-zero only for $\varepsilon_0 < \varepsilon < \varepsilon_3$.

This provides the contribution from each tetrahedron. The method is applied to all tetrahedra for all bands, and for each matrix element to obtain the matrix of the spectral function, $\mathcal{F}$.

3.4.6 Convergence with $n_{\mathbf{k}}$: Band Crossing and van Hove Singularities

For the LATM there are two major factors influencing the convergence with the number of $\mathbf{k}$ points ($n_{\mathbf{k}}$). These are the effect of bands crossing at high symmetry points in the Brillouin zone (Gilat, 1972; Cooke and Wood, 1973; Chen, 1977), and the inaccuracy of the linear interpolation at van Hove singularities (Boon et al, 1986).

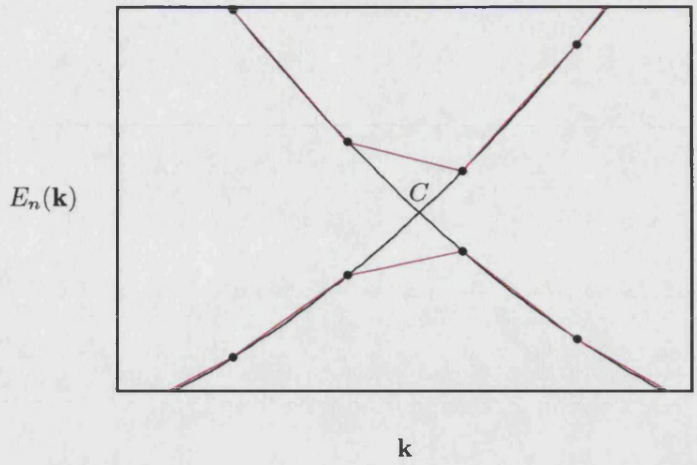

— Band structure, — linear interpolation of band structure from sample points ○.

Figure 3.6: Band structure near a degeneracy. The **k** axis is along a plane or line of symmetry in the BZ.

Band Crossing

Within the band structure bands may cross at high symmetry points in the Brillouin Zone, where the symmetry allows the degeneracy to take place (see figure 3.2). The bands must be identified in some way in order to associate a band index to each one and the integration carried out on each band. The only reasonable way to do this is to order the bands in increasing energy.

If this method is used problems occur when the bands cross. This band crossing must occur either on the surface of a tetrahedron, or at the corner points (at the points of higher symmetry than a general point in the Brillouin zone). In the first case the linear interpolation does not accurately describe the cusp in the band structure, and for both cases it does not describe the discontinuity in the Bloch states. Figure 3.6 schematically shows an example of this occurring, with the actual band structure and the linear interpolation of this band structure. In figure 3.2 the band structure for Aluminium is shown, and around the special point U, K it is apparent that the ordering of bands in terms of energy has prevented band crossing from occurring and introduced cusps in the band structure that are entirely artifacts of the interpolation scheme.

The effect of this on a Brillouin Zone integral can be illustrated by using the method to calculate a free electron spectral function from a reduced zone scheme

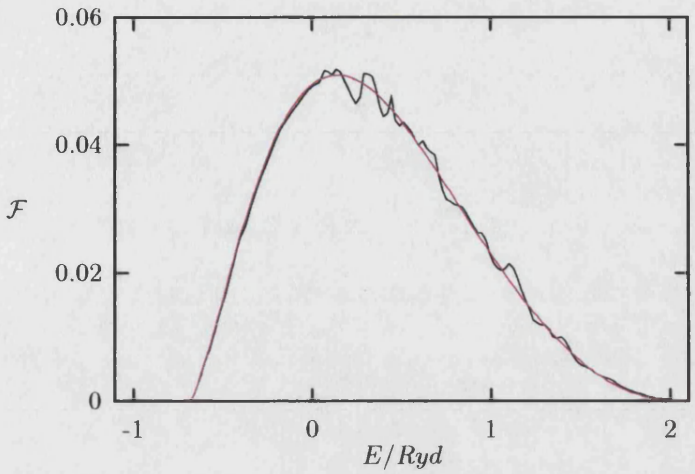

Figure 3.7: Free electron spectral function for bands ordered by energy or by associated reciprocal lattice vector. Matrix element shown is $\mathcal{F}_{(10,10)}$ for $n_{\mathbf{k}} = 89$.

(with the same parameters as figure 3.4, section 3.4.3) using the LATM. The band indices are chosen in two ways - from the reciprocal lattice vector associated with each free space Bloch state (each band is continuous) and by ordering in increasing energy (where discontinuities are introduced when bands cross). The two cases are illustrated in figure 3.7, where it is apparent that band crossing is a significant effect. The spectral function is shown for FCC free space (again with $a_0 = 4.05\mathring{A}$) and $n_{\mathbf{k}} = 89$ in the IW. Other parameters take the same values as for figure 3.4.

This effect could be avoided by using an *extrapolation* scheme for the integration within a tetrahedron (Müller and Wilkins, 1984). This would require the gradient of both $\varepsilon(\mathbf{k})$ and $\mu(\mathbf{k})$ at a point within the tetrahedron (by the **k.p** method, for example (Robertson and Payne, 1990)), and this gradient would be used for linear extrapolation to each corner of the tetrahedron. Provided the point within the tetrahedron possess no special symmetry no degeneracies will occur, so each band crossing will not result in discontinuities in the Bloch functions and the cusp will be represented with higher accuracy. This could give the same degree of convergence to the free electron calculation carried out with no band crossing, providing van Hove singularities are not important. Since this would require the gradient of both the band structure and Bloch states at each $\mathbf{k}$ point this method was not investigated here.

Van Hove Singularities

Van Hove singularities (Madelung, 1996) occur where $\nabla_{\mathbf{k}} E$ in equation (3.49) is zero, which takes place at band edges (see figure 3.2). At the analytic critical points where this occurs the energy derivative of any functions of the form (3.49) will possess singularities and a cusp will be present in the function itself.

This cusp cannot be represented by linear interpolation in reciprocal space, which will approximate this cusp by a rapidly oscillating function. Any scheme that employs linear interpolation of the band structure will suffer from this problem, which does not arise for quadratic interpolation schemes (Boon et al, 1986).

In the literature tests of the improvement over linear methods given by quadratic interpolation have been limited to density of states calculations and model systems where only one band has been considered. For the DOS calculations the effect of discontinuities in the Bloch states at a band crossing is irrelevant, and for only one band present no band crossing occurs anyway, hence these results do not prove the superiority of the quadratic interpolation over linear interpolation for the calculation of the spectral function.

The DOS for Aluminium and Silicon shown in figure 3.1 was calculated using the LATM method. It is apparent that the Silicon DOS shows some spurious structure at exactly the energies where band crossing occurs (see figure 3.2), whereas van Hove singularities appear to be well described. In view of this it seems reasonable to conclude that band crossing is the dominant cause of error in the LATM as applied here.

In the following section comparisons are made between convergence of the zero order method and the LATM for a lattice representation of a free electron gas with the bands ordered by increasing energy. This model system will exhibit the errors due to band crossing, which are expected to be greater than the equivalent errors for real materials since for real materials band crossing can only occur at critical points, whereas for a free electron its occurrence at any $\mathbf{k}$ is not prevented by symmetry. Note that band crossing does not influence the zero-order method since no interpolation takes place.

In the next chapter tests of convergence with $n_{\mathbf{k}}$ for the Green function are presented, for Al and Si pseudo-states resulting from the band structure calculations.

The LATM was found to be adequate for the calculations carried out here, and in chapter 5 the core reconstruction calculations can easily be converged for a reasonable number of **k** points - the final results were not sensitive to the fine structure of the spectral function.

3.5 The Green Function from the Spectral Function

This section describes the method used to transform the spectral function into the Green function for any complex energy E. This is essentially a generalisation of a similar procedure applied by Kuzmiak (Kuzmiak et al, 1991) to complex energy using a standard method for singular integrals (Davis and Rabinowitz, 1967).

3.5.1 The Convolution Integral

The Green function matrix expanded on the surface is given by the appropriate expression corresponding to equation (3.48)

$$\mathcal{G}_{LL'}(E) = \int_{-\infty}^{\infty} dx \frac{\mathcal{F}_{LL'}(x)}{E - x}. \tag{3.63}$$

In this expression x is real and is the energy variable of the spectral function, whereas E may be complex.

This integral is not easily evaluated by direct application of standard numerical schemes. For real E the integrand has a pole at $E = x$, and for the small imaginary parts required here the pole is close enough that the integrand has a narrow 'spike' at $E = x$ calling for a high sample point density. To obtain the integral by Simpson's rule, for instance, would require $\mathcal{F}(E)$ at an unrealistic number of energy values. Gaussian methods are another option, but since the position of the pole is a function of the integration variable the same problem arises.

In the method presented here the spectral function is calculated on a grid of energy values. Interpolating functions are defined between the values at these grid points, resulting in an interpolated approximation to the spectral function. Equation (3.63) is then evaluated for $\mathcal{F}_{LL'}$ represented by these interpolating functions, with

the contribution from the interpolation between adjacent grid points calculated analytically. This gives the Green function at the required energy.

At this point it should be noted that the limits for integration in equation (3.63) cover the entire real axis. Below the bottom of the lowest band there are no states, so $\mathcal{F}$ is zero below the minimum eigenvalue. A real system would have an infinite number of bands, which would be a problem. However the approximation described so far only includes a finite number of bands so $\mathcal{F}$ is zero above a maximum eigenvalue (the consequences of including only a finite number of bands are described in chapter 4). This means that the integral need only be taken over a finite energy range.

Polynomial functions are used here to interpolate the between values of $\mathcal{F}$. If the interpolating function between the energy values a and b is given by

$$f_{ab}(x) = a_0 + a_1 x + ... + a_m x^m \tag{3.64}$$

then the contribution to the integral in equation (3.63) from this range, g_{ab}, is given by

$$g_{ab}(E) = \int_a^b dx \frac{f_{ab}(x)}{E - x} \tag{3.65}$$

or

$$g_{ab}(E) = \sum_{i=0}^{m} a_m S^m(a, b; E) \tag{3.66}$$

where

$$S^m(a, b; E) = \int_a^b \frac{x^m}{E - x} dx. \tag{3.67}$$

Any functions can be used to represent $\mathcal{F}$ in this method provided that an integral of this form can be solved analytically.

For the case of polynomials this can be achieved by subtracting out the singularity to give (Davis and Rabinowitz, 1967)

$$S^m(a, b; E) = \int_a^b \frac{x^m - E^m}{E - x} dx + E^m \int_a^b \frac{1}{E - x} dx \tag{3.68}$$

which can be evaluated analytically. The first term on the LHS is in fact an integral of a polynomial, since the denominator is factor of the numerator. The moments, $S^m(a, b; E)$, are given in Table 3.1 for $m = 0 \ldots 3$, and are shown in figure 3.8.

Care must be taken in the application of this expression, due to a delicate numerical

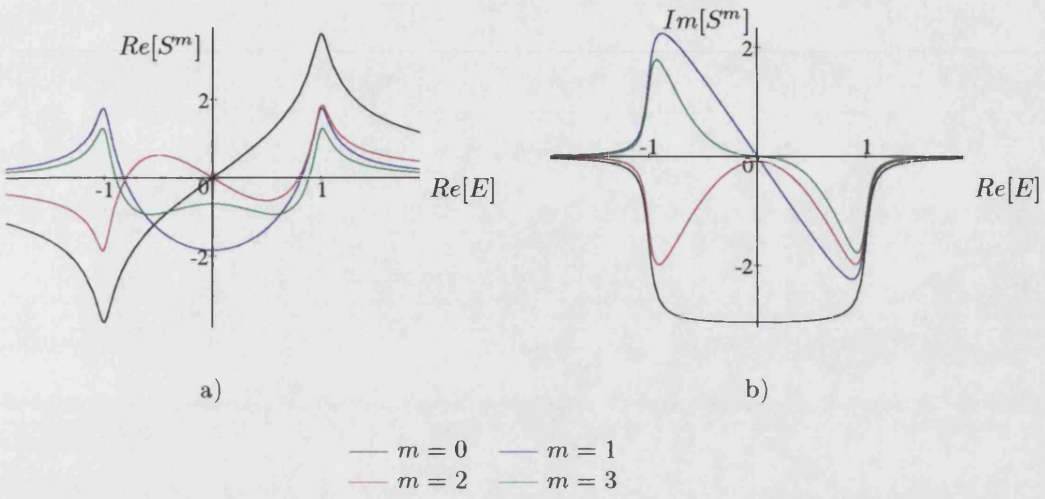

Figure 3.8: Moments of the Hilbert kernel, S^m, for $a = -1$, $b = 1$. The imaginary part of E is 0.1.

cancellation between the first and second integrals in equation (3.68). Each of these can be expanded as a series for $|\frac{x}{E}| \leq 1$ to give

$$\int_a^b \frac{x^m - E^m}{E - x} dx = \sum_{n=1}^{m} \frac{1}{n}(b^n - a^n)E^{m-n} \tag{3.69}$$

and

$$E^m \int_a^b \frac{1}{E - x} dx = -\sum_{n=1}^{\infty} \frac{1}{n}(b^n - a^n)E^{m-n}, \tag{3.70}$$

where it is apparent that the first integral is a polynomial in E, and the second is the sum of a polynomial in E and a power series in $1/E$. It is also apparent that the polynomial terms in the second integral cancel exactly with the polynomial terms in the first integral, so the moment S^m tends to zero as $1/E$ for $E \to \infty$.

m	$S^m(a, b; E)$
0	S^0
1	$(a - b) + ES^0$
2	$(a^2 - b^2)/2 + (a - b)E + E^2S^0$
3	$(a^3 - b^3)/3 + E(a^2 - b^2)/2 + E^2(a - b) + E^3S^0$

$$S^0 = \ln\left(\frac{E - a}{E - b}\right)$$

Table 3.1: Moments of the Hilbert kernel the over interval a-b. E may be complex.

Since each integral will be calculated separately, care must be taken to ensure that they are calculated accurately enough for this cancellation to occur for E a long way from a or b, where the polynomial terms will take large values. For the lower order terms ($m = 0, 1$) this causes no problem, but for higher order moments the cancellation of the higher order polynomials is sensitive to small errors.

3.5.2 Errors Due to the Polynomial Interpolation of $\mathcal{F}$

Describing the spectral function as a sum of interpolating polynomials will provide an accurate approximation provided a Taylor expansion for $\mathcal{F}$ is valid between sample energies. Unfortunately this is not the case since $\mathcal{F}$ possesses van Hove singularities - its behaviour at the top and bottom of bands is inherently $\propto E^{\frac{1}{2}}$. However this does not cause significant errors in the calculation of the Green function since the influence of these feature is smoothed out for finite imaginary energy. The convergence of the methods with the spacing of sample points along the axis will be examined in the next chapter.

The method described above would give exactly the same results as that given by Lambin and Vigneron (1984) if the convolution integral (equation 3.63) was carried out exactly for the $\mathcal{F}$ resulting from linear interpolation in $\mathbf{k}$ space, and not for a polynomial interpolation of this function. The main advantage of the method presented here is of greater flexibility in the degree of approximation applied, so minimising the computational effort. The method of Lambin and Vigneron accurately describes the contribution to the Green function from each region of $\mathbf{k}$ space and each band, with no account taken of whether the contribution is important or even negligible. In terms of the computational effort, the contribution from all tetrahedra and bands to the Green function (for each energy) must be calculated.

For the method described here the spectral function at a given energy depends only on the tetrahedra that the constant energy surface intersects, hence the number of tetrahedra that must be considered depends on the grid used to sample $\mathcal{F}$. This means that the spectral function in an energy range that has very little influence on the structure of the Green function at a certain energy (the contribution of high energy states to the Green function below the Fermi energy, for instance) need only be crudely sampled. Once the spectral function is calculated the convolution integral can be carried out to obtain the Green function (at any energy E) with

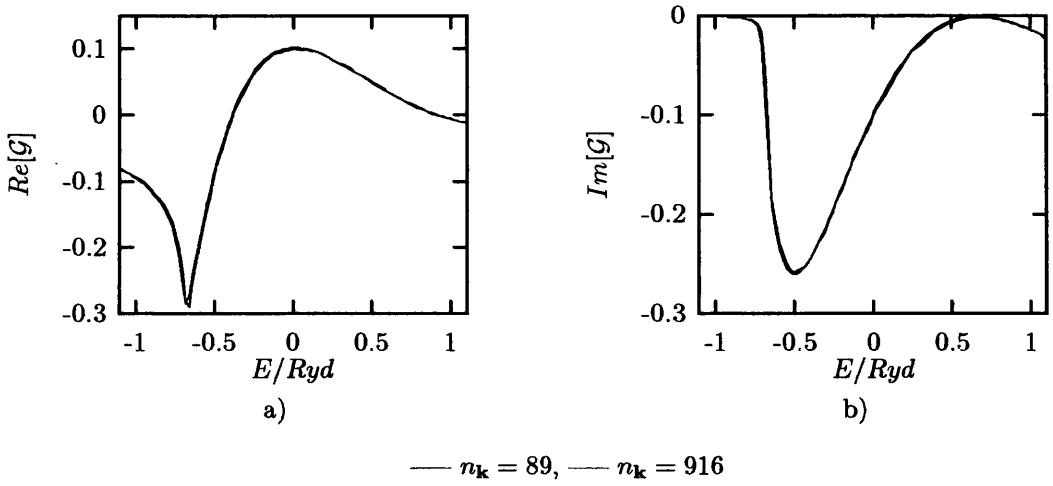

Figure 3.9: Free electron $\mathcal{G}_{(00,00)}$ calculated using the tetrahedron method.

very little computational effort.

The final application of this method (as applied in chapter 5) uses 240 **k** points in the irreducible wedge, the Green function evaluated at 16 energies (this is the number of energies that $\mathcal{G}$ is required for in chapter 5) for both Aluminium and Silicon, and a grid spacing that gives sufficient convergence. For this case the Lambin and Vigneron method required interpolation to be carried out over $\sim 5\times$ more tetrahedra than the LATM + convolution method for Aluminium, and $\sim 10\times$ more for Silicon. This ratio between the number of tetrahedra that must be considered for the two methods scales linearly with the number of energies $\mathcal{G}$ is required for.

3.5.3 Convergence for a Free Electron Green Function

Finally, to provide some further justification for the use of the above procedure over the considerably simpler zero order method, the jellium Green function is examined. Figure 3.9 shows the $(L, L') = (00, 00)$ coefficient of the jellium Green function for a FCC lattice with $a_0 = 4.05\mathring{A}$ and $\varepsilon = 0.1$ eV. All other parameters are the same as for figure 3.4. The IW contains 89 **k** points, and a fully converged result is also shown ($n_{\mathbf{k}} = 916$). In comparison to figure 3.4 the errors are far smaller for 3/4 the number of **k** points in the IW.

Figure 3.10 shows the rms error in the free electron Green function calculated with the zero order method and the LATM + convolution method for the same

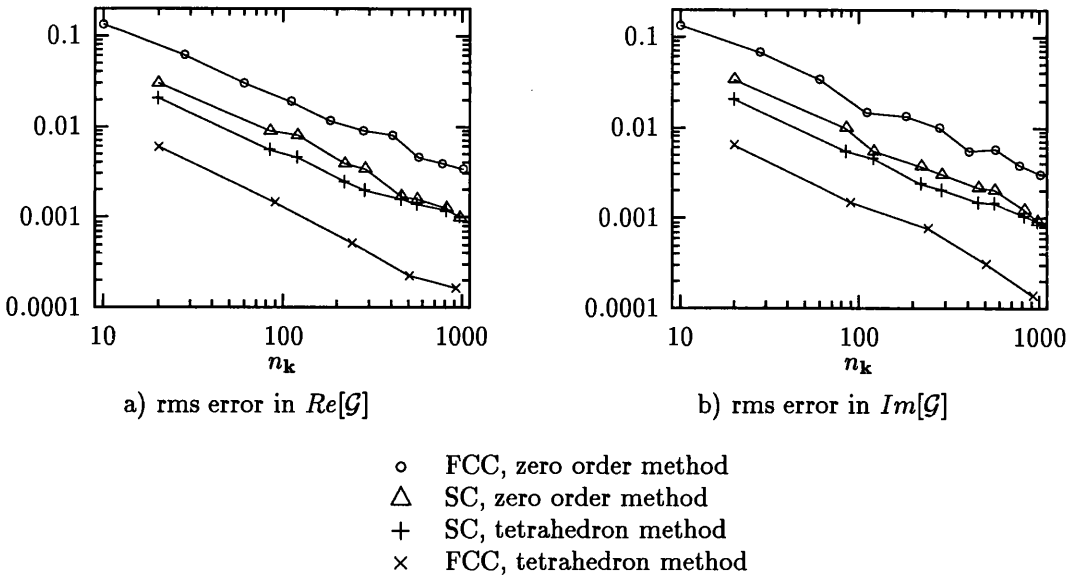

Figure 3.10: Error in free electron $\mathcal{G}_{(00,00)}$ as a function of $n_{\mathbf{k}}$

parameters as figure 3.9. The variation of the error in the $(00,00)$ matrix element with $n_{\mathbf{k}}$ is shown for both simple cubic and FCC unit cells, with $\varepsilon = 0.1$ eV. The error in the real part and the imaginary part within the range from the bottom of the lowest band (ie from V_0) to 1.5 Ryd is considered, a range that encompasses the energy range of occupied bands for metallic charge densities. The bands are ordered by energy, so the effects of band crossing are present, and the convolution integral is carried out with linear interpolation.

From this data it is clear that the LATM with a FCC unit cell gives the best convergence behaviour, as expected from the discussion of band crossing above. For the zero-order method the best convergence is obtained for the simple cubic lattice. This is due to the simple cubic unit cell being larger than the FCC unit cell in real space, hence the Brillouin zone smaller in reciprocal space. As a consequence of this the density of $\mathbf{k}$ points in the Brillouin zone is greater for the simple cubic case.

In all cases the error is approximately $\propto n_{\mathbf{k}}^{-\frac{2}{3}}$, and the LATM method for a FCC cell gives an error an order of magnitude smaller than the zero order method for a simple cubic cell, hence to achieve the same accuracy with the zero-order method requires $\sim 30\times$ as many $\mathbf{k}$ points as the LATM + convolution method. Again it should be noted that the dominant cause of the error for the LATM method is expected to be band crossing, and this should cause smaller errors for a real system.

3.6 Conclusions

Within this chapter the evaluation of a Green function for lattice of atoms is described, where the Bloch states of the lattice are available for a finite number of bands, for a finite sampling of **k** points within the Brillouin zone and are expanded in a plane wave basis set. This is achieved via the spectral representation (equation (3.16)), an expansion of the Green function in terms of the Bloch states of the lattice. In order to evaluate the spectral density an integration over the Brillouin zone must be carried out, for a function with a pole, and the position of the pole depends on the energy value at which the Green function is required. As a consequence of this the evaluation of this Brillouin zone integral requires some care. Lattice symmetry is also applied to reduce the volume of the Brillouin zone over which the integral is carried out. This reduces the volume by a factor of $\frac{1}{48}$ for both a simple cubic and FCC lattice, as considered here.

Two schemes are explicitly compared for a free electron Green function in a reduced zone scheme. The simplest method is a zero-order method. This evaluates the sum of the integrand over all the sample **k** points, weighted by the volume of reciprocal space associated with each point. This was found to be extremely inefficient, not as a consequence of the low order of the method, but due to the fact that it takes no account of the continuous nature of the band structure. The approximate Green function resulting from this method has the same analytic form as that for a set of discrete states, with no branch cut on the real E axis, only poles.

To circumvent this misrepresentation of the physics of the problem, a linear interpolation of the band structure in **k** space is carried out, from an appropriate set of sample points. From this interpolation of the band structure the *imaginary* part of the Green function on the real axis is calculated. From the analytic properties of the Green function, the function can be obtained for any complex energy from this imaginary part. This involves a numerical evaluation of a Hilbert transform (section 3.5.1), a convolution integral. To evaluate this convolution integral the imaginary part of the Green function is sampled on a grid of energy points.

Lambin and Vigneron (1984) have applied the same linear interpolation in **k** space, but with the spectral representation evaluated directly from this linear interpolation. The method applied here (LATM + convolution integral) allows more flexibility in the accuracy to which the Green function is evaluated. This can be more efficient as some parts of the spectrum of states of the Hamiltonian make a very

small contribution to the Green function in a given energy range, and do not require an accurate representation. It should also be remembered that the linear interpolation is an approximation in itself, so it is questionable whether it is worth accurately representing a function that is already approximate.

For Aluminium the Lambin and Vigneron method requires the evaluation of the linear interpolation parameters for $\sim 5\times$ as many tetrahedra as the LATM + convolution integral method to achieve an accuracy sufficient for the applications considered here. For Silicon the factor is ~ 10.

Higher order methods of interpolation are discussed, but these do not prevent band crossing, the effect that makes the biggest contribution to the error in the Brillouin zone integration. Both the Lambin and Vigneron method and the LATM + convolution method suffer from the errors introduced by band crossing.

These errors could be avoided by using *extrapolation* methods that preserve the band identities within the extrapolation region, as implemented by Müller and Wilkins (1984). These methods appear to improve convergence considerably, however they do require the gradient of the band structure (and possibly the Bloch states) in $\mathbf{k}$ space, which complicates the application of the method. Extrapolation methods are not applied in the work presented here. The LATM + convolution method described in this chapter allows the efficient calculation of the spectral representation, using a manageable number of $\mathbf{k}$ points (a factor of ~ 30 less than the zero order method).

So far the method presented approximates the spectral density using only a finite number of bands, and the spectral representation is only valid for a complete set of eigenfunctions included in the sum. The corrections to the finite sum are the topic of the next chapter, and the convergence of the method for the Green function and the embedding potentials derived from it are also presented.

Chapter 4

The Green Function and Embedding Potential

4.1 Introduction

In the previous chapter a method for the evaluation of the Green function resulting from the application of the spectral representation to the eigenstates of a total energy pseudopotential calculation is described. The method given takes into account the continuum nature of the band states, but for the spectral representation to be valid the set of states used in the sum must be *complete.* With only n bands included in the sum this is not the case, and in what follows this approximation is referred to as the *incomplete spectral representation.* It is not immediately apparent that this will have a significant effect, and it could be hoped that the 'missing' high energy states are so far above the energies of interest (at or below the Fermi energy) that any error introduced by their absence will be negligible. This is found to be only partly true, and a further correction is required to take into account the errors introduced by this lack of completeness. This correction not only speeds convergence of the approximation with the number of bands included, it also ensures that the approximation has the correct analytic form.

At this point it should be noted that although it is well established that a Green matrix can be defined within a limited basis set, and Green function methods used within this limited basis set (Williams et al, 1982), including the spectral representation, this requires the entire problem to be formulated in terms of the

limited basis set. The construction of the embedding potential and the embedding method rely on the properties of the *Green function in real space*, so cannot be formulated in this way.

Analogues of the real space embedding method are available, defined more generally in Hilbert space (see Fisher, 1988). A formulation in terms of a limited basis set using these methods might be more successful, but these methods receive no more attention in this thesis.

In section 4.2 this 'correction' term for the incompleteness of the set of functions present in the spectral representation is derived. Firstly the error introduced by not including the high energy bands is derived for a free electron gas to examine the characteristics of this error. Following this an error term for the incomplete spectral representation described in the previous chapter is presented. In section 4.3 the convergence properties of the Green function with the various parameters of the calculation are shown, for bulk Aluminium and Silicon. Section 4.4 begins with the calculation of the embedding potential matrices from the Green function (and its derivative) and the convergence of the embedding potential itself is examined.

Within this chapter convergence of the Green function and embedding potential matrices is explicitly examined only for particular matrix elements. This is entirely for reasons of space, and unless otherwise stated the conclusions and behaviour are the same for a general matrix element.

4.2 Completing the Incomplete Set of States

4.2.1 Error Term for a Free Electron Gas

The approximation to the Green function matrix obtained so far can be converged with respect to the number of $\mathbf{k}$ points and the energy sampling of the spectral function matrix. The fact that the spectral representation of a Green function is only valid if the sum is over a *complete* set of wavefunctions requires an infinite number of bands, which are not available. As a consequence of this 'incomplete' spectral representation the cusp at $\mathbf{r} = \mathbf{r}'$ is not present and the calculated function oscillates around the true function near this point. To illustrate this figure 4.1 gives the normal derivative of the $(L, L') = (10, 10)$ element of the free electron Green

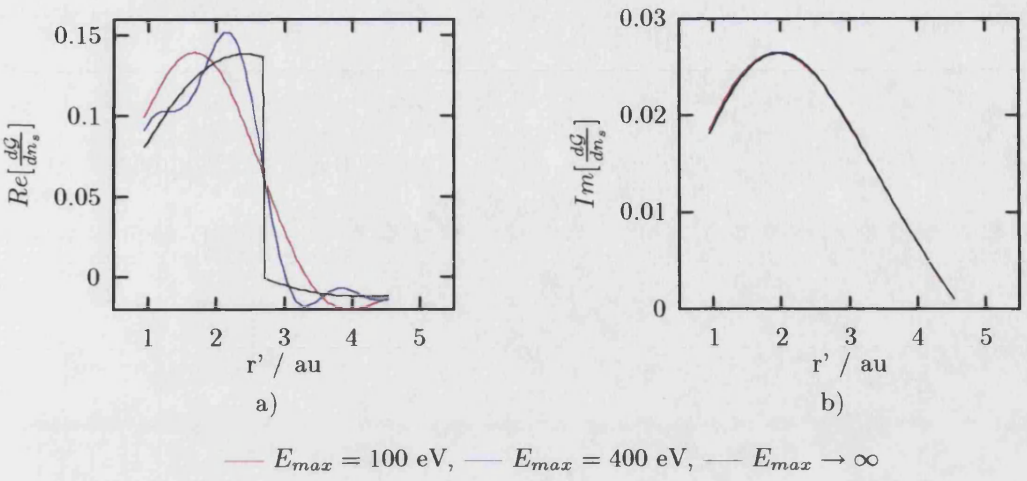

Figure 4.1: Free electron $\frac{\partial}{\partial n_2}\mathcal{G}_{(10,10)}$ as a function of r'.

function (with respect to r') for r at radius $r_s = 2.706$ au and for variation in r' about this radius. This Green function has been calculated for a simple cubic lattice ($a_0 = 4.05$ au), $V_0 = -9.5$ eV and at $E + i\varepsilon = (0 + 0.5i)$ eV. This effect is analogous to Gibb's phenomena seen in truncated Fourier integrals.

In order to assess the error introduced by this lack of completeness the case of a free electron spectral representation truncated at a finite energy is examined. An extended zone scheme is employed, and an expansion in spherical harmonics.

The contribution to the Green function of the terms of energy greater than some maximum value, $E_{cut} = k_0^2$, is calculated (this energy cutoff is analogous to the E_{max} cutoff in equation (3.13)). Since the high energy Bloch states should be essentially free in character, it seems reasonable that this should give an indication of the error introduced by the incompleteness of states in the spectral representation as applied so far. The free electron Green function is spherically symmetric, and with the sum over states outside a spherical boundary in **k** space this is also true of the error. As a consequence of this, both matrices are diagonal and independent of the m index, hence only one index is shown in what follows and the m index is suppressed.

The $\mathcal{F}$ matrix for free space is given by the imaginary part of the Green function for free space, or

$$\mathcal{F}_{LL'}(E') = k j_l^2(kr_s)\delta_{LL'} \tag{4.1}$$

where $E' = k^2$ and is real (Morse and Feshbach, 1953). From this the error, $\xi_l(E, E_{cut})$, introduced in the Green function from not including states with energy

greater that E_{cut} can be calculated. This leads to the defining equation

$$\xi_l(E+i\varepsilon, E_{cut}) = \frac{1}{\pi}\int_{E_{cut}}^{\infty} \frac{kj_l^2(kr_s)}{E+i\varepsilon-E'}dE'. \tag{4.2}$$

Using the relation $E' = k^2$ this leads immediately to

$$\xi_l(E+i\varepsilon, E_{cut}) = \frac{2}{\pi}\int_{k_0}^{\infty} k^2 \frac{j_l^2(kr_s)}{E+i\varepsilon-k^2}dk \tag{4.3}$$

where $k_0 = E_{cut}^{\frac{1}{2}}$. For $E_{cut} > |E+i\varepsilon|$ the integrand may be expanded as a Taylor series, to give the error expanded as a series

$$\xi_l(E+i\varepsilon, E_{cut}) = \sum_n a_l^n (E+i\varepsilon)^n \tag{4.4}$$

where

$$a_l^n(E_{cut}) = -\frac{2}{\pi} r_s^{2n-1} \int_{k_0 r_s}^{\infty} \frac{j_l^2(x)}{x^{2n}}dx. \tag{4.5}$$

These integrals can be carried out analytically by repeated integration by parts, to give solutions of the form

$$a_l^n = -\frac{1}{\pi}\frac{1}{2n+1}\frac{1}{r_s^2}\frac{1}{k_0^{2n+1}} + O\left(\frac{1}{k_0^{2n+2}}\right) \tag{4.6}$$

where the second term contains trigonometric functions.

For the normal derivative a similar expression can be derived. Denoting the coefficients of the series expansion by b_l^n, these are given by

$$b_l^n = \frac{1}{\pi}\frac{1}{2n+1}\frac{1}{r_s^3}\left[1 - \frac{2n+1}{2}(-1)^l \cos 2k_0 r_s\right]\frac{1}{k_0^{2n+1}} +$$

$$O\left(\frac{1}{k_0^{2n+2}}\right) + \delta_{n,0}\begin{cases} 1/2r_s^2 & r > r' \\ -1/2r_s^2 & r < r' \end{cases} \tag{4.7}$$

where the last term on the RHS is a step function. This step function is the source of the cusp necessary for the correct analytic form of a Green function.

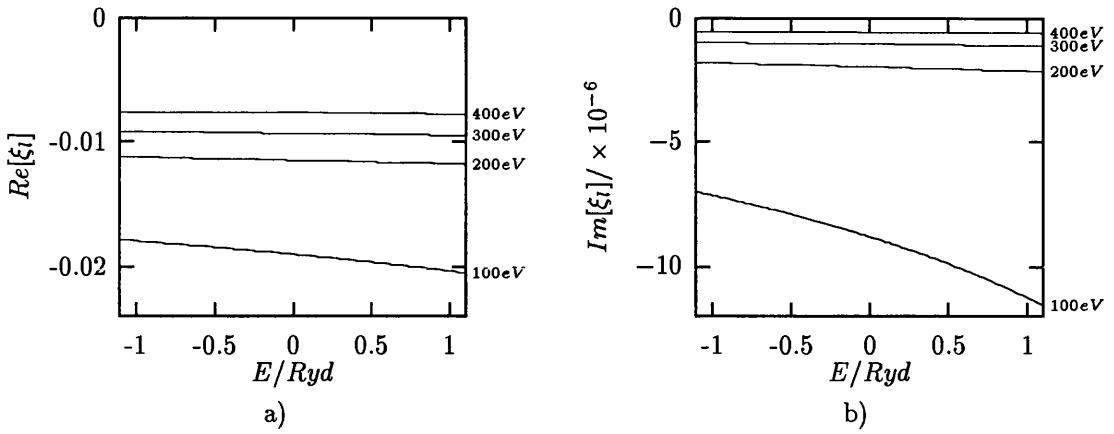

Figure 4.2: Contribution to free electron $\mathcal{G}_{(00,00)}$ from states of energy $> E_{cut}$, ξ_0, as a function of E.

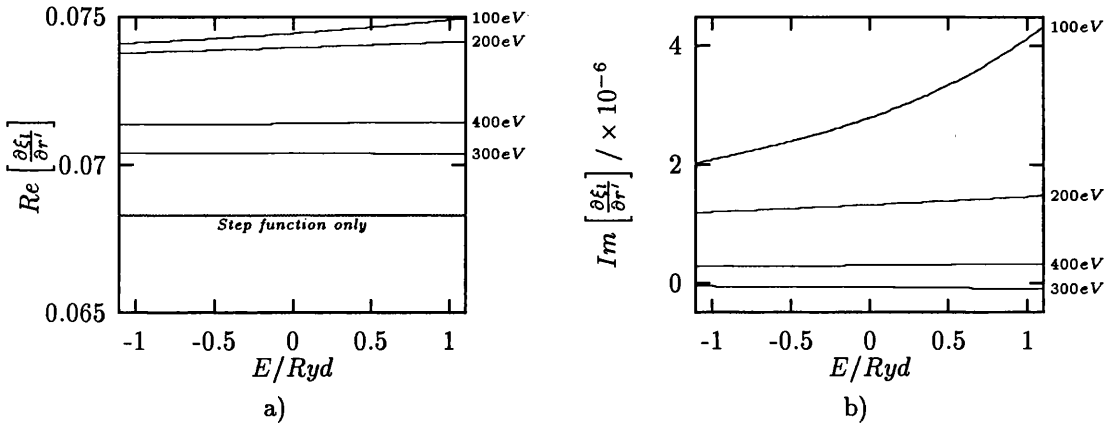

Figure 4.3: Contribution to free electron $\frac{\partial \mathcal{G}_{(00,00)}}{\partial n_2}$ from states of energy $> E_{cut}$, $\frac{\partial \xi_0}{\partial n_2}$, as a function of E. 'Step function only' denotes the contribution from the step function in equation (4.7).

ξ_l as a function of Green function energy, E

Figure 4.2 shows the error term, ξ_l, for the Green function as a function of $E + i\varepsilon$ (with $\varepsilon = 0.1$ eV and E_{cut} taking a range of values). ξ_l is calculated by evaluating equation (4.5) analytically for $n \leq 6$ and using the series expansion (this is enough to converge the final result), and $r_s = 4.05\sqrt{2}/4$ au. It is apparent from this figure that the error introduced from using an incomplete spectral representation shows only a weak dependence on $E + i\varepsilon$ provided the cutoff energy E_{cut} is large enough. However, although the error is approximately constant with $E + i\varepsilon$, the real part is of significant magnitude.

The error term of the normal derivative is shown in figure 4.3, and this shows the same characteristics. The main effect of these high energy states on the Green

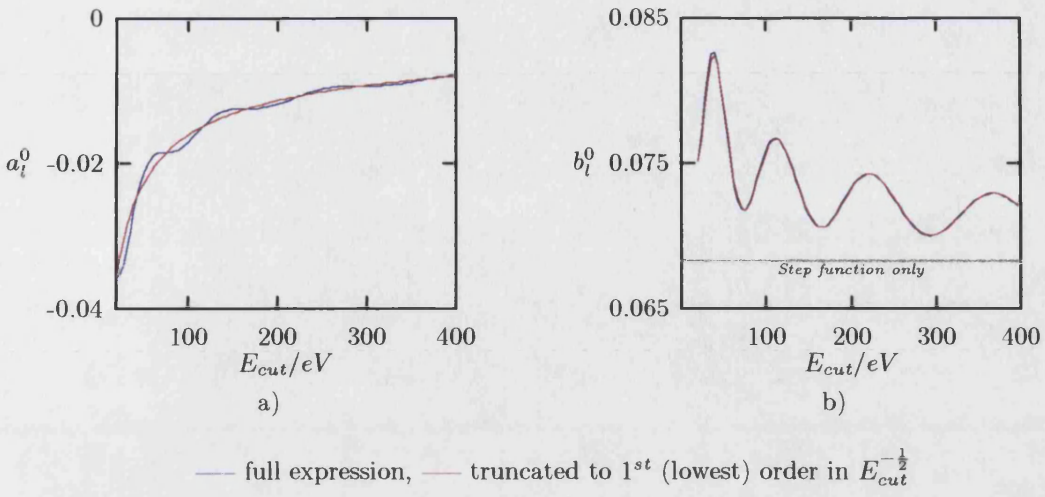

Figure 4.4: Error in $\mathcal{G}_{(00,00)}$ as a function of E_{max}. Both a full evaluation of equations (4.6) and (4.7) and the expressions approximated by the lowest order term are shown. 'Step function only' denotes the contribution from the step function in equation (4.7).

function at low energies (near the Fermi energy) is an error constant in $E + i\varepsilon$, or at worst a low order polynomial function of $E + i\varepsilon$.

ξ_l as a function of the cutoff energy, E_{cut}

Since the error is approximately independent of the energy at which the Green function is required, the dependence of the zero order part of the error on the energy cutoff E_{cut} is examined. Figure 4.4a shows the $n = 0$ term of the error in the Green function, together with the first term in the expansion of a_l^0 given in (4.6), and figure 4.4b the analogous case for the error in the normal derivative of $\mathcal{G}$. In both cases $l = 0$.

From these figures it can be seen that the convergence with respect to the energy cutoff is slow, approximately $\propto E_{cut}^{-\frac{1}{2}}$ (to lowest order) for the Green function. For the normal derivative of the Green function at the embedding surface the error decays, approximately $\propto E_{cut}^{-\frac{1}{2}}$ but with the addition of an oscillatory term whose magnitude decays as $E_{cut}^{-\frac{1}{2}}$ (again to lowest order).

To summarise, both the Green function and its derivative show an error that varies with E_{cut} in a significantly more complex manner than a simple power law decay with E_{cut}, and the error in the normal derivative does not converge to zero with

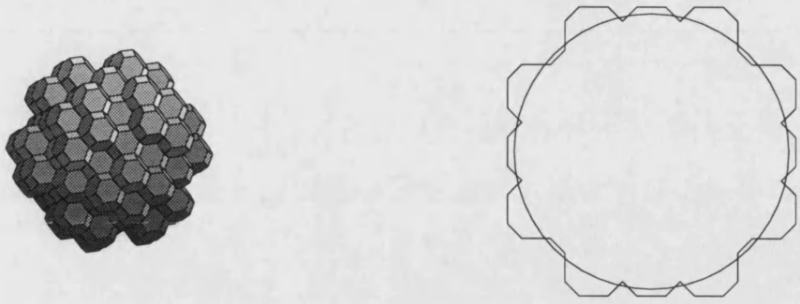

a) Perspective view b) Slice through xy plane

Figure 4.5: Region of reciprocal space occupied by basis set. Lattice is FCC and 113 bands are present - the figures are constructed from 113 FCC Brillouin zones.

increasing E_{cut}. For a finite E_{cut} the error function will always include the step function in equation (4.7).

4.2.2 Error Correction Term for the Incomplete Spectral Representation

A reasonable approximation to the high energy bands 'missing' from the spectral representation as applied in chapter 3 is to substitute free electron bands in their place. This can be justified from the high energy behaviour of the Bloch states - as the eigenenergy increases they become more free electron like. This is the method proposed by James and Woodley (1996) (see also Woodley, 1997), and applied to the $\mathbf{k}$ dependent Green function for some model systems.

For the results of the matrix diagonalisation preformed using CASTEP (see chapter 3) the set of bands available are represented in the plane wave basis set described by $|\mathbf{g}|^2 < E_{max}$, where the $\mathbf{g}$ are the reciprocal lattice vectors and E_{max} is a parameter that describes the size of the basis set. This suggests that the free electron states required to 'top up' the incomplete spectral representation are those described in the reduced zone scheme by $|\mathbf{g}|^2 > E_{max}$ and $\mathbf{k}$ in the first Brillouin zone.

Figure 4.5a shows the volume of $\mathbf{k}$ space occupied by the basis states for a band structure calculation carried out for Aluminium (the same as that in chapter 3) in the extended zone scheme and $E_{max} = 200$ eV. This volume would take the place of the sphere used to calculate the error terms above if a similar expansion to the spherical boundary case was derived, but this would involve a difficult surface

integral. However a sphere may be a good enough approximation to the surface in figure 4.5a for equation (4.3) to give a good approximation to the incompleteness errors - in figure 4.5b a cross section of figure 4.5a is shown (in the plane of the page) together with a cross section of a spherical boundary that encompasses the same volume as the actual boundary.

'Topping Up' within the Reduced Zone Scheme

In order to correct the Green function derived in the previous chapter, the technique employed is to calculate a free electron incomplete spectral representation with the same basis as the pseudopotential states. The difference between the free space and pseudopotential incomplete spectral representations (calculated with a limited basis set) is then taken. The analytic free electron Green function is then added to complete the spectral representation. This gives the approximation

$$\mathcal{G} \approx \mathcal{G}^{pseudo}_{E_{max}} - \mathcal{G}^{free}_{E_{max}} + \mathcal{G}^{free}_{\infty} \tag{4.8}$$

where the first term on the RHS is the incomplete spectral representation of the pseudo-states, the second is the incomplete spectral representation of free electron states and the final term the complete spectral representation for free electron states (the analytic free electron Green function).

In terms of the spectral function, $\mathcal{F}$, and the convolution integral used to transform this into the spectral representation this becomes

$$\mathcal{G}_{LL'} = \int \frac{\mathcal{F}^{pseudo}_{LL'} - \mathcal{F}^{free}_{LL'}}{E - E'} dE' + \mathcal{G}^{\infty}_{LL'} \tag{4.9}$$

where $\mathcal{G}$ is the Green function with the correct analytic form, E is complex and E' is real. $\mathcal{F}^{pseudo}$ and $\mathcal{F}^{free}$ are the spectral functions from the pseudo states and the free space states respectively, calculated from the limited basis functions, and are functions of E'. The last term, $\mathcal{G}^{\infty}$, is the analytic free space Green function given by (Abramowitz and Stegun, 1965; Morse and Feshbach, 1953)

$$\mathcal{G}^{\infty}_{LL'} = -ikj_l(kr_s)h_l(kr_s)\delta_{ll'} \tag{4.10}$$

where j_l is the spherical Bessel function of the first kind, h_l is the spherical Hankel function of the first kind and $E = k^2 + V_0$ where V_0 is the average potential within the unit cell (the specific value of V_0 not critical - see figures 4.2 & 4.3).

4.3 Convergence Properties

So far the method of approximating the Green function from the electronic states represented in the plane wave basis set has been described. The basic nature of the method has been examined by using free electron jellium states. These states are useful since an analytic form for the Green function is available for comparison with the approximations, and these comparisons have been made in the previous sections.

In this section the Green functions for bulk FCC Aluminium and Silicon are presented and the convergence of these with parameters of the calculation is investigated. These are the materials for which the embedding potentials are required.

The convergence behaviour of these Green functions depends on the following parameters of the approximations used:

- The number of plane waves in the basis, $n_{\mathbf{g}}$, or equivalently E_{max}.
- The number of $\mathbf{k}$ points in the irreducible wedge of the FCC Brillouin zone, $n_{\mathbf{k}}$.
- The spacing of energy points (ΔE) used to sample the spectral function, $\mathcal{F}$, in order to carry out the convolution integral.

4.3.1 The Total Energy Pseudopotential Calculation

As described in chapter 3, CASTEP is used to obtain the self-consistent potential for Aluminium and Silicon. Parameters of this calculation are chosen to ensure convergence of the total energy and self consistent potential. No effort is made here to demonstrate that the self consistent calculations are in fact converged, but for the materials investigated here the convergence behaviour is well understood and the parameters of the calculation are more than adequate to ensure convergence.

The self consistent potential obtained from this calculation is then used to generate the Hamiltonian within the chosen plane wave basis set, at each of the required $\mathbf{k}$ points. Plane waves that satisfy $|\mathbf{g}|^2 < E_{max}$ provided the basis set, and $\mathbf{k}$-points in the required mesh (see chapter 3) are calculated for Aluminium and Silicon. In what follows the 'standard' calculation is carried out for $E_{max} = 200$ eV, $n_{\mathbf{k}} = 240$

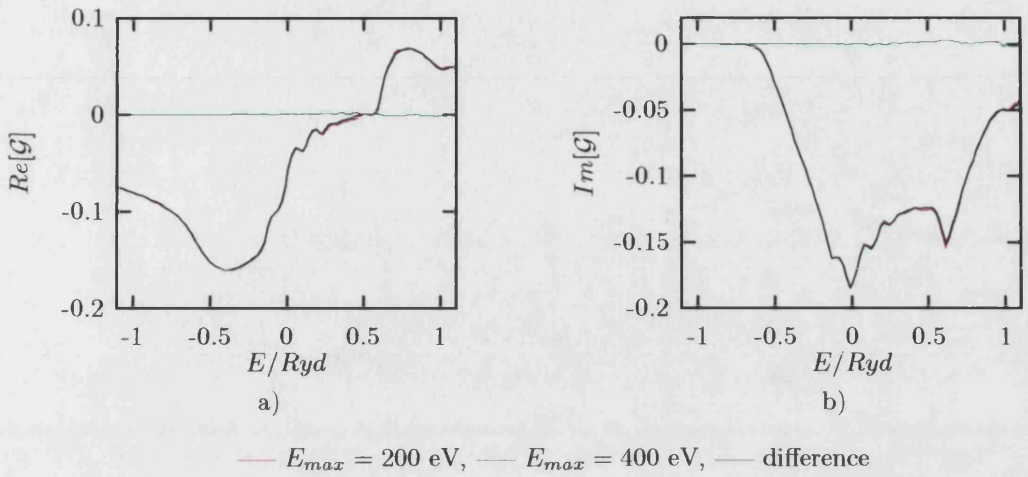

Figure 4.6: Convergence of Aluminium $\mathcal{G}_{(10,10)}$ with E_{max}.

and the spacing of points for the spectral function, $\Delta E = 0.1$ eV. These parameters are used unless other values are specifically given. For all results in this chapter the imaginary part of the energy at which the Green function is evaluated takes the value 0.1 eV, and in all the figures E refers to the *real* part of the Green function energy. All of the Green functions presented from this point on are 'topped up'.

4.3.2 Energy Cutoff for Basis Set, E_{max}

First the convergence of the Green function matrix with the number of plane waves employed in the diagonalisation of the Hamiltonian is investigated. For Aluminium four energy cutoffs are chosen, given in Table 4.1 together with the number of bands each of these correspond to.

Figure 4.6 shows the $(lm, l'm') = (10, 10)$ element of the Green matrix for Al, and for E_{max} taking values of 200 eV and 400 eV, or $n_{\mathbf{g}} = 113$ and 307 respectively. The difference between the two is also shown. It is immediately apparent that

E_{max}/eV	n_g - Al	n_g -Si
100	27	89
200	113	259
300	181	459
400	307	725

Table 4.1: Number of plane waves/bands for each energy cutoff

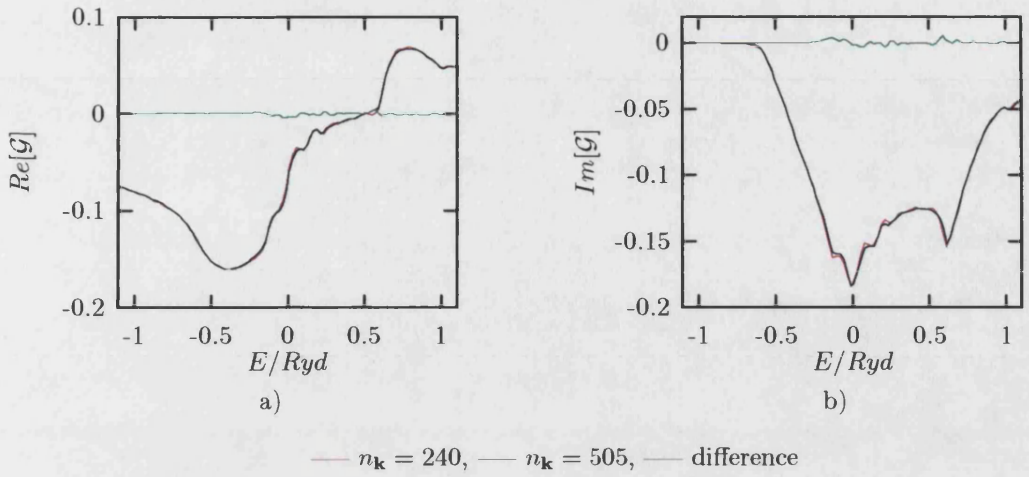

Figure 4.7: Convergence of Aluminium $\mathcal{G}_{(10,10)}$ with $n_{\mathbf{k}}$.

the approximation is well converged by $E_{max} = 200$ eV - the maximum difference between $E_{max} = 200$ eV and $E_{max} = 400$ eV is ≈ 0.002 for both the real and imaginary parts. If the topping up procedure is not employed the convergence is considerably worse and an approximately constant (with energy) error appears that converges slowly with energy cutoff, as expected from the discussion in section 4.2.

4.3.3 Number of k Points, $n_{\mathbf{k}}$

Table 4.2 gives the size of the **k** point sets that are investigated - $n_{\mathbf{k}}$ is the number of points within the FCC irreducible wedge.

Figure 4.7 shows the $(10, 10)$ element of the Green function for Al for $n_{\mathbf{k}} = 240$ and 505, and the difference. A similar degree of convergence is found to the previous subsection for 240 **k** points - the maximum difference between the results for 240 and 505 **k**-points is ≈ 0.004 for both real and imaginary parts.

q	$n_{\mathbf{k}}$
4	20
8	89
12	240
16	505

Table 4.2: Size of **k** point sets in Brillouin zone integration

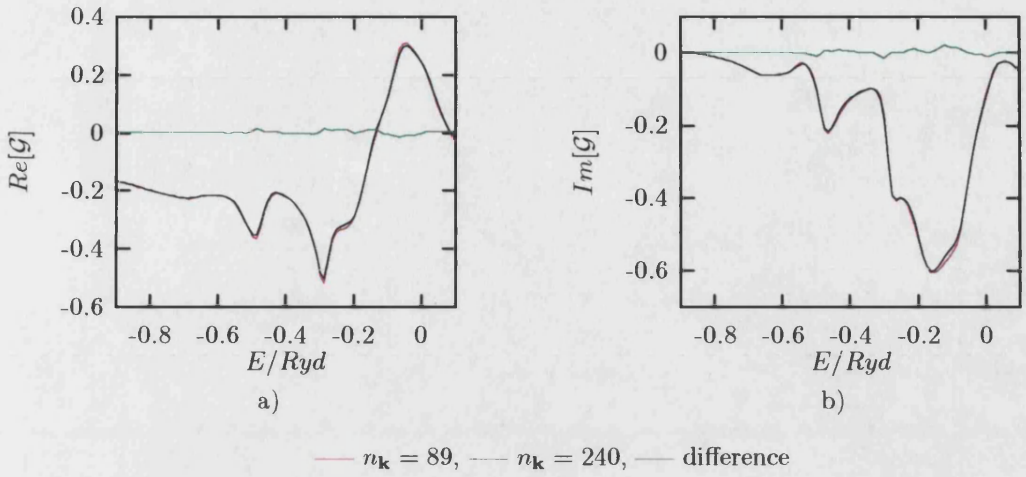

Figure 4.8: Convergence of Silicon $\mathcal{G}_{(10,10)}$ with $n_{\mathbf{k}}$.

In figure 4.8 the same results for Si are given, but results for $n_{\mathbf{k}} = 89$ and 240 are compared. As expected the maximum difference is larger, at ≈ 0.015 (for Aluminium the error is similar).

4.3.4 $\mathcal{G}$ from $\mathcal{F}$ - the Convolution Integral

Convergence of the convolution integral given by equation (3.63) is investigated in this section. In section 3.5 the method of approximating this integral was presented, and the error introduced by sampling $\mathcal{F}$ on a grid must be assessed.

Spectral Function Sampling

Convergence of the integral with the spacing of the interpolating points, ΔE, is the next consideration. Figures 4.9 and 4.10 show $(10, 10)$ matrix elements for Al and Si respectively, with $\Delta E = 0.1$ and 0.3 eV in each figure (linear interpolation is used for both). The difference between the matrix elements for the two ΔE values is also plotted. For both Al and Si there is a small difference between the two sample spacings (≈ 0.001 maximum for Al, and ≈ 0.025 for Si). The errors for Si are around the same as for Al except at the van Hove singularities, where the large errors are introduced, as can be seen from figure 4.10. Aluminium converges far quicker than Silicon, as would be expected since the band structure of Silicon exhibits more fine structure.

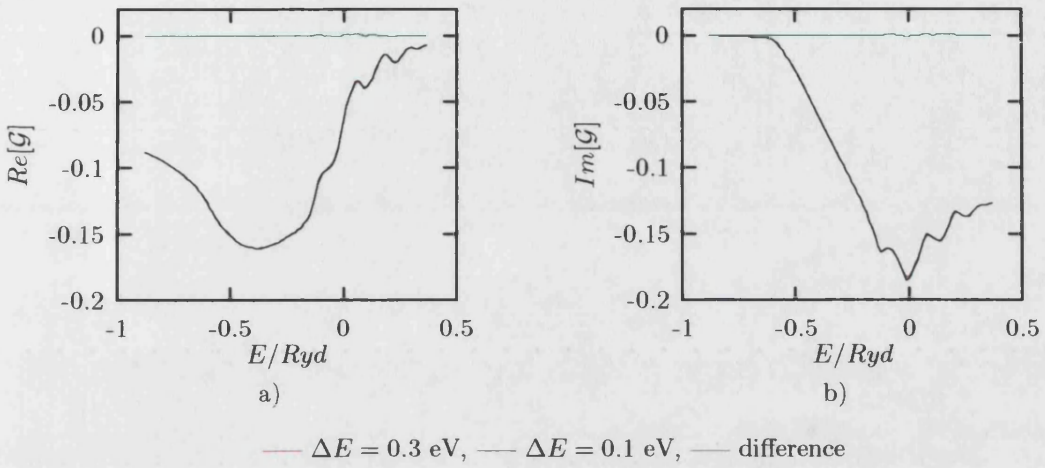

Figure 4.9: Convergence of Aluminium $\mathcal{G}_{(10,10)}$ with spectral function sampling interval, ΔE (linear interpolation).

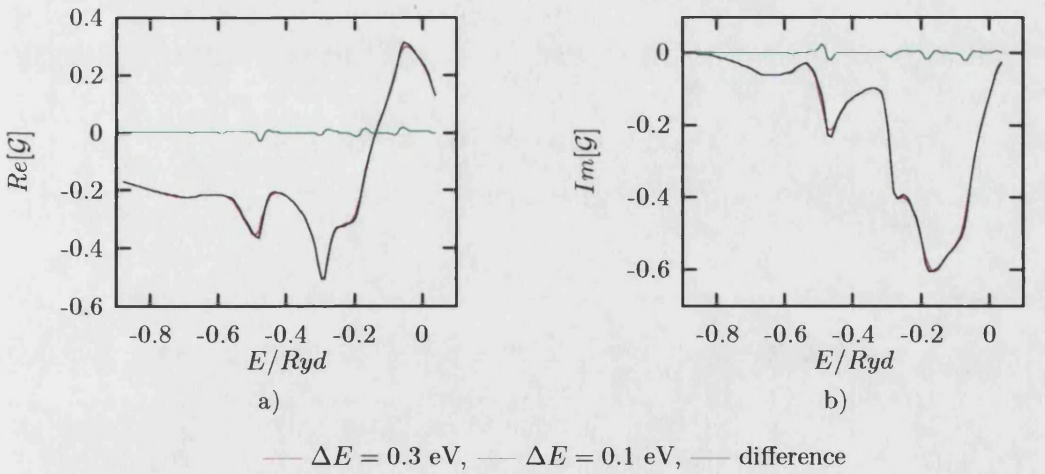

Figure 4.10: Convergence of Silicon $\mathcal{G}_{(10,10)}$ with spectral function sampling interval, ΔE (linear interpolation).

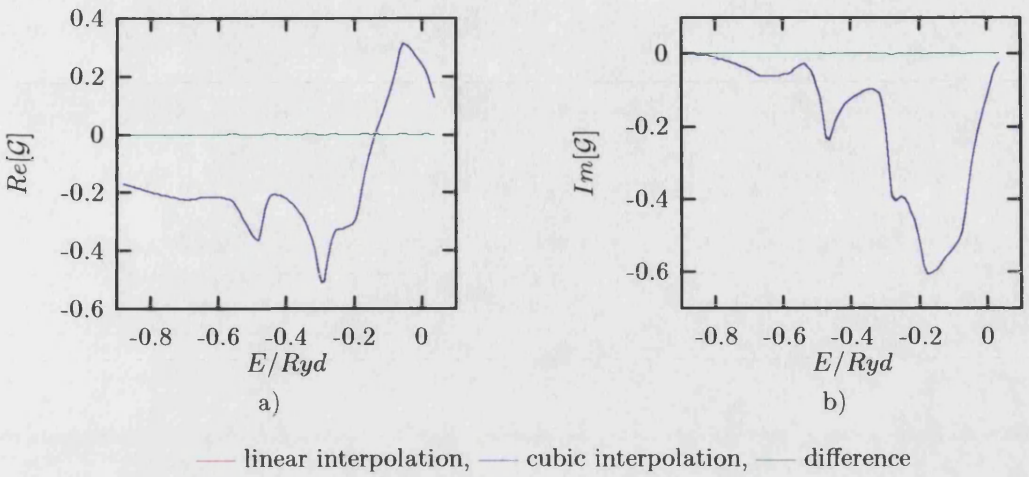

Figure 4.11: Silicon $\mathcal{G}_{(10,10)}$ for linear and cubic polynomial interpolation of $\mathcal{F}$, $\Delta E = 0.1$ eV.

In figure 4.11 the linear and cubic interpolation of the spectral function are compared, for Si with $\Delta E = 0.1$ eV. For this mesh of points the difference between the two results is negligible (≈ 0.002). For increasing ΔE the deviation from the converged result (taken to be 0.1 eV here) is not significantly lower for the cubic interpolation. For Aluminium the error for cubic interpolation is slightly lower than for linear interpolation, and for Silicon the error for cubic interpolation is *higher* than the linear case. This is probably due to the fact that the spectral function itself is not well approximated by a polynomial, so a higher order integration method can give worse results than a lower order method (Press et al, 1994). Not only are cusps present (due to van Hove singularities), but the function itself may well be best characterised by fractional powers (see section 3.4.4).

Artifact in the Incompleteness Correction

A problem with the spectral function and 'topping up' method employed here that requires attention is an unwelcome feature in the $(00,00)$ part of the Aluminium Green function at the bottom of the first band. Figure 4.12 shows the $(00,00)$ element of the Green function for the incompleteness correction calculated numerically (section 4.2.2), and analytically (section 4.2.1). Extensive tests have shown that the analytic form of the error correction is only a good approximation for the $(00,00)$ matrix element of the $\mathcal{G}$ function, and is not accurate for other elements or the normal derivative. It should be noted that it is only for this matrix element that this artifact of the approximation appears.

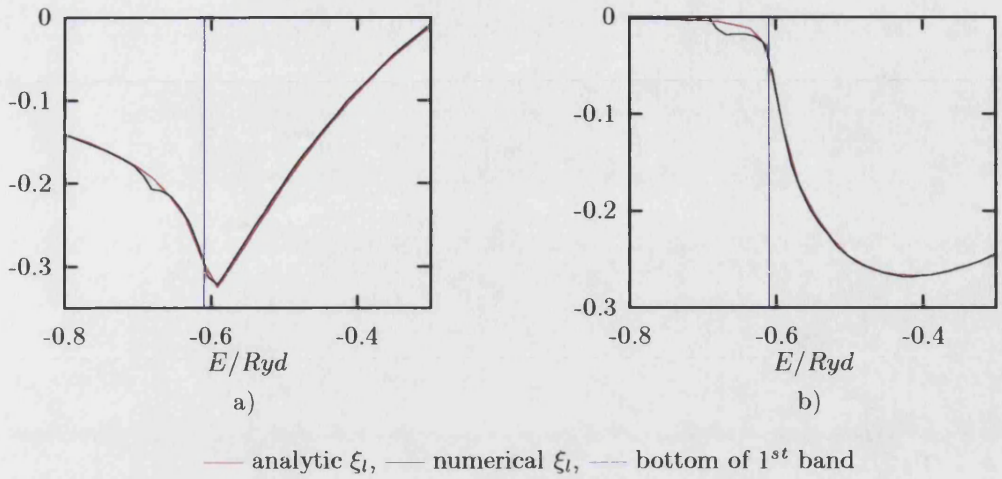

Figure 4.12: Aluminium $\mathcal{G}_{(00,00)}$ for analytic and numerical evaluation of ξ_l, the 'topping up' term.

Since (as figure 4.12 illustrates) the anomalous feature is not present for the analytic error correction term, it can be ascribed to the approximation employed to evaluate the error correction term numerically. The position of the feature is ≈ -0.7 Ryd, which is the zero energy for the free electron states used to 'top-up' the spectral representation. This leads to the conclusion that this feature is a consequence of inadequacies in the numerical methods that only appear at the bottom of the free space bands.

The source of this feature is the breakdown of the polynomial interpolation of the spectral function of the free electrons at the bottom of the first band, due to the van Hove singularity at the bottom of the first band (this is the only one present for free electrons). This in itself would only cause a small error but for the fact that we are taking the difference between the incomplete spectral representation of free space and the complete (analytic) Green function for free space to obtain the error correction term, $\xi_l(E, E_{max})$. The error term is small in comparison with the Green function, so a small error in the incomplete spectral representation of free space can result in large errors in the error term, $\xi_l(E, E_{max})$.

Fortunately this feature is below the lowest energy band for Aluminium (see figure 4.12), so can be expected to be irrelevant to the results of the embedding calculation (only the energies where states are occupied are important for the embedding calculations - see chapter 5). If this feature did become a problem then it could be removed by interpolating the free electron spectral function with a more appropriate function within some energy ranges, such as a spherical Bessel function

or a fractional power. Alternatively, analytic 'topping up' could be used for this matrix element.

4.4 Embedding Potential from the Plane Wave Pseudopotential Calculations

In this section the embedding potentials for a spherical region centred around an atomic site in a bulk material are derived. These are obtained from the Green function matrices given above, and the convergence of these potentials is investigated. In Chapter 2 two general expressions for the embedding potential in terms of a general Green function defined on a surface were presented. In this section these are applied to the spherical embedding surface, and the suitability of each of these (and a possible combination) is discussed.

4.4.1 Γ from $\mathcal{G}$

To obtain the embedding potential (Γ) from the Green functions above either equation (2.19) or (2.22) can be applied. The potential itself is non-local, energy dependent and non-zero only on the surface of the embedding sphere ($r = r' = r_s$, where r_s is the embedding sphere radius). The application of the defining equation(s) of the embedding potential requires the inversion of the Green function over the embedding surface, as discussed in chapter 2. This surface inversion (see equation (2.10)) corresponds to the inversion of the matrix representation of the Green function on the surface, provided the basis functions used to construct the matrix are orthonormal over the embedding surface (in this case a sphere of radius r_s).

As discussed before, for a spherical embedding surface an appropriate set of basis functions are the spherical harmonics. Starting with the appropriate matrix defined by

$$G(\mathbf{r}_s, \mathbf{r}'_s; E) = \sum_{LL'} Y_L(\Omega)\mathcal{G}_{LL'}(r_s, r_s; E)Y^*_{L'}(\Omega'), \tag{4.11}$$

the embedding potential matrix, $\Gamma_{LL'}$, defined by

$$\Gamma(\mathbf{r}_s, \mathbf{r}'_s; E) = \sum_{LL'} Y_L(\Omega)\Gamma_{LL'}(E)Y^*_{L'}(\Omega') \tag{4.12}$$

is required. This can be obtained by applying the matrix equivalent of equations

(2.19) and (2.22). The corresponding expressions are

$$\Gamma^{(1)} = -\frac{1}{r_s^2}\mathcal{G}^{-1}\left(\frac{1}{r_s^2}\mathcal{I} - \frac{\partial}{\partial n_2}\mathcal{G}\right) \tag{4.13}$$

and

$$\Gamma^{(2)} = \left(\mathcal{I} + r_s^2\frac{\partial}{\partial n_1}\mathcal{G}\right)^{-1}\frac{\partial^2}{\partial n_1 \partial n_2}\mathcal{G} \tag{4.14}$$

where the superscript denotes the two different expressions. Either of these two equations can be directly applied to the matrix representation of the Green function on the surface, given in section 4.3, to obtain the embedding potential for the substrate system. $\Gamma^{(1)}$ is the form used in this work for the reasons described in section 4.4.2.

4.4.2 Influence of Convergence of G on Γ

Figures 4.13-4.19 show the convergence behaviour of the embedding potential $\Gamma^{(1)}$ with the parameters that effect the convergence of the Green function from which it is calculated. These parameters are $n_{\mathbf{k}}$, $n_{\mathbf{g}}$ (or E_{max}) and ΔE, as discussed in the previous section.

Energy Cutoff

The correction term used to take into account the missing high energy states in the spectral representation approximates these missing states with free electron states. The error still present (that is the difference between the actual Green function and the approximation) will still be entirely due to the higher energy states, above E_{max}, so at the lower energies of interest (below the Fermi energy) the error can be expected to take the form of a constant (or low order polynomial) error.

For the Green functions themselves this is good news, as the error is well behaved (see section 4.2), but for the embedding potential derived from this problems can arise due to the presence of an inversion in the definition of Γ. To illustrate this we shall consider the case of a free electron Green function with a small error term, constant in energy, added to the Green function. This is not meant to be a quantitative analysis of the errors in the calculated Γ, but only a brief demonstration of what form these errors will take.

An error term of ϵ_l gives

$$\mathcal{G}_L(r,r') = -ikj_l(kr_<)h_l(kr_>) + \epsilon_l \tag{4.15}$$

for the approximate (diagonal) free electron Green function matrix elements $\mathcal{G}_L$, where $k = \sqrt{E}$, and $r_>$ and $r_<$ are the larger and smaller of r and r' respectively. The functions j_l and h_l are a spherical Bessel function of the first kind and a Hankel function of the first kind respectively. Placing this approximate Green function in equation (4.13) gives

$$\Gamma^{(1)} = \frac{1}{r_s^2} \frac{ik^2 j_l(kr_s)h_l'(kr_s) - \epsilon_l'}{ikj_l(kr_s)h_l(kr_s) - \epsilon_l} \tag{4.16}$$

where the dash denotes the derivative. If $\epsilon_l = 0$ and $\epsilon_l' = 0$ then this reduces to the free electron embedding potential

$$\Gamma^{(1)} = \frac{k}{r_s^2} \frac{h_l'(kr_s)}{h_l(kr_s)} \tag{4.17}$$

due to cancellation of the Bessel functions. However with an error present the denominator can be zero when the numerator is not, hence a *small* error in the Green function may result in a *large* error in the embedding potential.

It is clear that for this system a small error in $\mathcal{G}$ at the zeroes of j_l results in a pole in $\Gamma^{(1)}$, or that small errors in the Green function can result in large localised errors in the embedding potentials calculated from them. The same argument can be applied to the aspherical Green function calculated for Al and Si. For this case poles will appear when the Green function matrix is singular (see equation (4.13)), or close to singular. Equation (4.14) gives an alternative expression, but suffers the same error propagation - for inversion of a singular matrix, or close to singular, small errors in the Green function can result in large errors in the embedding potential.

Figure 4.13 shows the (00, 00) part of the Al $\Gamma^{(1)}$ function (the embedding potential obtained via equation (4.13)) for $E_{max} = 200$ and 400 eV and the rest of the parameters as for the 'standard' calculation of the previous section (ie $n_{\mathbf{k}} = 240$, $\varepsilon = 0.1$ eV and $\Delta E = 0.1$ eV). The convergence is good until the region around the zero of the Green function, where large errors are present, as expected from the discussion above. For the current calculations these convergence anomalies are unimportant as they are small below the Fermi energy ($E_f = 0.207$ Ryd for Al) and it is only at the Fermi energy and below that Γ is required to be accurate. For

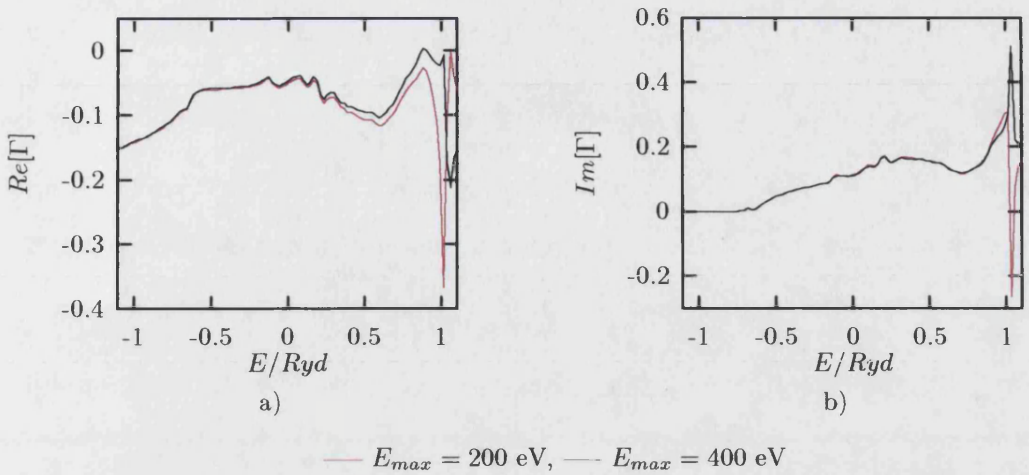

Figure 4.13: Aluminium $\Gamma_{(00,00)}$ for different E_{max} - E_{Fermi} = 0.207 Ryd.

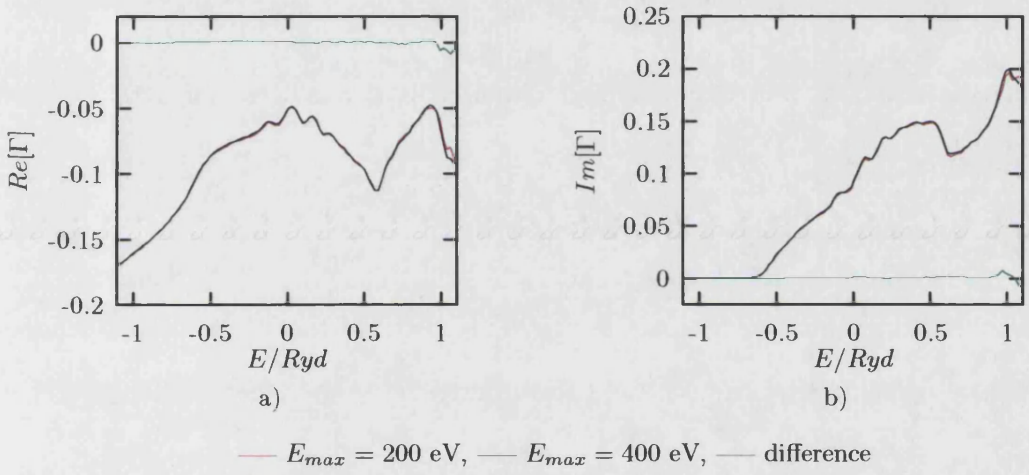

Figure 4.14: Convergence of Aluminium $\Gamma_{(10,10)}$ with E_{max}.

matrix elements with higher l the zeroes in $\mathcal{G}$ appear at higher energies, so these present no difficulties. The $(10, 10)$ matrix element for Al is shown in figure 4.14 for $E_{max} = 200$ and 400 eV. The difference between the two is less than ~ 0.002 for both the real and imaginary parts for energies below the Fermi energy, a similar residual to the original Green function, and this is typical of the residual for all but the $(00, 00)$ matrix element.

The second expression for Γ, equation (4.14), provides a notably worse approximation to Γ since this possesses poles where the normal derivative of the Green function is equal to -1 (or, in matrix terms, the identity matrix plus the normal derivative is singular). Unfortunately this occurs near zero energy for the $(00, 00)$ matrix element of Aluminium (exactly at zero for free space) making this approx-

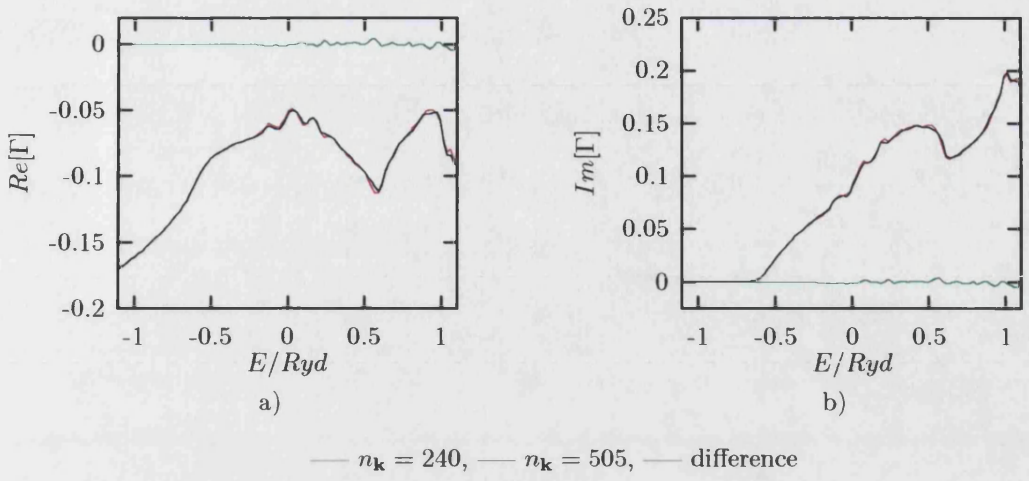

Figure 4.15: Convergence of Aluminium $\Gamma_{(10,10)}$ with $n_{\mathbf{k}}$.

imation unusable. All calculations from this point on employ equation (4.13) to obtain the embedding potential.

The Si Green function (with spatial variables on the surface of the embedding sphere) does not display the nearly free electron behaviour of Al, so has no zeroes near the energy range of interest. As a consequence of this the error is small and featureless.

Note that a combination of the two independent expressions for the embedding potential, equation (4.13) and (4.14), can be written down which possess poles at complex energy values that could be controlled (provided the zeroes of the Green function and its derivatives are available). A possible form for this would be

$$\Gamma = \left[ar_s^2\mathcal{G} + b\left(\mathcal{I} + r_s^2\frac{\partial\mathcal{G}}{\partial n_1}\right)\right]^{-1}\left[ar_s^2\mathcal{G}\Gamma^{(1)} + b\left(\mathcal{I} + r_s^2\frac{\partial\mathcal{G}}{\partial n_1}\right)\Gamma^{(2)}\right] \qquad (4.18)$$

where a or b can be complex, matrices or functions of E, and would be chosen to ensure that any poles in the approximation are well under control. This expression reduces to either equation (4.13) or (4.14) for $a = 0$ or $b = 0$ respectively.

Convergence of Brillouin Zone Integral

Figure 4.15 shows the $(10, 10)$ element of the embedding potential matrix for Al for 240 and 505 $\mathbf{k}$ points within the irreducible wedge, together with the difference between them. The convergence of Γ is as good as for the Green functions they are

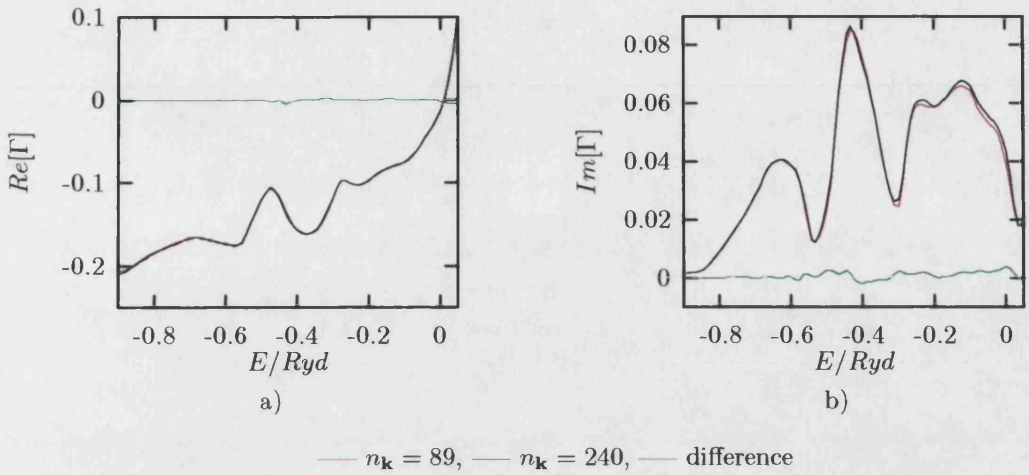

Figure 4.16: Convergence of Silicon $\Gamma_{(10,10)}$ with $n_{\mathbf{k}}$.

obtained from, with no artifacts introduced by the expression for the embedding potential. A maximum difference of ≈ 0.005 is found between the results for 505 and 240 **k** points.

Figure 4.16 shows the same quantity for Si with 89 and 240 **k** points within the irreducible wedge. The errors for Al and Si appear to be comparable in magnitude, but for Si the error is highest (and strongly localised) at van Hove singularities, and for Al the error is highest in the region of band crossing.

For both cases a satisfactory starting point for applying the embedding potentials was taken to be 240 **k** points within the irreducible wedge.

Convergence of Γ with ΔE

Figures 4.17 and 4.18 show the convergence of the embedding potentials for Al and Si with the parameter ΔE of the convolution integral used to obtain the Green function from the spectral function (see section 3.5). This shows the same convergence behaviour as for the Green functions themselves, as discussed in section 4.3.4 - no artifacts are introduced by the expression for the embedding potential.

For both Al and Si there are few discernible differences between calculations with ΔE of 0.1 eV and 0.3 eV; what small errors are present (less than 0.001 for both real and imaginary parts and this matrix element) appear to be localised to regions of fine structure, as would be expected.

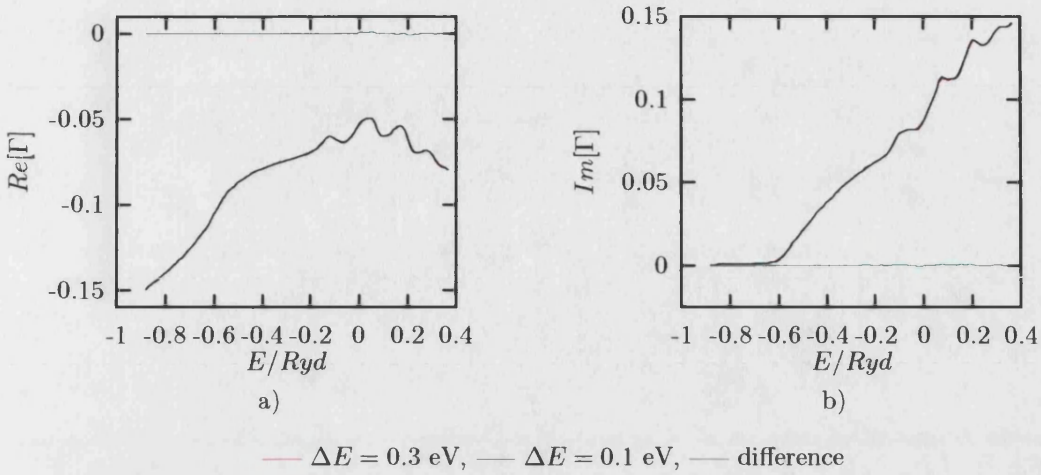

Figure 4.17: Convergence of Aluminium $\Gamma_{(10,10)}$ with spectral function sampling interval, ΔE (linear interpolation).

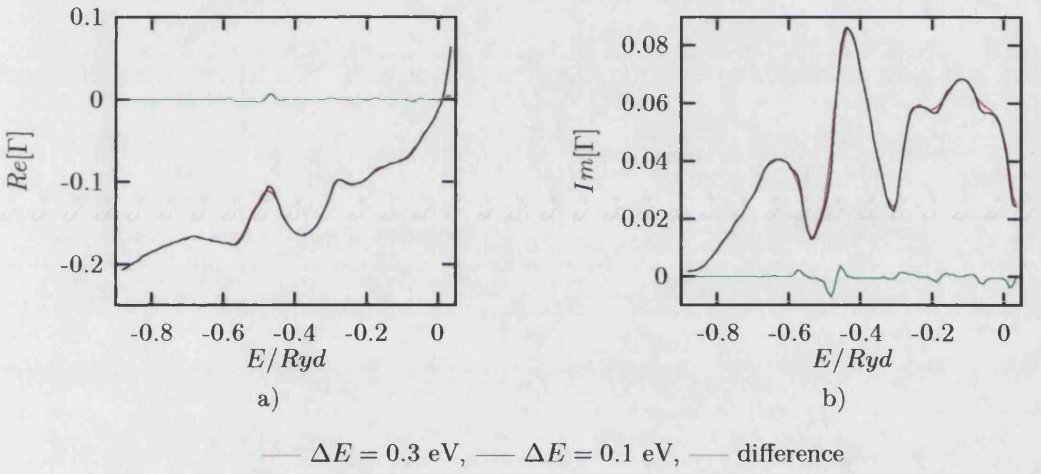

Figure 4.18: Convergence of Silicon $\Gamma_{(10,10)}$ with spectral function sampling interval, ΔE (linear interpolation).

For Si the peak at ~ -0.5 Ryd has clearly not converged perfectly, as would be expected for a polynomial approximation to such a singular feature (which is present in the spectral function, $\mathcal{F}$), but the overall convergence is good.

At this point it should be mentioned that the efficiency of the convolution integral can be improved significantly by using different step sizes for different energy ranges of the spectral function, $\mathcal{F}$. Over the range where the fine structure of $\mathcal{F}$ is important a fine spacing is required. In the region above this ($\mathcal{F}$ for E well above the Fermi energy) a much coarser spacing can be used as the only contribution that the spectral function makes to $\mathcal{G}$ (through the convolution integral) takes the

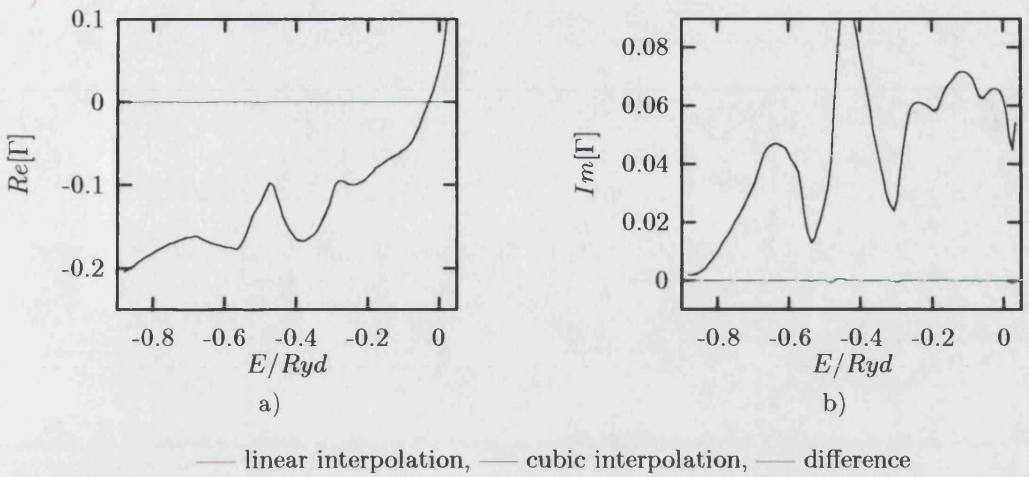

Figure 4.19: Silicon $\Gamma_{(10,10)}$ for linear and cubic polynomial interpolation of $\mathcal{F}$, $\Delta E = 0.1$ eV.

form of a low order polynomial in $E + i\varepsilon$ (see section 4.2). This is a result of the contribution from the high energy spectral function being insensitive to the fine structure in the higher energy region. As a consequence of this the structure of $\mathcal{F}$ requires a much less detailed description above the Fermi energy.

It was found that for Al and Si the choice of spacing 0.1 eV below 5 eV, and 1 eV spacing above gave results indistinguishable from 0.1 eV over the full range of the spectral function. This reduced the number of spectral function sample energies from $\sim$ 2800 to $\sim$ 400, and would be particularly useful if the method is to be applied to materials requiring a large E_{max}.

A cubic interpolation scheme was also investigated for the convolution integral. Figure 4.19 compares the results from the linear and cubic interpolation schemes, for Si with a ΔE of 0.1 eV. The difference between the cubic and linear interpolation schemes is negligible for this ΔE. For a larger ΔE the cubic method applied to Al is only slightly more efficient, and applied to Si the cubic method is *worse* than linear interpolation, as discussed in section 4.3.4.

4.4.3 Effect of Including Only a Subset of Bands

In this section the effect of including only a subset of the bands resulting from the CASTEP calculations is investigated. It would obviously be advantageous if only a small number of low energy bands were required to be included in the calculation

of the embedding potential, ideally only the occupied bands. It might be hoped that this is the case on physical grounds, since the embedding potential is only required to reproduce the correct occupied states - states above the Fermi energy are entirely irrelevant (within DFT they are incorrect anyway).

However, the 'topping up' corrections required to ensure that the spectral representation of the Green function is made up of a complete set of states (see section 4.3) suggest there may be difficulties with this idea. The fact that the spectral representation requires these states to be present in order to *be* a Green function and that the high energy states have a significant influence on the Green function (and embedding potential) in the low energy region implies that these high energy states are important. This is clearly demonstrated by the convergence of Γ with E_{max} discussed above.

This situation can be clarified by examining exactly what Hamiltonian (or more specifically what potential) the *approximate* Green function is associated with. So far the states have been taken as the result of a full matrix diagonalisation, and free electron states have been added to this to give a complete spectral representation. This gives the Green function for a system corresponding to a Hamiltonian (expressed in the plane wave basis)

$$\langle \mathbf{k}+\mathbf{g}|-\nabla^2+V_{eff}|\mathbf{k}+\mathbf{g}'\rangle = \begin{pmatrix} \langle \mathbf{k}+\mathbf{g}|-\nabla^2+V_{sc}|\mathbf{k}+\mathbf{g}'\rangle & \mathbf{0} \\ \mathbf{0} & |\mathbf{k}+\mathbf{g}|^2\delta_{\mathbf{g}\mathbf{g}'} \end{pmatrix} \quad (4.19)$$

where V_{sc} is the non-local self consistent potential that provides the CASTEP states. The potential V_{eff} implied by this set of orthonormal states (CASTEP low energy states and free electron high energy states) is the potential that the embedding potential calculated with the topping up method will represent.

From this viewpoint it appears that there is no justification for only including a few low energy bands and topping up the rest with plane wave states, as this spectral representation cannot be written in the simple form described above (the set of states is not orthonormal, so the spectral representation cannot satisfy a Green function equation).

However, the above discussion does not take into account the fact that the embedding potential is only defined on the embedding surface, so the Green function is only required on this surface. In terms of the set of states of the substrate system, the states (and their normal derivative) are only required on the embedding

surface.

Another way of viewing this is that the embedding potential represents the scattering properties of the potential of the substrate system outside of the embedding surface. This potential is entirely characterised by the *complete* set of eigenfunctions and their normal derivatives *on the embedding surface*, and this explains why a full set of states are required to construct the embedding potential.

As a consequence of this a spectral representation constructed with some set of eigenfunctions on the surface (in this case a subset of the CASTEP states and free space) will represent a substrate potential that:

- Has the same eigenvalues as the states used to construct the spectral representation.
- Has eigenfunctions (and their normal derivatives) *at the embedding surface* that are the same as those used to construct the spectral representation.

So, if the spectral representation has the correct low energy states, incorrect high energy states may still imply a substrate potential that differs significantly from the correct substrate potential.

In view of this discussion it seems reasonable to try to approximate the embedding potential from a spectral representation of the Green function using only the lowest energy n bands and topping up the rest with free space. The spectrum of eigenstates will no longer consist of an orthonormal set, but this is unimportant as long as the potential implied by this set of states at the sphere surface is reasonable, and whether this is the case or not must be assessed. Here the convergence of the embedding potential with the number of bands included is examined.

The spectral functions, $\mathcal{F}$, are calculated exactly as before except that only the lowest energy n_{bands} bands are summed for both the pseudo-states and the numerical free electron states (ie $\mathcal{F}^{pseudo}$ and $\mathcal{F}^{free}$ in equation (4.9)). Figure 4.20 shows the $(10,10)$ matrix element of the embedding potential for Aluminium at $E = -1.9 + 5.5i$ Ryd (this is chosen arbitrarily as one of the energies employed in the contour integration described in chapter 5) and $n_{bands} = 3$ to 113 bands out of the original 113 included. By $n_{bands} = 90$ there is little variation with increasing energy bands included, and the embedding potential can be considered converged. In itself this is no great advantage, but for quite low n the error due to the lack of

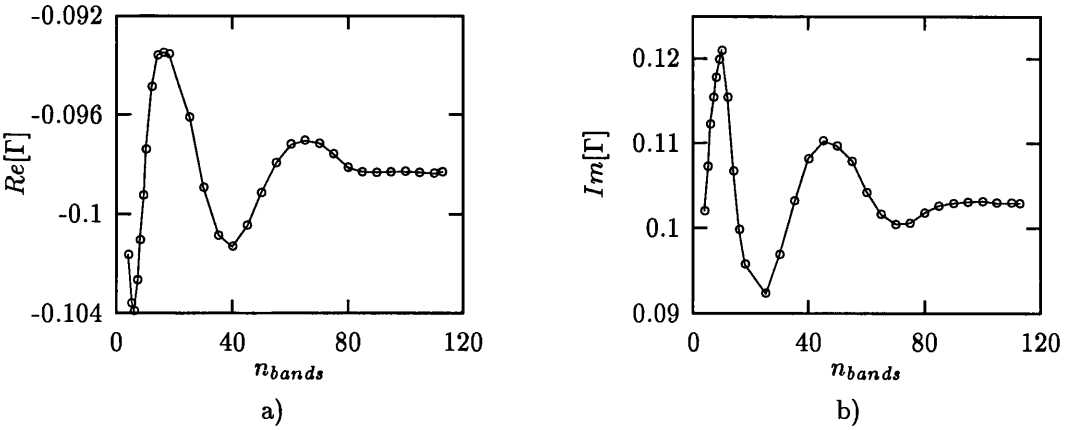

Figure 4.20: $\Gamma_{(10,10)}$ for Aluminium with only lowest n_{bands} included.

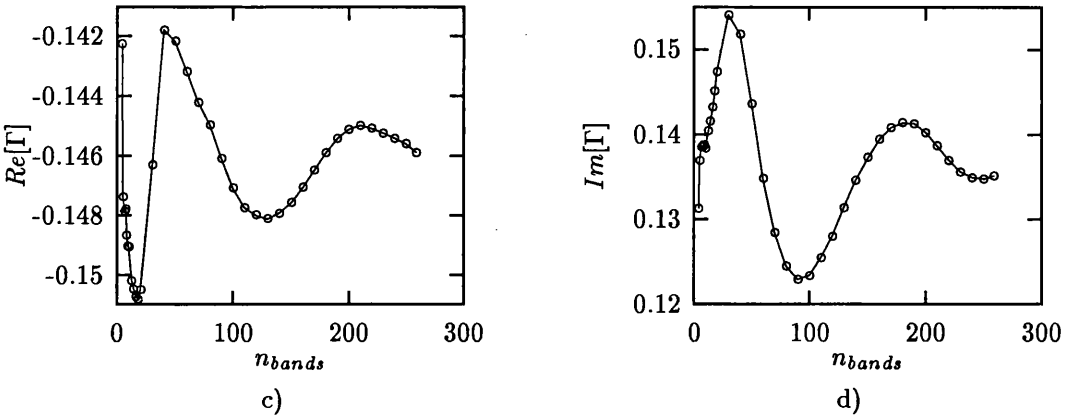

Figure 4.21: $\Gamma_{(10,10)}$ for Silicon with only lowest n_{bands} included.

convergence is comparable to some of the errors so far encountered. Figure 4.21 shows the same element for Silicon at $E = -4.8 + 5.9i$ Ryd, for $n_{bands} = 4$ to 259.

This 'sub-band' embedding potential is retained and investigated for actual embedding calculations largely because of the physical argument that only the lower bands should be important, and not in view of its convergence behaviour - even if it is not converged the substrate potential it represents may still be a good enough description of the substrate system to be useful. In Chapter 5 embedding calculations are carried out with this sub-band embedding potential.

4.4.4 Convergence with Matrix Dimension

Finally, the convergence of the embedding potential matrix with the *size* of the matrices employed is investigated. A limit must be placed on the number of spherical harmonics used to represent the spatial variation over the embedding sphere.

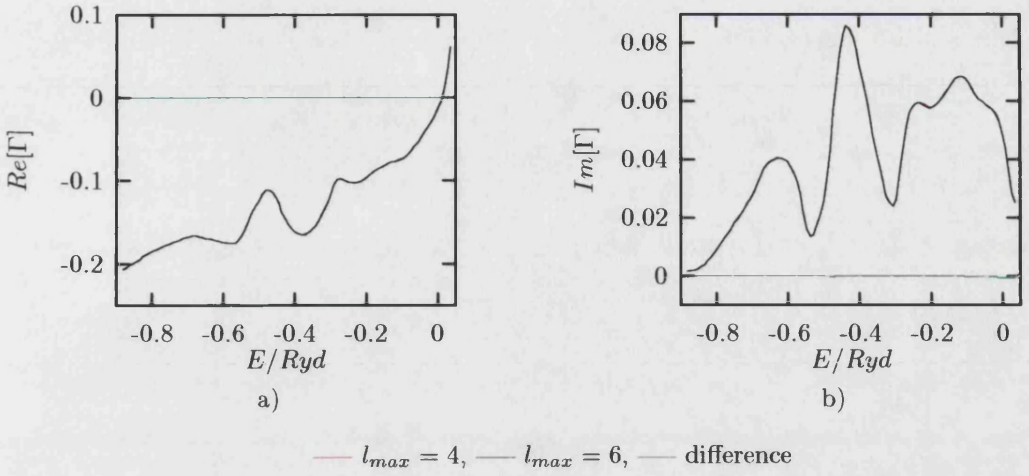

Figure 4.22: $\Gamma_{(10,10)}$ for Silicon, different l_{max}

This limit is here denoted l_{max}, the maximum l value of the spherical harmonics present.

A general system (including the crystalline systems considered here) does not possess spherical symmetry, so the Green function matrices and the embedding potential matrices will not be diagonal (as is the case of a free electron). In principle this means that the inversion and multiplication of matrices required to obtain Γ (section 4.4.1) requires the knowledge of the *entire* matrix, with an infinite number of matrix elements. This means that even if we only require the lowest $l_{max} \times l_{max}$ embedding potential sub matrix, this will depend on the entire (infinite) Green function matrix.

The $(10, 10)$ matrix element for Si (for the standard calculation parameters described earlier) is shown in figure 4.22. This shows negligible difference between the matrix elements for the cases of $l_{max} = 4$ and 6, and for the other matrix elements present the accuracy is comparable. In view of this it seems reasonable to conclude that this truncation is justified and that the main factor in the choice of l_{max} will not be the convergence of the matrix inversion required to calculate Γ - provided the elements are present, they will be sufficiently accurate.

4.5 Conclusion

For numerical calculations of eigenfunctions of a system only a finite number of states can ever be solved for, whereas the spectral representation of a real space Green function requires an infinite number of states. In order to apply the spectral representation with only a finite number of eigenstates available this must be taken into account, as described in the first section of this chapter. The behaviour of the error term introduced by an incomplete set of states in the spectral representation is examined analytically for a free electron gas. A method is then proposed to approximately correct for the incomplete spectral representation described in chapter 3.

Following this the Green functions for Al and Si are calculated using the theory outlined in this and the previous chapter, and the convergence assessed. The embedding potential is then derived from these Green functions, and the convergence of the embedding potential assessed. In both cases good convergence with the parameters of the calculation is achievable. Convergence is achieved for the 'standard' calculation with $n_{\mathbf{k}} = 240$ k-points, $E_{max} = 200$ eV and a spectral function sampling interval of 0.1 eV below 5.0 eV and 1.0 eV above 5.0 eV ($\sim$ 400 samples).

The most important conclusion of this chapter is that accurate embedding potentials can be constructed from plane wave pseudopotential calculations. It should be noted that the size of error in the embedding potential that can be tolerated when an embedding calculation is carried out can not be assessed until the embedding calculation itself is carried out, in the next chapter.

Chapter 5

Embedded All-Electron Calculation

5.1 Introduction

In chapter 2 the embedding potential method of Inglesfield (1981) was described, and some model calculations presented. In chapters 3 and 4 a method is described for the accurate calculation of a Green function from a limited set of eigenfunctions, particularly from a set of eigenfunctions calculated in a plane wave basis and using pseudopotential methods. This Green function could have a number of applications as it is a powerful analytic tool for addressing perturbation and many-body problems accurately. In this thesis this Green function is used to construct an embedding potential, and the application of this embedding potential is described here.

In this chapter the all-electron calculation carried out in the region near the nucleus is described. In what follows it is assumed that the embedding potential is available.

The all-electron calculation is carried out in a sphere centred at a nucleus (the 'embedding sphere') with the pseudopotential calculation providing the boundary conditions at the surface of this sphere. Many previous solutions of this problem have required spherical symmetry of the boundary conditions of the charge density at the embedding sphere surface, as discussed in chapter 1. The main advantage of the embedding approach is that it *does not require spherical symmetry* in these

boundary conditions or within the core region for either the charge density or the potential.

The all-electron calculation is carried out within the normal density functional framework, with the Kohn-Sham Hamiltonian extended by the addition of the embedding terms. Since these extra terms are functions of energy the eigenvalue solution of the Hamiltonian is not simple, hence the charge density is obtained directly from the Hamiltonian (via the Green function of the *embedded* system). This is implemented using the Green function method as described by Williams et al (1982).

The method employed in the all-electron calculation is essentially that used by other workers (eg Trioni et al, 1996) generalised so as not to require any particular symmetry of the charge density or self-consistent potential, and to include core electrons.

5.2 The Embedded All-electron Calculation

The all-electron self consistent embedded calculation is described in this section, and is based on Density Functional Theory (DFT) within the Local Density Approximation (LDA), as described in chapter 3.

The calculation proceeds through an iterative cycle, starting with a trial potential. From this the *embedded Hamiltonian* is constructed - a Hamiltonian defined in the embedding region only that includes the embedding potential, as described in chapter 2 - using a suitably chosen basis set. From this a Green function is obtained, and the valence charge density is derived from this in sections 5.2.2 and 5.2.3. Following this the core states of the embedded atom are calculated, and the charge density associated with these states is added to the valence charge density to give the total charge density. From this total charge density a new trial potential is derived, as described in chapter 3, and in section 5.2.4 within this chapter. This procedure is repeated starting with the new potential until self consistency is achieved.

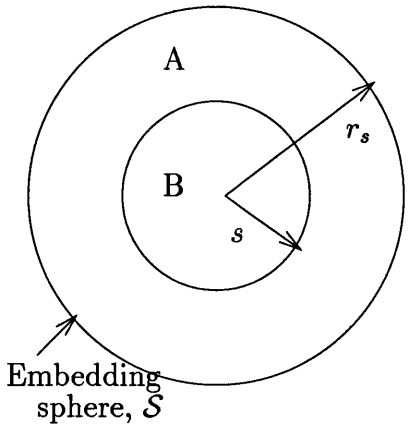

Figure 5.1: The embedding region. In A basis functions are Bessel functions, in B LAPW are used.

5.2.1 The Embedded Hamiltonian

The embedding sphere is divided into two parts, regions A and B, as shown in figure 5.1. A set of basis functions is constructed for the description of the valence electrons. Each function is a product of a radial function and a spherical harmonic, with the radial part of each basis function defined as an augmented plane wave in region B and spherical Bessel function in region A. These are chosen since Linearised Augmented-Plane-Waves (LAPW) orbitals describe the (all-electron) valence states well near the nucleus, and in the region nearer the embedding radius the spherical Bessel functions provide the flexibility required to satisfy the boundary conditions. Care must be taken to ensure that the chosen basis functions are flexible enough for a wave function constructed from them to satisfy arbitrary boundary conditions at $\mathcal{S}$ (see figure 5.1).

The basis functions in region B are found by solving the Dirac equation using numerical integration in the spherical part of the trial potential. The method used is that described by Koelling and Harmon (1977), where the Dirac equation is approximated in the form of a Schrödinger equation which does not include spin-orbit interaction but takes other relativistic effects (mass-velocity, Darwin and higher order terms) into account. A solution is found at a fixed 'pivot' energy, E_p, and the resultant radial functions are denoted $u_l(r)$. The energy derivative of these functions are also obtained and orthogonalised to the associated $u_l(r)$, and these orthogonalised energy derivatives are denoted $\dot{u}_l(r)$ (see Krasovskii, 1997 or Takeda and Kübler, 1979).

In A the radial basis functions used are spherical Bessel functions of the first kind, defined as $j_l(g_i r)$ where $g_i = \frac{\pi i}{d}$. The parameter i is chosen to take integer values, to give a set of functions, and d is a parameter of the calculation (larger than r_s to allow sufficient flexibility for the basis functions to satisfy the boundary conditions).

From this it can be seen that the basis functions, denoted $\chi_{il}(r)Y_{lm}(\hat{\mathbf{r}})$, take the form

$$\chi_{il}(r) = \begin{cases} a_{il}u_l(r) + b_{il}\dot{u}_l(r) & 0 \leq r \leq s \\ j_l(g_i r) & s < r \leq r_s \end{cases} \tag{5.1}$$

where s is the radius of the boundary sphere between A and B. The parameters a_{il} and b_{il} are chosen to ensure χ_{ilm} is continuous in amplitude and derivative at the AB boundary, leading to the equation

$$\begin{pmatrix} a_{il} \\ b_{il} \end{pmatrix} = \begin{pmatrix} u_l(s) & \dot{u}_l(s) \\ \frac{\partial u_l}{\partial r}\Big|_s & \frac{\partial \dot{u}_l}{\partial r}\Big|_s \end{pmatrix}^{-1} \begin{pmatrix} j_l(g_i s) \\ \frac{\partial j_l}{\partial r}\Big|_s \end{pmatrix}. \tag{5.2}$$

Typically r_s is chosen to be half the distance between nearest neighbour atoms in the lattice, $s \sim 0.9r_s$ and $d \sim 2r_s$ to give basis functions that give a good description of the valence electrons. For i the range $1 \ldots 5$ is typical. The parameters used for actual calculations are described in section 5.3.

The embedded Hamiltonian matrix is then expanded in terms of these basis functions, for a trial potential given by

$$V(\mathbf{r}) = \sum_L V_L(r)Y_L(\hat{\mathbf{r}}) \tag{5.3}$$

where $L = (lm)$, the index of the spherical harmonic. The embedded Hamiltonian matrix, $\langle \chi_{iL} \mid \mathcal{H}_{emb} \mid \chi_{jL'} \rangle$ is here written as the sum of 3 parts,

$$\mathcal{H}_{emb} = \mathcal{H}^A + \mathcal{H}^B + \mathcal{E} \tag{5.4}$$

with $\mathcal{H}^A$ the contribution from region A, $\mathcal{H}^B$ the contribution from region B, and $\mathcal{E}$ the contribution from the embedding terms at the surface $\mathcal{S}$.

The contribution from region A is given by

$$\mathcal{H}^A_{iL,jL'} = \frac{1}{2}g_j^2 \int_s^{r_s} r^2 dr \left[j_l(g_i r) j_l(g_j)\right] \delta_{LL'} + \sum_{L''} S^L_{L'L''} \int_s^{r_s} r^2 dr \left[j_l(g_i r) V_{L''}(r) j_{l'}(g_j r)\right] \tag{5.5}$$

where $S^L_{L'L''} = \int Y^*_L Y_{L'} Y_{L''} d\Omega$ are Gaunt coefficients.

The contribution from region B is the sum of contributions from the spherical and aspherical parts of the Hamiltonian in B

$$\mathcal{H}^B_{iL,jL'} = \left[a_{il}a_{jl}E_p\langle u_l \mid u_l\rangle + a_{il}b_{jl}\langle u_l \mid \dot{u}_l\rangle + b_{il}b_{ji}E_p\langle \dot{u}_l \mid \dot{u}_l\rangle\right]\delta_{LL''}$$

$$+$$

$$\sum_{L''\neq 0} S^L_{L'L''} \int_0^s r^2 dr \left[\left(a_{il}u_l + b_{il}\dot{u}_l\right) V_{L''}(r) \left(a_{jl'}u_{l'} + b_{jl'}\dot{u}_{l'}\right)\right] \tag{5.6}$$

where E_p is the 'pivot' energy at which $u_{il}(r)$ is calculated, and the bra-ket's denote integration over region B only. The integrals in the above expressions are carried out analytically or numerically as appropriate.

The contribution from the embedding terms, $\mathcal{E}$, is given by

$$\mathcal{E}_{iL,jL'} = j_l(g_i r_s)\Gamma_{LL'}(E) j_{l'}(g_j r_s) + \frac{1}{2} g_j j_l(g_i r_s) j_{l'}(g_j r_s)\delta_{L,L'}, \tag{5.7}$$

which is derived from the normal derivative and embedding potential terms in equation (2.15), together with the expansion of the embedding potential in equation (4.12). The embedded Hamiltonian is obtained from the sum of these three terms.

In addition to the Hamiltonian matrix the overlap matrix of the basis functions, $\langle \chi_{iL} | \chi_{jL'}\rangle = \mathcal{O}_{il,jL'}$ is also required. This is given by

$$\mathcal{O}_{iL,jL'} = \delta_{LL'} \int_s^{r_s} j_l(g_i r) j_l(g_j r) r^2 dr + \delta_{LL'}\left[a_{il}a_{jl}\langle u_l \mid u_l\rangle + b_{il}b_{jl'}\langle \dot{u}_l \mid \dot{u}_{l'}\rangle\right] \tag{5.8}$$

where the first integral on the RHS can be performed analytically (Abramowitz and Stegun, 1964) and the second numerically.

5.2.2 The Embedded Green function and Local Density of States

The next step is to obtain the Green function from the embedded Hamiltonian, and to obtain the local density of states from this. The valence charge density may then be calculated by integrating over the occupied states.

The Green function is obtained directly by matrix inversion,

$$\mathcal{G}(E) = (\mathcal{H}_{emb}(E) - E\mathcal{O})^{-1}, \tag{5.9}$$

where $\mathcal{H}_{emb}$ is the embedded Hamiltonian described above.

The local DOS, $n(\mathbf{r}; E)$ is then obtained from the identity (Economou, 1990)

$$n(\mathbf{r}; E) = \frac{1}{\pi}\text{Im } G(\mathbf{r}, \mathbf{r}; E). \tag{5.10}$$

We require the local density of states expanded in spherical harmonics, or

$$n(\mathbf{r}; E) = \sum_L n_L(r; E) Y_L(\hat{\mathbf{r}}), \tag{5.11}$$

so equation (5.10) becomes

$$n_{L''}(r; E) = \frac{1}{2\pi} \sum_{ijLL'} \chi_{il}(r)\chi_{jl'}(r) \left(\mathcal{G}_{iLjL'} S^{L'}_{LL''} - \mathcal{G}^*_{iLjL'} S^{L}_{L'L''}\right) \tag{5.12}$$

where $S^L_{L'L''}$ is a Gaunt coefficient, and zero for $l'' > 2l$ or $2l'$ so a $l_{max} \times l_{max}$ Hamiltonian matrix will result in a charge density containing components $l \leq 2l_{max}$. It is due to the basis functions being complex (the spherical harmonics are complex) that this expression does not simply involve the imaginary part of the Green function matrix.

5.2.3 The Charge Density

The valence charge density is obtained by filling all states to the Fermi energy (obtained from the original pseudopotential calculation using the tetrahedron method described in chapter 3). The local density of states has a fine structure, so the number of points required to evaluate it by direct integration is fairly high.

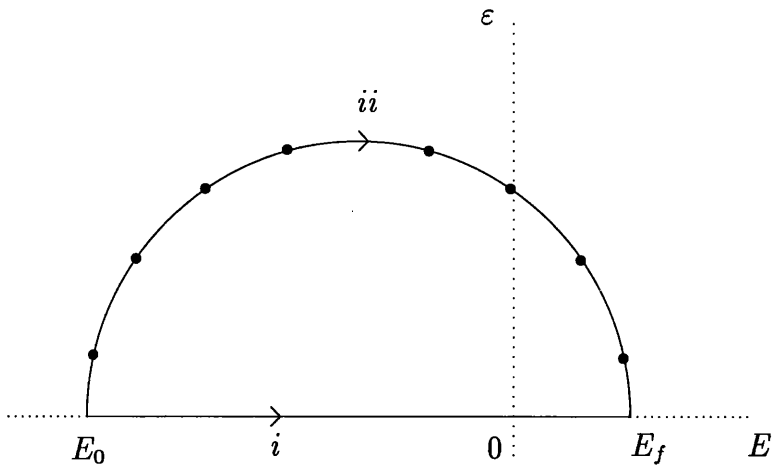

Figure 5.2: Contour paths for integral over occupied states. E_0 is below the bottom of the 1^{st} band, and E_f is the Fermi energy.

This can be avoided be taking advantage of Cauchy's theorem and the analytic properties of the Green function. The imaginary part of the Green function integrated over path i in figure 5.2 (with $\mathbf{r} = \mathbf{r}'$) is the charge density, due to equation 5.10. However, since the Green function is an analytic function, and no poles are present in the upper half of the complex plane the identity

$$\int_i G(\mathbf{r}, \mathbf{r}'; E) = \int_{ii} G(\mathbf{r}, \mathbf{r}'; E) \tag{5.13}$$

is provided by Cauchy's theorem (Morse and Feshbach, 1953), where the contour ii is also shown in figure 5.2. As the imaginary part of the energy increases the Green function becomes smoother and more featureless, hence a more sparse sampling is sufficient to approximate the integral accurately. So, applying equation (5.13) and (5.10) gives the valence charge density as

$$\rho^{val}(\mathbf{r}) = \frac{1}{\pi} Im \left[\int_{ii} G(\mathbf{r}, \mathbf{r}; E) \right] \tag{5.14}$$

and the expansion in spherical harmonics is given by a similar expression to equation (5.12).

Gaussian integration (Press et al, 1994) is used to perform the integral along contour ii, and converged integrals are typically obtained for around 16 points on the contour.

Core charge density

In addition to the valence charge density the contribution to the total charge density given by the core electrons must also be calculated, to give

$$\rho_L(r) = \rho_L^{val}(r) + \rho_L^{core}(r). \tag{5.15}$$

The core states could be obtained by finding the discrete states of the embedded Hamiltonian in a similar manner to that described in chapter 2, which would be equivalent to finding the bound states of the potential shown schematically in figure 2.7(b). This is a fairly cumbersome method of solving for the core states, especially given that these states are well localised within the embedding sphere (vital for the pseudopotential to describe the valence states adequately) so the potential outside of the embedding sphere is largely irrelevant to the core states. It should be noted that for the embedding method applied here the core states are truly localised, since we are embedding an all-electron atom at one site within a lattice of pseudo-atoms.

In view of the unimportance of the potential outside the embedding sphere the core states are solved for the trial potential inside the sphere, and a constant potential outside the sphere. Only the spherically symmetric part of the potential is used to obtain the states, and the constant potential outside the sphere is taken to be continuous with the spherical part. This spherically symmetric approximation has been used by many workers (eg Blaha et al, 1988; Methfessel and Frota-Pessô, 1990), and can easily be extended to included aspherical effects perturbatively as described by Ehmann and Fähnle (1997), Sternheimer (1986) and Lauer et al (1979). Ehmann and Fähnle have applied these corrections to FLAPW calculations of the electric field gradient of a number of materials, and conclude that although the contribution of core asymmetry is negligible for many materials, in some cases it must be considered in order to obtain reliable EFG's.

To obtain the core charge density a fully relativistic treatment is used, solving the Dirac equation within the embedding region to find the core states and filling the states to obtain the core charge density (Inglesfield, 1996). This equation is solved numerically using standard techniques, with the spherical average of the trial potential within s, and a constant potential outside of s so the eigenfunctions decay exponentially. This leads directly to the required core charge density, $\rho^{core}(\mathbf{r})$. Since this is spherically symmetric, only the $L = (00)$ coefficient of the spherical

harmonic expansion is non-zero.

5.2.4 Self Consistency

A new trial potential is calculated from total charge density via DFT and the LDA, as described in chapter 3. The potential due to the total charge density and the atomic nucleus is the sum of three parts,

$$V_{lm}^{new}(r) = V_{lm}^{Nuc}(r) + V_{lm}^{Hart}(r) + V_{lm}^{XC}(r), \tag{5.16}$$

the nuclear potential, the Hartree potential due to electrostatic interactions between the electrons, and the exchange-correlation potential due to many-body effects. These are described below.

The nuclear potential

This is presumed to be that of a point charge centred at the nucleus, hence is given by

$$V_{lm}^{Nuc}(r) = \left\{ \begin{array}{cc} -2\sqrt{4\pi}\frac{Z}{r} & l=0 \\ 0 & l \neq 0 \end{array} \right\} \tag{5.17}$$

where Z is the atomic number of the nucleus (Rydberg units are used).

The Hartree potential

Poisson's equation is solved to obtain the Hartree contribution. The general solution (for a distributed charge) expanded in spherical harmonics takes the form

$$\begin{aligned} V_{lm}^{Hartee}(r) \;=\; & \frac{4\pi}{2l+1}\frac{1}{r^{l+1}}\int_0^r [r'_l \rho_{lm}(r')]\, r'^2 dr' + \\ & \frac{4\pi}{2l+1} r^l \int_r^{r_s} \left[\frac{1}{r'^{l+1}}\rho_{lm}(r')\right] r'^2 dr' + \\ & a_{lm} r^l \end{aligned} \tag{5.18}$$

where a_{lm} is a constant defined by the boundary conditions of the potential at the embedding surface (Morse and Feshbach, 1953), and these integrals are evaluated numerically. It should be noted that the boundary conditions require the

total potential to equal the original pseudopotential self-consistent potential on the embedding sphere.

The Exchange-Correlation potential.

LDA is used to obtain the exchange-correlation potential from the charge density. Although other approximations could be used, it has been shown that consistency in the choice of approximation to the exchange-correlation functional is required for pseudopotential calculations, and this is likely to be the case for embedding calculations as well (Fuchs et al, 1998). The Ceperly-Alder parameterisation was employed (Ceperly and Alder, 1980).

The LDA exchange-correlation potential is a non-linear function of the charge density, and as a consequence of this it cannot be directly applied to the spherical components of the charge density to obtain the spherical components of the XC potential. To arrive at the expansion of the XC potential, the charge density could be expanded in real space, the real space XC potential calculated from this, and the real space XC potential expanded in spherical harmonics.

Alternatively, if the XC potential is expanded as a Taylor series

$$V^{XC}(\rho) = V^{XC}(\rho_0) + \left.\frac{\partial V^{XC}}{\partial \rho}\right|_{\rho_0} (\rho - \rho_0) + \cdots \tag{5.19}$$

then truncating this series should give a good approximation provided that $\rho_0 - \rho$ is small compared to ρ_0.

In the present case ρ_0 is taken as the spherical part of the charge density (deviations from this are expected to be relatively small) and the expansion truncated at the linear term. A higher order expression could easily be employed, but a second order expansion was not found to improve the accuracy of any of the calculations presented in this thesis.

Using these approximations, with $\rho_0 = \rho_{00} Y_{00}$, the expansion coefficients are

$$V_{lm}^{XC}(r) \approx \begin{cases} \frac{1}{Y_{00}} V^{XC}(\rho_0(r)) & l = 0 \\ \left.\frac{\partial V^{XC}}{\partial \rho}\right|_{\rho_0} \rho_{lm}(r) & l \neq 0 \end{cases} \tag{5.20}$$

where $Y_{00} = \frac{1}{\sqrt{4\pi}}$, the zero order spherical harmonic.

Imposing boundary conditions on the total potential

On the surface of the embedding sphere the potential in the embedded calculation must equal the self consistent potential from the original pseudopotential calculation.

If the self-consistent potential from the pseudopotential calculation is given by $V_L^{pseud}(r_s)$ when expanded in spherical harmonics, the boundary conditions on the embedding surface give

$$V_L^{pseud}(r_s) = V_L^{Nuc}(r_s) + V_L^{Hart}(r_s) + V_L^{XC}(r_s) \tag{5.21}$$

This defines the coefficients a_{lm} in equation (5.18).

Self consistency is achieved by iterating the above procedure, to provide a new trial potential from the old at each step. The initial trial potential is chosen to be spherically symmetric, taking the form $c - 2Z/r$ with c chosen so the potential matches the spherical part of the original pseudopotential self-consistent potential. Instabilities in the non-linear equations solved in each iteration cause oscillations in the charge density (Payne et al, 1992) that can prevent the algorithm converging. By employing a combination of the trial potentials from previous iterations and the new trial potential these oscillations can be damped, significantly improving convergence. The scheme applied is that due to Broyden (1965) and modified by Johnson (1988). This typically increases the speed of convergence by a factor of at least 2 (see Johnson, 1988, for a brief review of mixing procedures and the Broyden mixing employed here).

Spin Polarisation

It should be noted that the generalisation of the reconstruction procedure to spin-polarised systems within the structure of the Local Spin-Density Approximation (LSDA) (Jones and Gunnarsson, 1989) is straightforward. An embedding potential is constructed from CASTEP for each spin, and the all-electron calculation carried out for each spin. Coupling between the two spin systems only becomes complex when the exchange-correlation potential is calculated, and spin dependent parameterised forms are available for this (Jones and Gunnarsson, 1989).

5.3 Results

In this section the result of carrying out the all-electron embedded calculation described above for Aluminium and Silicon are described. Total energy pseudopotential calculations provide the embedding potential through the method given in chapters 3 and 4, and this provides the framework to reconstruct the correct electron states within the core region from the pseudopotential calculation.

This 'core reconstruction calculation' provides:
- The total (including core states) charge density within the radius r_s.
- The density of states within the embedded region.
- A self consistent potential.
- The core eigenstates.

This section presents the results for two typical reconstruction calculations, compared with the original pseudopotential results in order to assess the accuracy of the core reconstruction.

In addition to these all-electron results, reconstruction calculations are also carried out in which no core states are included and the core and nucleus are described by a pseudopotential, the same pseudopotential used in the original CASTEP calculations. This provides a more stringent test of the accuracy and reliability of the entire embedding approach, since for a successful implementation the resulting (valence) charge density should be the same as the original CASTEP charge density throughout the embedding sphere. This is achieved, showing the validity of the approach and the algorithms used.

The effect of assuming spherical symmetry of the self consistent potential or boundary conditions (ie the embedding potential) is also briefly examined. Many past workers have assumed the spherical symmetry of one or both (see the discussion in chapter 1) of these for solving this problem simply to allow the application of standard techniques, with little justification.

In section 5.4 the convergence of the method is investigated with respect to the parameters already encountered in calculating the Green function (chapter 3) and the embedding potential (chapter 4). Convergence with the parameters of the all-electron calculation is not presented as this is easily converged, and it is the quality of the embedding potential that primarily determines the accuracy of the results.

Finally, section 5.5 uses the reconstructed all-electron states from Silicon to calculate structure factors for bulk Si. Accurate experimentally determined structure factors are available for Si, and the structure factors resulting from the core reconstruction are compared with both experimental data and recent FLAPW results. The core reconstruction calculations appear to provide results as accurate as the FLAPW method, even to reproducing the same trends in the errors.

5.3.1 Core Reconstruction for Aluminium and Silicon

In chapters 3 and 4 the method of calculating the pseudo-eigenstates using the total energy pseudopotential method is described, and how the embedding potential can be obtained from these calculations. The same method is also used to obtain the embedding potentials employed in this chapter for the core reconstruction calculations. There is no difference in how the two are calculated, only the energies differ - the results in chapter 4 evaluate Γ at 0.1 eV above the real axis, whereas the core reconstruction requires Γ on the contour shown in figure 5.2. Although we have not investigated the convergence of the embedding potential at ε values greater than 0.1 eV this was not expected to be necessary since the contour integral over path *ii* in figure 5.2 *equals* the contour integral over path *i* (along the real axis), so provided the approximation to Γ is valid on the real axis the integral over path *ii* will also be valid. In approximating this contour integral with a finite number of sample points all of the sample energies had imaginary parts greater than 0.1 eV.

For both Al and Si the total energy pseudopotential calculation was taken to self consistency for an energy cutoff of 400 eV, as described in chapter 4. The resultant self consistent potentials were employed for all the calculations in this chapter. This self consistent potential was used to obtain the full set of eigenstates by matrix diagonalisation for a plane wave basis set with a different energy cutoff and at the $\mathbf{k}$ points required for the Brillouin zone integration.

Table 5.1 shows a set of parameters that were found to give good convergence of the embedding potential in chapter 4, and these are the parameters used in this section.

Table 5.2 shows the parameters (as described in section 5.2) of the core reconstruction calculation. These either follow from the embedding potential calculation, or

by requiring convergence and stability of the reconstruction calculation. The Fermi energies used were obtained directly from the CASTEP eigenstates resulting from the matrix diagonalisation by applying the Brillouin zone integration method of chapter 3, and were not updated self consistently.

These parameters are taken as the 'standard calculation' in what follows. For all results in this chapter the parameters are as given in Tables 5.1 & 5.2, unless different values are explicitly given.

parameter	Al	Si
a_0(Å)	4.05	5.43
E_{max}(eV)	200	200
n_{bands}	113	259
$n_{\mathbf{k}}$	240	240
ΔE(eV)	0.1	0.1

a_0 - lattice constant
E_{max} - energy cut-off for plane wave basis set, $|\mathbf{g}|^2 < E_{max}$
n_{bands} - number of bands (and plane waves in basis set)
$n_{\mathbf{k}}$ - number of $\mathbf{k}$ points calculated (in irreducible wedge)
ΔE - energy spacing of sample points for spectral function, $\mathcal{F}$

Table 5.1: Parameters used for 'standard' calculation of the embedding potential.

	Al	Si
r_s(au)	2.705	2.222
s(au)	2.5	2.1
r_c(au)	2.19	2.0
n_{basis}	4	3
l_{max}	6	6
d(au)	4.0	4.0
E_f(eV)	2.816	0.324
E_p(eV)	-2.721	-2.721

r_s - radius of the embedding sphere
s - see figure 5.1
r_c - maximum core radius of the original pseudopotential
n_{basis} - number of radial basis functions for each (lm)
l_{max} - maximum l value (total number of basis functions $= (l_{max}+1)^2 n_{basis}$)
d - parameter for Bessel functions in region A (see equation 5.1)
E_f - Fermi energy
E_p - pivot energy for radial basis functions (see section 5.2.1)

Table 5.2: Parameters used for 'standard' reconstruction calculation.

A first step in assessing the accuracy of the method is to compare the valence charge, q, contained within the embedding sphere, given by

$$q = \int_0^{r_s} \rho_{00}^{val}(r) r^2 dr, \tag{5.22}$$

for the original pseudopotential calculation and the reconstruction calculation. These charges are shown in Table 5.3 for Al and Si. This quantity differs between the two since the Fermi energy in the reconstruction is taken to be the same as for the original pseudopotential calculation. If the pseudopotential approximation is valid and the reconstruction is successful then the two quantities should be extremely close, hence the difference between the two gives an indication of the success of the reconstruction. It should be remembered that any difference could be entirely due to limitations of the pseudopotential approximation itself.

The valence charge agrees extremely well, suggesting a successful reconstruction, however this is a fairly gross measure of success since it takes no account of the structure of the electron states within the embedding sphere (only the average behaviour) and compares only the spherical part of the charge density.

A more demanding measure of the accuracy of the reconstruction is to compare the charge density and/or self consistent potential of the original pseudopotential calculation with the reconstruction. As described in chapter 3 the charge density of pseudo-states and the all-electron states should agree outside of the core radius of the pseudopotential, r_c. So, for a successful reconstruction, the original pseudopotential charge density/self-consistent potential should agree with the reconstructed charge density/self-consistent potential between r_c and the embedding sphere radius, r_s.

In figure 5.3 the valence charge density for both the original and reconstructed systems is shown. Figure 5.3a shows the charge density for Al sampled along a ray in the {011} direction with the Aluminium nucleus at the origin. In figure 5.3b,

	Charge within embedding sphere/ e		
	Pseudo. calc.	reconstruction	% error
Al	2.298	2.300	0.08
Si	2.374	2.375	0.05

Table 5.3: Total charge within embedding sphere, q, for original pseudopotential and reconstruction calculation.

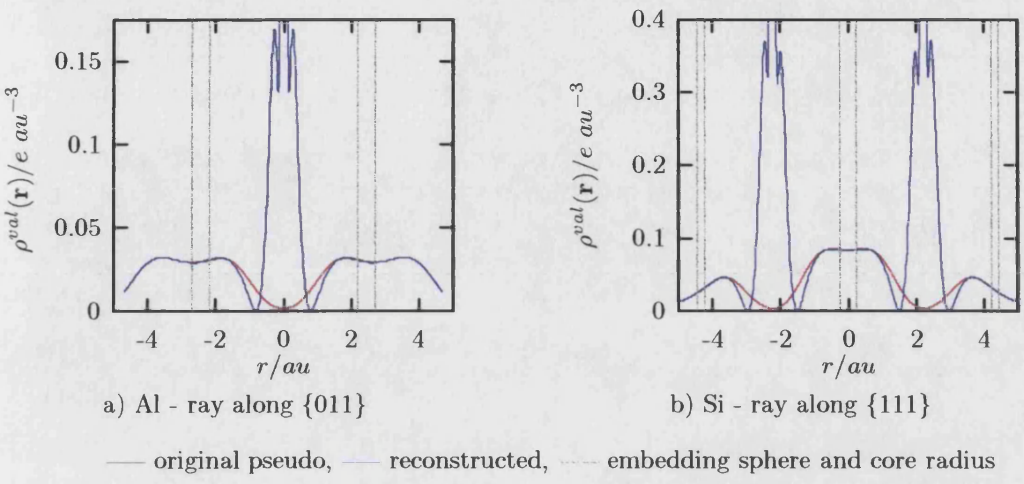

Figure 5.3: Valence charge densities for Al and Si, reconstructed and original pseudopotential results.

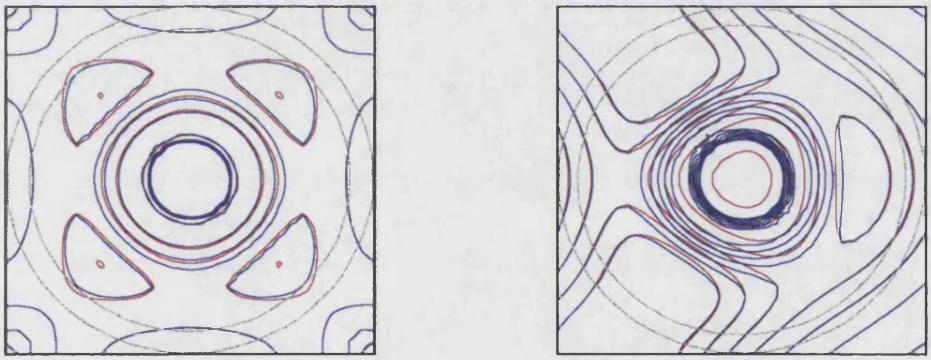

Figure 5.4: Contours of constant valence charge density on planes shown in figure 5.5 - contour levels are shown below each figure in $e\ au^{-3}$.

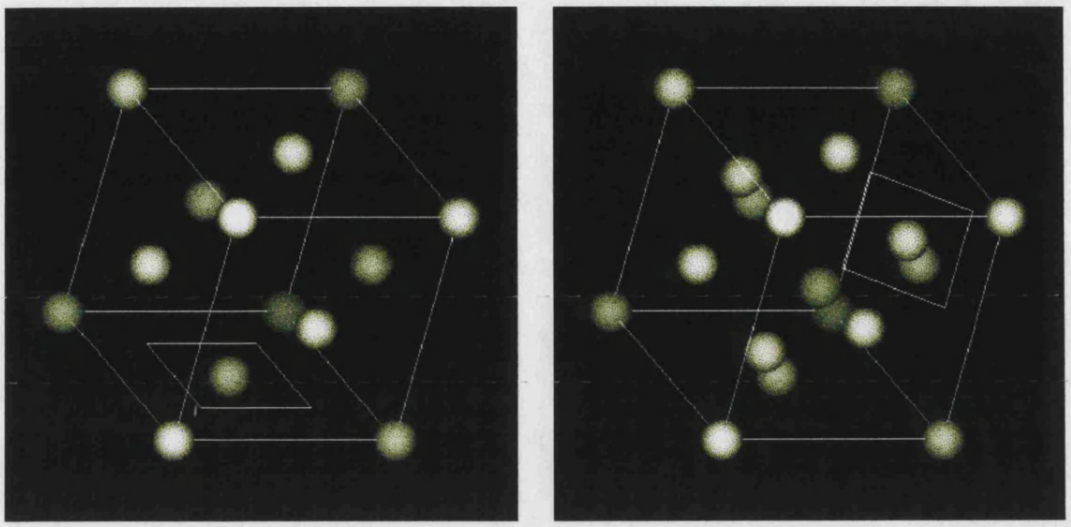

a) Al b) Si

Figure 5.5: Unit cells for Al and Si. Squares indicate planes for contour plots in figure 5.4.

the Si charge density is shown along the {111} direction through the inversion centre, with two atomic sites located on the line sampled. For both Si and Al both the core radius (r_c) and embedding radius (r_s) are shown. It is apparent from this figure that agreement is good in the required region, at least for a radial line in this direction.

We can gain an idea of the spatial variations of these charge densities by examining their behaviour over a $2d$ slice taken through the atom. Figure 5.4 shows contour plots of the $\rho^{val}(\mathbf{r})$ for Al and Si, and for both the original CASTEP and reconstruction calculations. The planes these are taken over are shown within the unit cell in figure 5.5 - the squares shown just enclose the embedding sphere (dimensions $2r_s \times 2r_s$). Again, agreement between the two results is good, with the asymmetry of the bonding reproduced.

In order to quantify the agreement between the original and reconstructed charge densities in the 'shell' between the spheres of radius r_c and r_s an error measure function is introduced, the R-factor (Press et al, 1994). This is defined as the average absolute error expressed as a percentage of the average charge density in the region, or

$$R = \int_{r_c}^{r_s} |\rho^{recon}(\mathbf{r}) - \rho^{pseud}(\mathbf{r})| d^3\mathbf{r} / \int_{r_c}^{r_s} |\rho^{pseud}(\mathbf{r})| d^3\mathbf{r}, \tag{5.23}$$

and gives a measure of the error over the whole region. Since the volume of

integration takes the form of a thin shell, R is essentially a measure of the angular variation between the original and reconstructed charge densities. The peak error, or peak difference between the original and reconstructed quantities, is also given. In most cases the peak error is $\sim 2\times$ the mean square error.

Table 5.4 shows both the peak error between the CASTEP and reconstructed charge density, and the R-factor. The peak errors are of a comparable size to those apparent in figure 5.3, and are small.

The charge density is reconstructed in the form of a spherical harmonic expansion, and each term in the expansion can be expected to show different error behaviour. In light of this it is desirable to quantify the contribution to the error made by each component of the charge density expansion. In order to achieve this Table 5.5 gives the peak error and R-factor for the reconstructed charge density only including terms satisfying $l \leq l_{top}$ with the original pseudo charge density again only including terms satisfying $l \leq l_{top}$.

For Aluminium an abrupt decrease in accuracy occurs when the $l \geq 6$ terms of the charge density are included in the comparison, both for the peak error and R. Silicon exhibits a more gradual increase in error as more terms are included in the comparison, with negligible increase in R. However a much greater increase in the peak error is apparent - this increases by a factor of ~ 5. This behaviour will be returned to in the discussion on convergence properties of the reconstruction, but it is important to note that the low l components of the charge density are significantly more accurate than the high l components, and that the largest contribution to the error is made by the high l components. This is an important point, since many of the applications of this method require only low l components of the charge density (see chapter 1).

As well as the charge density, errors in the self-consistent potential should be considered. As with ρ^{val} the reconstructed potential should agree with the original (CASTEP) potential outside of the core radius. Table 5.6 gives a similar analysis to that above of the difference between the self consistent potentials of the pseudo and reconstructed system. The % error is smaller than for the charge density, largely due to the fact that the reconstructed potential is forced to agree with the original self-consistent potential at the embedding sphere.

Error in $\rho(\mathbf{r})$ between r_c & r_s		
	peak ($e\ au^{-3}$)	$R(\%)$
Al	-5.47×10^{-4}	0.46
Si	19.95×10^{-4}	0.89

Table 5.4: Errors in charge density.

Error in $\rho(\mathbf{r})$ between r_c & r_s, including $l \leq l_{top}$				
	Al		Si	
l_{top}	peak($\times 10^{-4} e\ au^{-3}$)	$R(\%)$	peak($\times 10^{-4} e\ au^{-3}$)	$R(\%)$
0	1.29	0.18	4.46	0.88
3			8.99	0.88
4	1.29	0.19	8.74	0.88
6	−5.59	0.46	12.07	0.88
7			15.41	0.88
8	−5.11	0.46	15.59	0.88
9			17.94	0.88
10	−5.47	0.46	19.82	0.89
11			19.98	0.89
12	−5.47	0.46	19.95	0.89

Table 5.5: Errors contributed by each l component. $l_{max} = 6$ for all results shown here, hence no terms with $l > 12$ are present. l components not present are zero due to lattice symmetry.

Error in $V(\mathbf{r})$ between r_c & r_s		
	peak ($/Ryd$)	$R(\%)$
Al	-0.50×10^{-3}	0.06
Si	-1.33×10^{-3}	0.07

Table 5.6: Errors in self consistent potential resulting from reconstruction calculation.

5.3.2 Embedding with a Pseudopotential

In order to further validate the accuracy of the embedding method a reconstruction calculation is carried out using the *original pseudopotential* in the core region to represent the core electrons in the reconstruction, with no core states calculated. Provided the embedding potential and reconstruction calculation are converged this will reproduce the charge density of the original total energy pseudopotential calculation within the entire embedding sphere. In view of this the comparison of the original pseudopotential and the reconstructed *pseudopotential* systems is a good measure of the accuracy of the entire reconstruction scheme - both the quality of the embedding potential and the success of the all-electron embedding calculation.

For both Al and Si the total charge within the embedding sphere agree to the same accuracy as in the previous section (see Table 5.3). Figure 5.6 shows the charge density along a ray out from the origin in the {011} direction for Al (with atomic site at origin), and along the {111} direction for Si (inversion centre at the origin), for both the reconstructed pseudopotential calculation and the original CASTEP results. Agreement is good for both Al and Si.

Errors within the entire embedding sphere are shown in Table 5.7. The peak errors are comparable or smaller than those in Table 5.4, and the R-factor indicates an error as good or slightly smaller than those in the previous section, but it should be remembered that the errors are calculated over different regions so a direct comparison cannot be made. In view of this the errors calculated over the same region as the previous section (between the core radius r_c and the embedding radius r_s) are also given in Table 5.7. The errors are comparable to the all-electron reconstruction of the previous section, hence it seems reasonable to assume that the errors present in the all-electron reconstruction are contributed by the reconstruction process and *not* due to inadequacies of the pseudopotential approximation.

	Error in $\rho(\mathbf{r})$ within r_s		Error in $\rho(\mathbf{r})$ between r_c & r_s	
	peak ($e\ au^{-3}$)	R(%)	peak ($e\ au^{-3}$)	R(%)
Al	-5.56×10^{-4}	0.49	-5.56×10^{-4}	0.48
Si	13.68×10^{-4}	0.50	13.67×10^{-4}	0.59

Table 5.7: Errors in reconstructed $\rho(\mathbf{r})$ using pseudopotential for reconstruction.

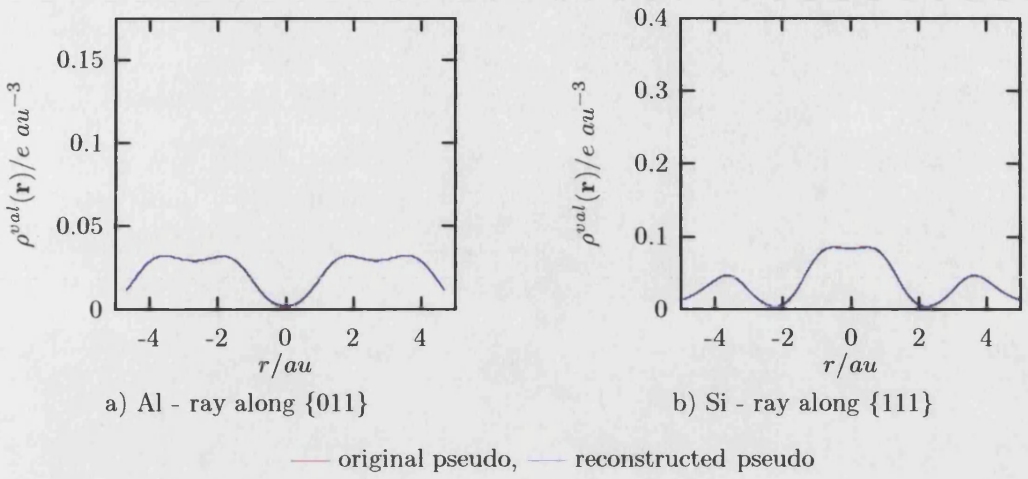

a) Al - ray along {011}

b) Si - ray along {111}

original pseudo, reconstructed pseudo

Figure 5.6: Valence charge densities for Al and Si, reconstructed pseudopotential and original pseudopotential results.

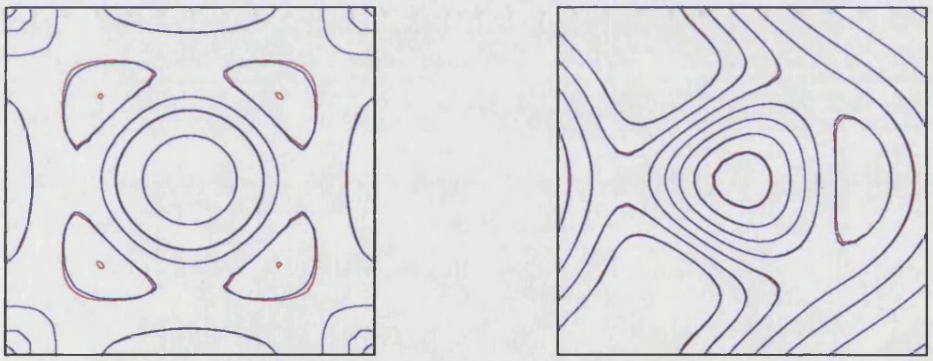

a) Al 0.010 0.020 0.025 0.275 0.030 0.032

b) Si 0.01 0.02 0.03 0.04 0.05 0.06 0.07

original pseudo, reconstructed pseudo

Figure 5.7: Contours of constant valence charge density on planes shown in figure 5.5 - contour levels are shown below each figure in $e\ au^{-3}$.

Figure 5.7 shows contour plots of $\rho(\mathbf{r})$ for both Al and Si, in order to visually demonstrate the quality of the reproduction of the charge density - the planes through the unit cell are as shown in figure 5.5. There is good agreement between the original and reconstructed densities for both Al and Si, with very little distinguishable difference between these contour plots.

5.3.3 Original Pseudo and Reconstructed DOS

Now we return to the reconstruction of the correct core and valence states from the original pseudopotential calculation. A useful check on the success of the reconstruction is a comparison of the Density of States of the original and reconstructed systems. Since there is a 1 : 1 correspondence between the all-electron valence and pseudo states, the eigenvalues are equal and the pseudopotential is norm conserving (see chapter 3), then a successful reconstruction will yield an identical DOS to the original results.

The DOS within r_s is calculated from the CASTEP results by applying the tetrahedron method (see chapter 3) to obtain the LDOS, and integrating this over the volume contained by the embedding sphere[1]. For the reconstructed DOS a self consistent calculation is carried out (as described earlier in this chapter), and the embedded Green function obtained along a contour parallel to the real axis, with an imaginary energy of 0.1 eV. The LDOS is taken from the imaginary part of this Green function, and integrated over the volume of the embedding sphere, hence the reconstructed DOS is smoothed by a Lorentzian of width 0.1 eV, small enough for the fine structure to be apparent.

In figure 5.8 the DOS within the embedding sphere is shown, for pseudo and reconstructed states. For Al agreement is good, with an error of $\sim$ 1 %. For Silicon the agreement is worse, with reconstructed states shifted up in energy by up to $\sim$ 0.3 eV.

Overall the agreement is fair, and it should be remembered that the total DOS (over the entire unit cell) includes the contribution from the states outside of the embedding sphere, so these errors become less important when the total DOS is considered.

[1]This is carried out by converting the reciprocal space expansion of the charge density into a spherical harmonic expansion (see chapter 3 for a similar conversion for the Bloch states) so the integration over the embedding sphere can be carried out analytically and reduced to a sum.

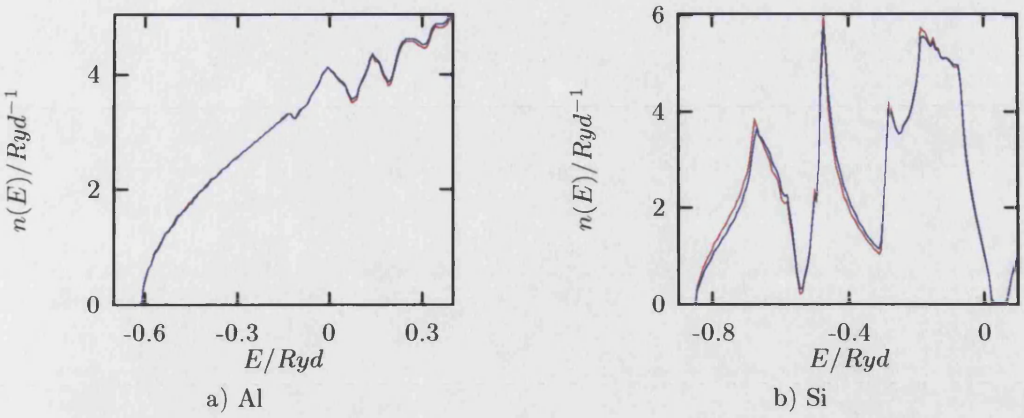

Figure 5.8: Reconstructed (——) and original (– – –) DOS within the embedding sphere.

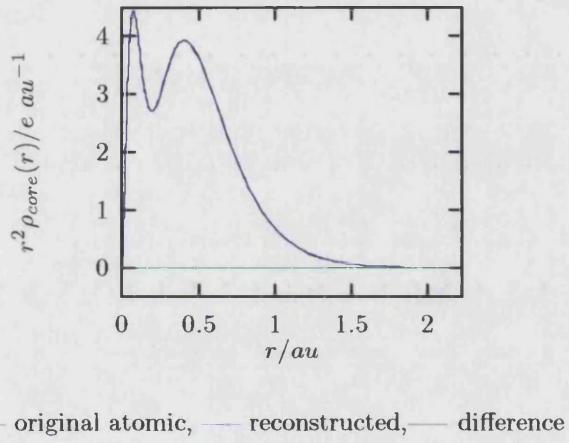

Figure 5.9: Silicon core charge density from reconstruction and atomic calculation used to construct pseudopotential.

5.3.4 Core States

Unfortunately we cannot compare the core states directly with the original pseudopotential calculation, as none are explicitly present. However, we can compare the core states from the reconstruction with the core states of the atomic calculation that produced the original pseudopotential. If the frozen core approximation is valid there will be negligible difference between the two. If a difference was apparent this could be attributed to either genuine core relaxation or inaccuracies in the reconstruction. Figure 5.9 shows the core electron charge density for the reconstructed calculation and the atomic calculation that yielded the original pseudopotential, together with the residue $\rho^{recon}(r) - \rho^{atom}(r)$ for Si. Agreement is good, with a maximum difference of ~ 0.2 % near the origin. It is difficult to

identify the cause of this discrepancy with any confidence since the original atomic states used to construct the pseudopotential are not calculated fully relativistically, whereas the core states within the reconstruction are, hence no effort is made here to assess the likelihood of core relaxation being the cause.

5.3.5 Is an aspherical calculation necessary?

So far no justification has been given for the additional complexity and effort required to implement this method in a form that does not require spherical symmetry of either the charge density or self consistent potential. The first question to answer is what error is introduced by only considering the s part of the charge density? Taking ρ_{00}^{val} from a fully converged aspherical reconstruction and comparing this with the original CASTEP charge density gives the peak errors and R values shown in Table 5.8, where it is apparent that the $l > 0$ parts of the charge density are important.

Figure 5.10 shows a surface of constant charge density for both Al and Si. The cube encasing the figures just contains the embedding sphere, and the charge density outside of the sphere is taken from the original pseudopotential calculation. These figures graphically illustrate the importance of the asphericity of the charge density, with the bonding in Silicon particular clear.

Although this demonstrates that asphericity is important, it should be mentioned that good results for the spherical part of the charge density can be obtained by carrying out a reconstruction with only the spherical parts of the charge density and self-consistent potential included *provided the embedding potential is the correct aspherical potential.* This is also true if other l values are included in the reconstruction. In other words if only the $l = 2$ component of the charge density is required (eg for EFG calculations), then only the $l = 0, 2$ components of the self consistent potential and charge density need be included to obtain good results.

	Error in $\rho(\mathbf{r})$ within r_s	
	peak ($e\ au^{-3}$)	$R(\%)$
Al	57.85×10^{-4}	7.05
Si	404.63×10^{-4}	27.50

Table 5.8: Errors in ignoring aspherical part of ρ.

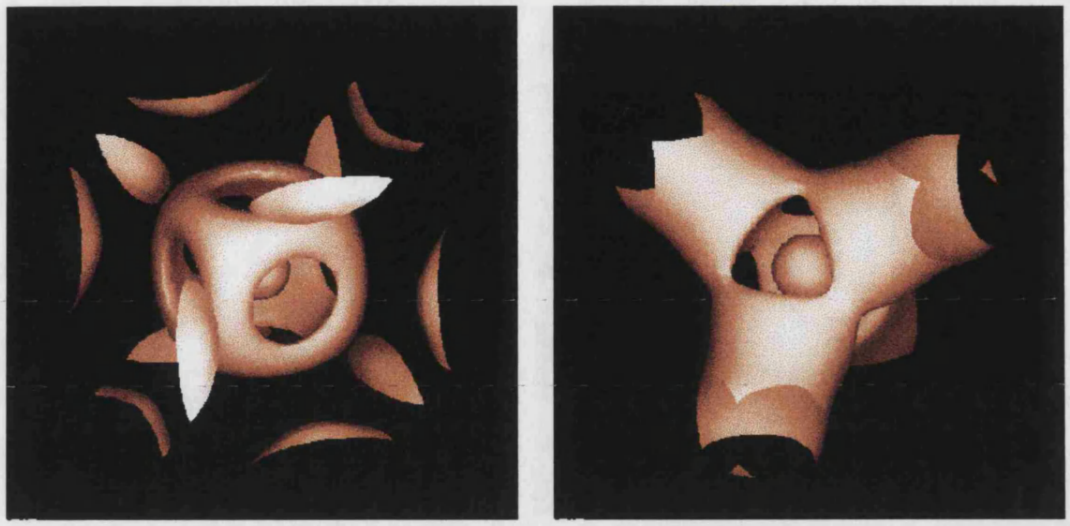

a) Al - $\rho^{val}(\mathbf{r}) = 0.031\ e\ au^{-3}$ b) Si - $\rho^{val}(\mathbf{r}) = 0.055\ e\ au^{-3}$

Figure 5.10: Charge density isosurfaces from reconstruction calculations.

5.4 Convergence

In this section the convergence properties of the reconstructed charge density are examined. All of the parameters examined in chapter 4 are investigated to ensure that the embedding potential is sufficiently well converged for the reconstruction calculation to be accurate. Parameters investigated are:

- E_{max}, the energy cut off of the plane wave basis set used for the original CASTEP matrix diagonalisation.
- $n_{\mathbf{k}}$, the number of $\mathbf{k}$ points used for the Brillouin zone integral.
- The energy grid used to perform the convolution integral that gives $\mathcal{G}$, the surface Green function, in terms of $\mathcal{F}$, the spectral function.
- l_{max}, the maximum l value to which Γ is expanded - the size of the embedding potential matrix (this gives a charge density and self-consistent potential with terms $l \leq 2l_{max}$, see section 5.2).
- n_{bands}, the number of bands included in the spectral representation of the Green function (before 'topping up' with free space).

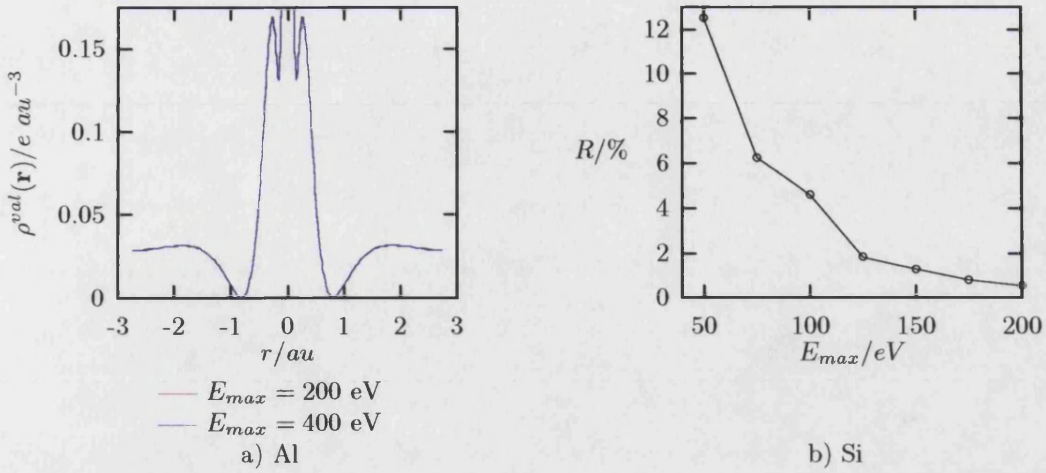

Figure 5.11: Convergence of $\rho(\mathbf{r})$ with E_{max}.

5.4.1 Energy Cutoff

Embedding potentials were constructed for Aluminium, using the 'standard' parameters given in section 5.3.1, but with E_{max} values ranging from 100 to 400 eV. Figure 5.11a shows the reconstructed valence charge density sampled along a line in the {110} direction with an atomic site at the origin. Results for 200 and 400 eV cutoff are shown in the figure, and there is no distinguishable difference. This is supported by the R-factors - for cutoffs of 200 and 400 eV, R takes the values 0.6 and 0.4 % respectively. The results for Silicon are much the same, but the percentage error is slightly smaller - for $E_{max} = 200$ eV, $R = 0.53$ %.

Figure 5.11b shows the R-factor for Silicon for a range of cutoffs up to 200 eV. The valence charge within the embedding sphere shows similar variation with E_{max} - errors of ~ 5 % for 100 eV and ~ 0.1 % for 200 eV. These results suggest that a cutoff of 200 eV gives good results for both Al and Si, and that accuracy may be increased minimally by increasing E_{max}.

The errors considered here are for the charge density expanded with all components. If only the well converged components (see Table 5.5) are compared the error is still decreased only minimally - for Al increasing the cutoff from 200 to 400 eV decreases R from 0.19 to 0.17 %.

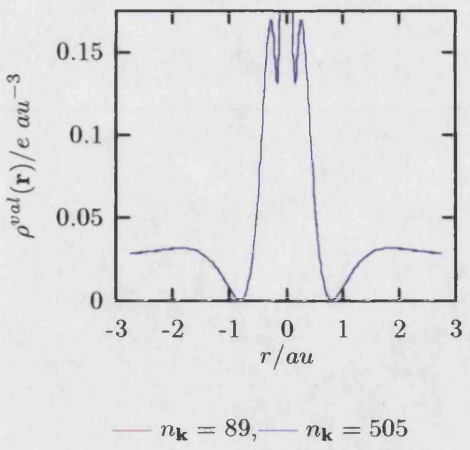

Figure 5.12: Convergence of $\rho^{val}(\mathbf{r})$ with $n_{\mathbf{k}}$ for Al.

5.4.2 Brillouin Zone Integral

Different sized **k** point sets were used for the Brillouin zone integration method described in chapter 3, and reconstruction calculations performed with the resulting embedding potentials.

In figure 5.12 the valence charge density for Al is given, again along {110} through an atomic site. Results are shown for $n_{\mathbf{k}} = 89$ and 505 (240 is the value used for all other results in this chapter), and no discernable difference between the two is apparent.

Table 5.9 gives the valence charge within r_s, q, for Aluminium, and the R values for 4 different **k** point sets. The error is minimal for more than 20 **k** points, and the charge within the sphere agrees with the reconstruction to within 0.5 % for more than 20 points in the set.

$n_{\mathbf{k}}$	$q(e)$	peak($\times 10^{-4} e\ au^{-3}$)	$R(\%)$
20	2.3314	−22.69	2.30
89	2.3030	−6.32	0.47
240	2.3011	5.23	0.44
505	2.3000	5.46	0.45
Pseud.	2.2981	-	-

Table 5.9: Errors in ρ for different **k** point sets used to calculate embedding potential - Aluminium.

This is a surprising result given the problems with convergence of the Brillouin zone integral encountered in chapter 3, and is likely to be due to the fact that the charge density takes the form of an integral of the LDOS over occupied states. Any errors in the Brillouin zone integrals performed using linear interpolation cause states to be placed at a slightly incorrect energy (see the DOS in section 5.3.3), so the states are not lost and are still included as occupied states (unless shifted above the Fermi energy). This would ensure that band crossing and inadequate representation of van Hove singularities has negligible effect on the charge density resulting from the reconstruction.

If only the well converged components (see Table 5.5) are compared the error is still decreased only minimally- for Al increasing the number of $\mathbf{k}$ points from 240 to 505 decreases R from 0.19 to 0.18 %.

5.4.3 The Convolution Integral

A particularly computationally expensive part of the reconstruction procedure is the calculation of the embedding potential itself - the time taken to obtain this is dominated by deriving the spectral function $\mathcal{F}$ from the pseudo-states.

In view of this it is desirable to investigate the sampling resolution required in order to carry out a reconstruction calculation of sufficient accuracy. In this section core reconstruction calculations are presented as in the previous sections, with the embedding potential calculated using a range of sampling resolutions for the spectral function.

Sampling interval - ΔE

Figure 5.13 shows the errors in the charge density resulting from a spectral function sampling interval, ΔE, taking a number of values. The R-factor is given as a function of ΔE for both Al and Si.

For Aluminium no increase in accuracy is achieved for $\Delta E < 0.5$ eV, and the errors are still fairly low ($R < 1$ %) up to $\Delta E = 1.4$ eV. Silicon shows a marked increase in error for $\Delta \geq 0.5$ eV, with very little change in error below this value.

Aluminium converges with decreasing ΔE far quicker than Silicon due to the fine

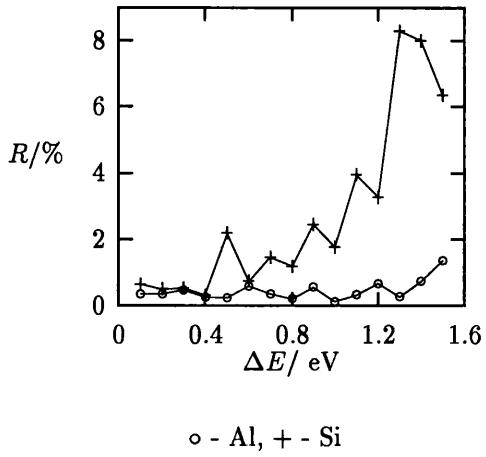

Figure 5.13: Convergence with sampling of spectral function, $\mathcal{F}$. The R-factor is shown for Al and Si and $\Delta E = 0.1 - 1.5$ eV.

structure present in the Silicon band structure. This leads to high resolution features in the density of states (for example the sharp peak at ~ -0.5 Ryd shown in figure 5.8), so the spectral function requires finer sampling to be described accurately. Aluminium has a much smoother distribution of states, so coarser sampling is adequate.

Variation of Sampling with Energy

As described in chapter 4, the fine structure of the Green function over a given energy range is entirely due to the fine structure of the spectral function within that range. The spectral function outside of this range of interest contributes only a slowly varying part to the Green function (within the range of interest). This contribution is an *average* of the spectral function outside of this limited range as given by convolution integral discussed in chapter 4.

This suggests that a further improvement in the efficiency of sampling used for the spectral function can be achieved by dividing the energy range of the spectral function into two regions. The first of these regions is the low energy range, where we are interested in the fine structure of the Green function - in this case from the bottom of the lowest energy band to just above the Fermi energy. The second region is from the top of the first region to the top of the highest energy band. The first region is sampled at a fine resolution, ΔE_1, in order to represent the fine structure, and the second region sampled more coarsely at intervals of ΔE_2.

For the present calculation, region 1 is taken as from the bottom of the lowest band to 5 eV (E_f for Al and Si are 2.816 eV and 0.324 eV respectively) and region 2 taken as from 5 eV to the top of the highest band ($\sim$ 250 eV). In region one $\Delta E_1 = 0.1$ eV, and a range of values are chosen for ΔE_2.

Table 5.10 shows the values of ΔE_2 used and the corresponding number of $\mathcal{F}$ energy sample points. All of the reconstruction results presented so far have employed linear interpolation for the evaluation of the convolution integral. Cubic interpolation (see chapter 3) was also used to perform the convolution integral with the current sample scheme, and results for this are presented here.

Figure 5.14 shows the R-factor of the valence charge density for different ΔE_2. In figure 5.14a the error is given for Al, with both linear and cubic interpolation. Below $\Delta E_2 = 2.0$ eV no decrease in error is achieved by employing a finer sampling interval, hence the reconstruction can be considered to be converged. There is a low R at 1.5 eV which is probably spurious. Across the whole range of ΔE_2 the cubic interpolation gives lower errors than linear interpolation, but within the useful range of low error ($\Delta E_2 \leq 2$ eV) the difference between linear and cubic interpolation is minimal.

Figure 5.14b shows the error for Si, again with both linear and cubic interpolation. A higher resolution is required than for Al, and cubic interpolation gives *worse* results than linear interpolation. This is as expected from the discussion of embedding potential convergence in chapter 4. Linear interpolation appears to

	No. samples	
ΔE_2/ eV	Al	Si
0.1	2878	2569
0.5	694	649
1.0	421	409
1.5	331	331
2.0	286	289
2.5	259	265
5.0	205	217
7.5	187	202
10.0	178	193
15.0	169	187
20.0	163	181

Table 5.10: Number of $\mathcal{F}$ sample points ($\Delta E_1 = 0.1$ eV).

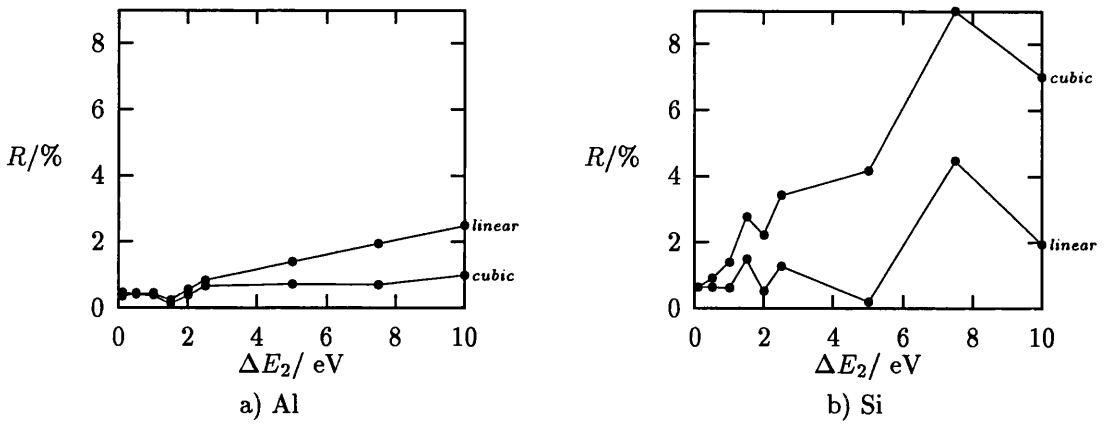

Figure 5.14: Convergence with sampling of spectral function, $\mathcal{F}$, in region 2 (see text). $\Delta E_2 = 0.1 - 10$ eV, and $\Delta E_1 = 0.1$ eV.

give a converged charge density for $\Delta E_2 \leq 1$ eV, whereas the results from cubic interpolation only agree with the linear results at $\Delta E_2 = 0.1$ eV.

In summary, these results suggest that a spectral function sampling of 0.1 eV below 5 eV, and 1 eV above will give a converged reconstruction for a linear interpolation scheme. This reduces the required number of sample points (and so the time and memory requirements) by a factor of ~ 7.

5.4.4 Size of Embedding Potential Matrix

Another important factor in the convergence of the reconstruction calculation is the number of spherical harmonics included in the basis used for the embedding potential (and also used for the basis of the reconstruction calculation itself), l_{max}. The value of l_{max} chosen can effect the results of the reconstruction in three distinct ways, discussed below.

Convergence of Γ

The embedding potential, Γ, requires the inversion of the Green function over the embedding surface. For a matrix representation of Γ and the Green function this requires knowledge of the *entire* surface Green function matrix, and the inversion of this matrix, as discussed in chapter 4. In chapter 4 it was concluded that for $l_{max} \geq 3$ the elements of the embedding matrix are converged with respect to l_{max} (those elements present, at least).

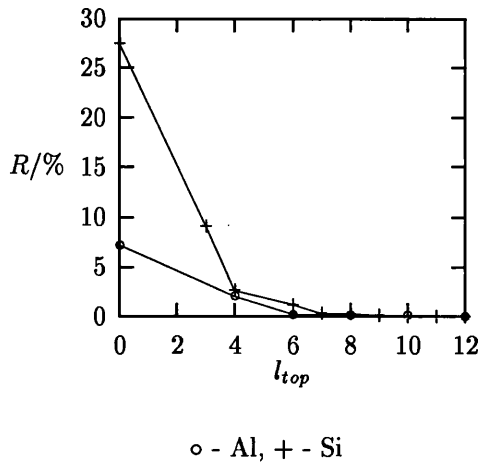

Figure 5.15: R-factor for charge density including terms up to l_{top} only. The R-factor is calculated by comparing this expansion and the real space charge density.

This was also found to be the case for the resultant reconstructions - a reconstruction carried out using $l_{max} = 3$ was found to be indistinguishable from a reconstruction using only the $l, l' \leq 3$ sub-matrix of an embedding potential calculated using $l_{max} = 6$.

Convergence of the valence charge density

The valence charge density, $\rho^{val}(\mathbf{r})$, can be derived from the imaginary part of the Green function, as described in section 5.2. In view of this it is reasonable to require l_{max} to be large enough to accurately describe the $\rho^{val}(\mathbf{r})$ for the system.

If the basis set for the Green function includes only $l \leq l_{max}$ then the charge density will be non zero for $l \leq 2l_{max}$ (see section 5.2). Figure 5.15 shows the R-factor of the original pseudo charge density expanded to contain only $l \leq l_{top}$ components, compared with same charge density expanded with all terms up to $l = 12$. For both Al and Si $R < 0.3$ % for $l_{top} \geq 8$, corresponding to $l_{max} = 4$. This suggests that $l_{max} = 4$ should provide enough terms to describe $\rho^{val}(\mathbf{r})$ accurately.

Further justification for this can be given by examining the contribution to the LDOS integrated over the embedding sphere from the Green function in the reconstruction calculation. The integral of the LDOS over the embedding sphere depends only on the $L = L'$ elements of the Green function matrix, and the contribution from the diagonal elements corresponding to each l value is shown in figure 5.16, for Al and Si. The contribution from matrix elements $l, l' > 3$ is negligible

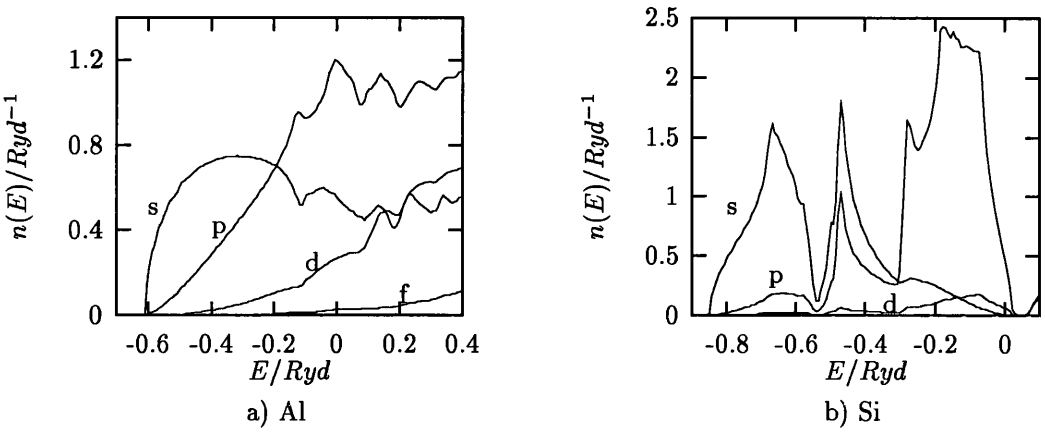

Figure 5.16: Contributions to DOS within r_s from different diagonal parts of the Green function matrix. s denotes the contribution from the $(0m, 0m)$ elements, p from the $(1m, 1m)$ etc.

for both Al and Si.

It should be noted that although this means sufficient components of the spherical harmonic expansion of $\rho^{val}(\mathbf{r})$ are present to describe it accurately, these components may not be converged for $l_{max} = 4$. Similarly, although the Green function matrix is large enough to describe the DOS for $l_{max} = 4$, the matrix elements may not have converged with l_{max} for this size of matrix.

Convergence of the reconstruction calculation

The greatest influence that the l_{max} value chosen has upon the results of the reconstruction is in the completeness of the basis set used in the reconstruction calculation itself. A large enough value must be chosen for the Green function within the reconstruction calculation to be converged, and so to provide an accurate valence charge density.

Figure 5.17a shows the R-factor for Al and Si with $l_{max} = 1 \ldots 9$. For $l_{max} \leq 3$ the error is largely due to insufficient components of the charge density being present to describe it accurately. Even when l_{max} is large enough for the required components to be present a significant error is observed. This is due to the higher l components of the charge density not being converged. To illustrate this figure 5.17b shows the $(lm) = (40)$ component of the charge density for Si, reconstructed with $l_{max} = 2, 4, 6$ together with the original pseudo-density. It is apparent that this is not converged until $l_{max} = 6$. The convergence of the higher l ($l > 4$)

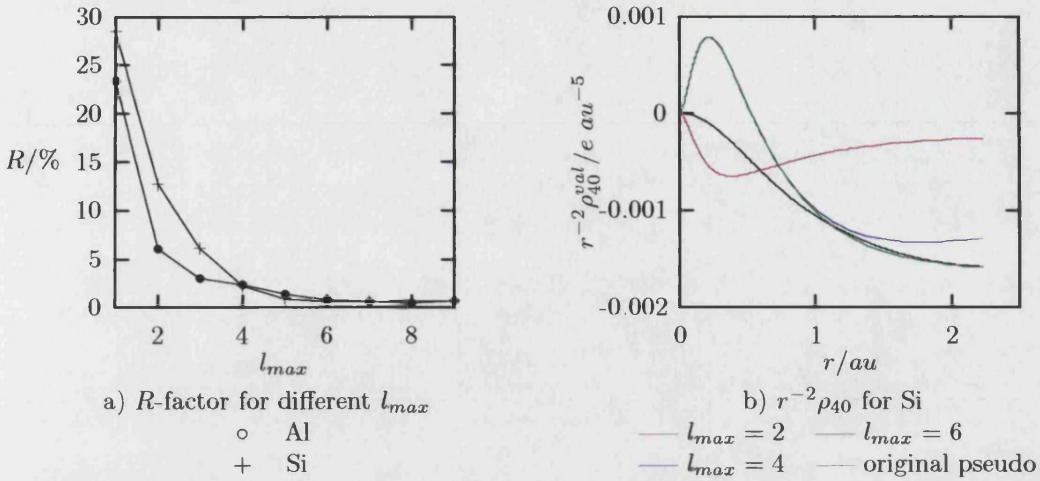

a) R-factor for different l_{max}
○ Al
\+ Si

b) $r^{-2}\rho_{40}$ for Si
$l_{max} = 2$ $l_{max} = 6$
$l_{max} = 4$ original pseudo

Figure 5.17: Convergence with l_{max}.

components of the charge density is slower, and the lack of convergence of the $l = 6$ component contributes a significant error to the charge densities calculated with $l_{max} = 6$ for both Al and Si (see Table 5.5).

In summary, for $l_{max} < 4$ the error in the charge density is due to non-spherical parts of the charge density being absent, and for $l_{max} \geq 4$ the error is due to non-spherical parts of the charge density being incorrect.

5.4.5 Effect of Including Only Low Energy Bands in Γ

As mentioned before the most computationally expensive part of the reconstruction procedure is the construction of the spectral function, $\mathcal{F}$, both from the viewpoint of obtaining the pseudo-states, and calculating the spectral function from these states. In chapter 4 the contribution of the unoccupied bands to the Green function and embedding potential was discussed, and embedding potentials calculated using only a low energy subset of the bands.

If a significantly lower number of bands could be used than the full set given by direct matrix diagonalisation (in the pseudopotential total energy calculation), then this would give two advantages. Firstly the spectral function $\mathcal{F}$ would require evaluation at fewer sampling points, and secondly the low energy pseudo-states could be obtained by efficient iterative methods avoiding the diagonalisation of a matrix.

In order to investigate this, reconstruction calculations are performed using the

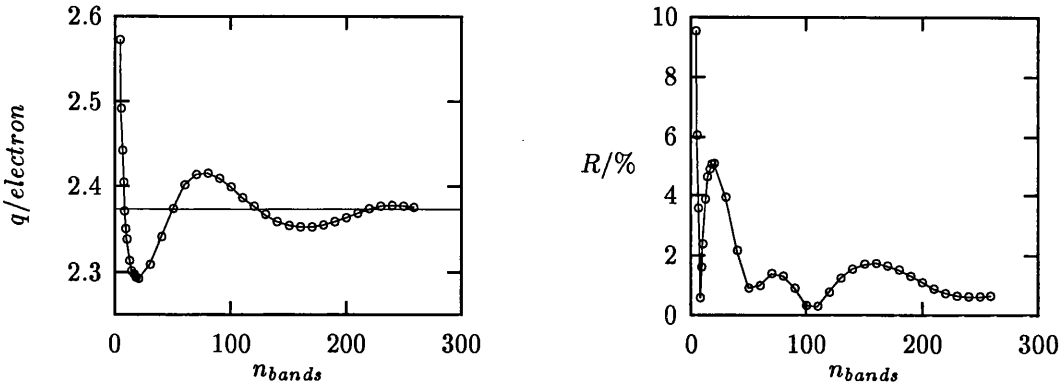

a) total charge b) R-factor

Figure 5.18: Convergence with n_{bands} for Si.

embedding potential derived from the lowest n_{bands} bands (see chapter 4). Figure 5.18a gives the resulting q for Si as a function of n_{bands}, with n_{bands} ranging from 4 (the number of occupied bands) to 259 (total number of bands available). This is clearly not converged until virtually all of the bands are included.

Figure 5.18b shows the R-factor for each n_{bands}, again for Si. The error in the charge density shows the same oscillatory behaviour as q, eventually converging to a stable value of $\sim$ 0.8 % for all bands included.

It is clear that an accurate reconstruction cannot be performed using a subset of the bands of the system - with the present method of obtaining the embedding potential all the unoccupied bands are required to give an accurate embedding calculation. However the errors introduced by using a subset of the available bands are oscillatory with accurate q values and minima in the error, R, present for small n_{bands}. This suggests that it may be possible to find an underlying cause for this oscillatory effect and take it into account to provide a more efficient scheme to derive the embedding potential.

5.5 Silicon Structure Factors

Extremely accurate measured structure factors for Silicon have been available in the literature for some time (Cumming and Hart, 1988; Aldred and Hart, 1973; Teworte and Bonse, 1984; Saka and Kato, 1986). These results have been used by a number of workers to assess the accuracy of parameterised models (Deutsch, 1992), FLAPW and other *ab initio* methods (Lu et al, 1993) and generalisations of the LDA exchange-correlation potential (Zuo et al, 1997).

In view of the accuracy and range of data available, both experimental and theoretical, the reconstructed Silicon charge densities are here used to construct structure factors for comparison with experimental data and the results of state of the art FLAPW calculations.

5.5.1 Structure Factors from Charge Densities

To obtain the structure factors we require the charge density expanded in the usual plane wave basis set,

$$\rho_{total}(\mathbf{g}) = \frac{1}{V_\Omega}\int_\Omega \rho_{total}(\mathbf{r})e^{-i\mathbf{g}.\mathbf{r}}d^3\mathbf{r} \tag{5.24}$$

where V_Ω denotes the unit cell volume and $\rho_{total}(\mathbf{r})$ is the real space total charge density.

The real space charge density within the integral in equation (5.24) consists of the original pseudo charge density between atoms, and the reconstructed charge density (including the core contribution) within the embedding sphere surrounding atoms. Since this integral is a linear operation on the charge density it is possible to subtract the contribution to the pseudo density from the embedding regions around each atom and add on the contributions from a reconstruction calculation. This gives the expression

$$\rho_{total}(\mathbf{g}) = \rho_{pseudo}(\mathbf{g}) + \frac{1}{V_\Omega}\sum_i \left[\alpha^{recon}_{\mathbf{s}_i} - \alpha^{pseudo}_{\mathbf{s}_i}\right] \tag{5.25}$$

where $\mathbf{s}_i$ are the positions vectors of the atoms in the unit cell. The quantities α^{recon} and α^{pseudo} are the Fourier integrals of the reconstructed and pseudo densities respectively, carried out over the reconstruction sphere surrounding each atom,

and are given by

$$\alpha_{\mathbf{s}_i} = \int_{|\mathbf{r}-\mathbf{s}_i|<r_s} \rho(\mathbf{r}) e^{-i\mathbf{g}.\mathbf{r}} d^3\mathbf{r} \tag{5.26}$$

where $\rho(\mathbf{r})$ is the appropriate charge density, reconstructed or pseudo. Since the original pseudo charge densities are available in reciprocal space directly from the CASTEP calculations, and the reconstructed charge densities available expanded in spherical harmonics, equations (5.25) and (5.26) can be evaluated.

For an atom situated at the origin equation (5.26) takes the form

$$\alpha_0 = 4\pi \sum_L (-i)^l Y_L(\hat{\mathbf{g}}) \int_0^{r_s} \rho_L(r) j_l(gr) r^2 dr \tag{5.27}$$

where the charge density has been explicitly written as an expansion in spherical harmonics, and the identity given in equation (3.20) has been used. The radial integral is carried out by interpolating the available $\rho_L(r)$ values and integrating the product of this interpolating function and the Bessel function analytically. Linear interpolation is sufficient for the logarithmic radial grids employed in the reconstruction.

Other atoms within the unit cell

The integral in equation (5.27) is carried out over a sphere centred at a corner of the unit cell, but the charge density within the segments of the sphere that fall outside of the unit cell are repeated at corners of the unit cell due to periodicity of the lattice, hence the contribution from this atom is calculated correctly.

Other atoms within the unit cell must also be taken into account. In the case of Silicon there is another atom at $\left(\frac{1}{4}, \frac{1}{4}, \frac{1}{4}\right)$ related to the origin by an inversion symmetry at $\left(\frac{1}{8}, \frac{1}{8}, \frac{1}{8}\right)$. The contribution to equation (5.25) from this atom can be derived from the symmetry of the unit cell. If the atom at the origin is related to an atom at site $\mathbf{s}$ by the space group operator $\{P|\mathbf{s}\}$ (see chapter 3) then the integral for the atom at $\mathbf{s}$, $\alpha_\mathbf{s}$, will be given by

$$\alpha_\mathbf{s} = \int_{|\{P|\mathbf{s}\}^{-1}\mathbf{r}|<r_s} \{P|\mathbf{s}\}^{-1} \rho(\mathbf{r}) e^{-i\mathbf{g}.\mathbf{r}} d^3\mathbf{r}. \tag{5.28}$$

By transforming coordinates this reduces to

$$\alpha_\mathbf{s} = \int_{|r|<r_s} \rho(P^{-1}\mathbf{r}) e^{-i\mathbf{g}.(\mathbf{r}+\mathbf{s})} d^3\mathbf{r}. \tag{5.29}$$

For Silicon the atom at $\left(\frac{1}{4},\frac{1}{4},\frac{1}{4}\right)$ is related to the atom at the origin by the operator $\left\{-I|\left(\frac{1}{4},\frac{1}{4},\frac{1}{4}\right)\right\}$, an inversion followed by a translation. In this case the above expression together with the expansion around the origin in spherical harmonics yields

$$\alpha_{\mathbf{s}} = 4\pi e^{-i\mathbf{g}.\mathbf{s}} \sum_{L} (-1)^{l}(-i)^{l} Y_L(\hat{\mathbf{g}}) \int_0^{r_s} \rho_L(r) j_l(gr) r^2 dr \tag{5.30}$$

where $\mathbf{s} = \left(\frac{1}{4},\frac{1}{4},\frac{1}{4}\right)$. The transformation results in the phase factor, and the inversion results in the power of (-1) present in the sum.

Equations (5.27) and (5.30) are applied to both the reconstructed charge density and the pseudo density (expanded in spherical harmonics) and then substituted into equation (5.25) to yield the structure factor as a function of the reciprocal lattice vector, $\mathbf{g}$. At first it seems a roundabout route to calculate the radial expansion of the pseudo density only to convert this back to a reciprocal space representation, but this is the most straightforward way of replacing the pseudo charge density with the reconstructed charge density in the sphere around each atom.

Shifting the origin

One final point is the position of the origin. The coordinate system used for Si throughout this work is centred on one of the Silicon atoms in the unit cell (at $\bar{4}3m$), whereas the system normally chosen for crystallographic studies is centred at the inversion centre, $(\bar{3}m)$ (see Hahn, 1995). Placing the origin at the inversion centre has the particular advantage that the structure factors are real. This can easily be taken into account by transforming the spatial variable in the Fourier representation (equation 5.24) introducing an additional phase factor, so that

$$\rho(\mathbf{g})^{\mathrm{O\ at\ } \bar{3}m} = \frac{1}{\sqrt{2}}(1+i)^{h+k+l} \rho(\mathbf{g})^{\mathrm{O\ at\ } \bar{4}3m} \tag{5.31}$$

is the required structure factor, and (hkl) are the indices for the cubic reciprocal lattice vectors for Silicon, $\mathbf{g} = \frac{2\pi}{a_0}(h\mathbf{i} + k\mathbf{j} + l\mathbf{k})$.

5.5.2 Comparison with Experimental Results and FLAPW Calculations

Before comparison can be made between the theoretical and experimental results two further factors must be taken into account. Firstly, the experimentally measured quantity (normally given in the literature) is not the Fourier coefficient of the charge density, $\rho(\mathbf{g})$, but the form factor f_{hkl}, which takes into account the lattice structure. This is defined as (Zuo et al, 1997)

$$f_{hkl} = \rho_{total}(\mathbf{g}) / \cos\left((h+k+l)\frac{\pi}{4}\right) \tag{5.32}$$

where (hkl) are the indices of the reciprocal lattice vector. For (hkl) values that satisfy the criteria $h+k+l = 4n+2$ for n integer, the denominator on the RHS is zero. For a lattice of spherically symmetric charge densities the ρ values at these $\mathbf{g}$ points would be zero, but for a real lattice this is not the case. For these $\mathbf{g}$ points the denominator is generally taken to be unity and the structure factor given.

Another important effect that must be taken into account when correlating the theoretical and experimental results is that of thermal motion of the lattice. The majority of experimental data for structure factors is taken at room temperature, and the thermal energy 'smears out' the charge density, reducing the amplitude of the higher order structure factors. This can be described by a convolution integral in real space, which corresponds to a further correction factor in reciprocal space to give the *dynamic structure factor*

$$f_{hkl}^{dyn} = f_{hkl} e^{-Bg^2/16\pi^2} \tag{5.33}$$

where B is the Debye-Waller parameter (Lu et al, 1993; Deutsch, 1992; Zuo et al, 1997). This parameter is often treated as a free variable to optimise the fit between theoretical and experimental values.

Structure factors obtained from the core reconstruction are here compared with those obtained from three sources:

- Structure factors obtained from the simple addition of atomic core states to the original pseudo charge density.
- Structure factors obtained using the FLAPW method by Zuo et al (1997).

- Structure factors determined experimentally by Cumming and Hart (1988) and Saka and Kato (1986), as given by Zuo et al (1997).

The pseudo+core structure factors are obtained from the charge density of the original pseudopotential calculation together with the core charge densities of the original atomic calculations used to create the pseudopotential. The contribution from the atomic core charge density was included at the atomic sites in the same manner as described above, ie

$$\rho_{total}(\mathbf{g}) = \rho_{pseudo}(\mathbf{g}) + \frac{1}{V_\Omega}\sum_i \alpha_{\mathbf{s}_i}^{core} \tag{5.34}$$

where $\alpha_{\mathbf{s}_i}^{core}$ is the contribution from the core states at site $\mathbf{s}_i$. This structure factor is expected to show significant error, since the valence charge density will be entirely incorrect close to atomic sites.

Zuo et al (1997) calculated Si structure factors using the FLAPW method, an all-electron method based on density functional theory. The method makes the same *physical* approximation as the reconstruction method described here, and they produce results using the Local Density Approximation (LDA), and two different Generalised Gradient Approximations (GGA).

Since the core reconstruction calculation carried out here employs the LDA the reconstruction results are only compared with the LDA FLAPW results given by Zuo. For a successful reconstruction scheme we would expect to accurately reproduce these results, since the same physical approximations have been made even though the algorithmic implementation of the two methods are entirely different.

The experimental data obtained by Cumming and Hart, and Saka and Kato is taken from the paper by Zuo, where they use this data to assess the accuracy of the FLAPW calculations (and several other less exact methods). Here the same data is used to assess the accuracy of the reconstructed, FLAPW and pseudo+core structure factors.

5.5.3 Static Structure Factors

Table 5.11 gives the form factors resulting from the three calculation methods (reconstruction, Zuo et al FLAPW (with LDA) and pseudo-states plus free atom core

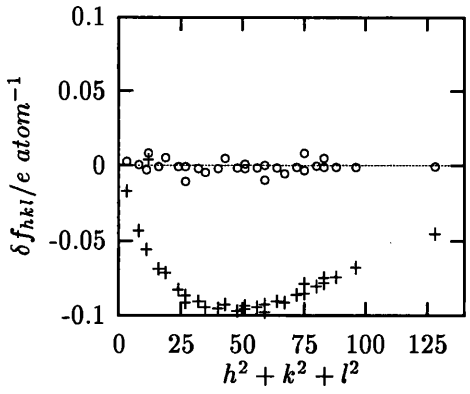

Figure 5.19: Difference between static form factors calculated by reconstruction and FLAPW methods, and the difference between static form factors calculated by pseudo+core and FLAPW methods.

states) with no temperature correction. Only the (hkl) values for which experimental data was available are considered (see Table 5.12). Figure 5.19 shows the differences between the reconstructed and FLAPW form factors, and the difference between the pseudo+core and FLAPW form factors. It is apparent that the reconstruction agrees well with the FLAPW results - the average absolute difference for the reconstructed results is only 3 milli-electrons/atom whereas for the pseudo+core result the average absolute difference is over 25 times greater at 76 milli-electrons/atom.

5.5.4 Experimental, FLAPW and Reconstructed Structure Factors

In order to compare the static structure factors given above with the experimental data a value for the Debye-Waller parameter in equation (5.33) is required. This is commonly taken to be a free parameter and varied to minimise the error between the experimental and theoretical results. The value of B used here is that employed by Zuo in comparisons with experimental data, a value of $B = 0.4668\mathring{A}^2$. In this paper values of B are obtained by minimising the error of high $|\mathbf{g}|$ values only, for a number of different *ab initio* methods. These high $|\mathbf{g}|$ structure factors depend almost entirely on the core states of the atoms that make up the lattice, so the best values should result from methods that most accurately describe the core states. A calculation of these high order structure factors using the Multi Configuration

	$f_{hkl}/e\ atom^{-1}$		
(hkl)	Reconstruction	FLAPW	Pseudopotential
1 1 1	10.7286	10.7261	10.7088
2 2 0	8.6656	8.6653	8.6218
3 1 1	8.0300	8.0331	7.9772
2 2 2	0.1777	0.1693	0.1730
4 0 0	7.4495	7.4505	7.3816
3 3 1	7.2320	7.2266	7.1549
4 2 2	6.6957	6.6965	6.6138
3 3 3	6.3936	6.4043	6.3130
5 1 1	6.4267	6.4276	6.3411
4 4 0	6.0291	6.0311	5.9406
5 3 1	5.7943	5.7992	5.7050
6 2 0	5.4526	5.4548	5.3595
5 3 3	5.2738	5.2690	5.1762
4 4 4	4.9662	4.9681	4.8713
7 1 1	4.7984	4.8003	4.7048
5 5 1	4.8036	4.8027	4.7089
6 4 2	4.5449	4.5466	4.4522
7 3 1	4.4040	4.4041	4.3114
5 5 3	4.3960	4.4059	4.3080
8 0 0	4.1815	4.1831	4.0924
7 3 3	4.0560	4.0615	3.9700
8 2 2	3.8690	3.8702	3.7839
6 6 0	3.8688	3.8702	3.7841
5 5 5	3.7687	3.7606	3.6817
7 5 1	3.7611	3.7645	3.6791
8 4 0	3.5981	3.5986	3.5179
9 1 1	3.5045	3.5059	3.4276
7 5 3	3.5090	3.5041	3.4289
6 6 4	3.3608	3.2205	3.2878
8 4 4	3.1544	3.1556	3.0875
8 8 0	2.5501	2.5509	2.5052
R/%	0.06	-	1.55
GOF	3.6	-	1349

Table 5.11: Form factors from reconstruction, FLAPW and pseudopotential calculations.

Dirac-Fock (MCDF) method (Grant et al, 1980) gives the best fit and so the associated B parameter is chosen by Zuo.

It should be noted that a better fit can be obtained between the experimental and theoretical results for a different B value, but this would essentially be using the description of a *physical* effect, the thermal smearing, to adjust for deficiencies in the theory (the LDA for instance).

Table 5.12 gives the experimental data, the reconstructed, FLAPW and Pseudopotential dynamic form factors. The quality of the theoretical data is assessed by two statistics - the R-factor and GOF parameter. The R-factor is given by

$$R = \frac{\sum_i |f_i^{theory} - f_i^{exp}|}{\sum_i |f_i^{exp}|} \tag{5.35}$$

and is the average absolute error as a fraction of the average absolute value. The goodness of fit parameter is given by

$$GOF = \frac{1}{N}\sum_{i=1}^{N}(1/\sigma_i^2)(f_i^{theory} - f_i^{exp})^2 \tag{5.36}$$

where σ_i^2 is the sample variance of the i^{th} form factor. The variance σ_i^2 is taken to be the average of the estimated error for all data points in line with the approach of Zuo, and takes the value $0.0022^2/e^2\ atom^{-2}$.

The R and GOF are shown in Table 5.12 for the three different theoretical calculations. From this data it can see that the reconstruction calculation describes the experimental data as well as the (LDA) FLAPW results given by Zuo et al. For both sets of data the R-factor is 0.24 %, and the GOF is $\sim$ 35 with the GOF for the reconstruction slightly greater than that for the FLAPW.

In terms of actual values of the error, the average absolute error $|f^{theory} - f^{exp}|$ is 10 milli-electrons/atom for both the FLAPW and reconstructions calculations and 70 milli-electrons/atom for the pseudopotential results. The maximum errors fall at $\sim$ 20 milli-electrons/atom for the FLAPW and reconstruction results, and $\sim$ 100 milli-electrons/atom for the pseudo+core results.

Figure 5.20a shows the residual error of the FLAPW results together with the error bars of the experimental data. Figure 5.20b shows the residual error for the reconstruction calculations. The errors are very similar, even to the point of significant correlation existing between the two. This suggests that the errors

	$f_{hkl}^{dyn}/e\ atom^{-1}$			
(hkl)	Experimental	Reconstructed	FLAPW	Pseudopotential
1 1 1	10.6025(29)	10.6020	10.5995	10.5824
2 2 0	8.3881(22)	8.3955	8.3952	8.3531
3 1 1	7.6814(19)	7.6879	7.6909	7.6373
2 2 2	0.1820(10)	0.1695	0.1615	0.1650
4 0 0	6.9958(12)	6.9924	6.9933	6.9287
3 3 1	6.7264(20)	6.7081	6.7031	6.6365
4 2 2	6.1123(22)	6.0890	6.0897	6.0145
3 3 3	5.7806(21)	5.7456	5.7552	5.6732
5 1 1	5.7906(27)	5.7754	5.7761	5.6984
4 4 0	5.3324(20)	5.3119	5.3136	5.2339
5 3 1	5.0655(17)	5.0447	5.0490	4.9670
6 2 0	4.6707(9)	4.6542	4.6561	4.5748
5 3 3	4.4552(11)	4.4485	4.4444	4.3661
4 4 4	4.1239(18)	4.1069	4.1085	4.0285
7 1 1	3.9282(22)	3.9213	3.9229	3.8449
5 5 1	3.9349(34)	3.9255	3.9248	3.8482
6 4 2	3.6558(54)	3.6413	3.6427	3.5671
7 3 1	3.4919(11)	3.4868	3.4869	3.4135
5 5 3	3.5055(14)	3.4805	3.4883	3.4108
8 0 0	3.2485(34)	3.2458	3.2470	3.1766
7 3 3	3.1270(14)	3.1112	3.1154	3.0453
8 2 2	2.9111(15)	2.9096	2.9105	2.8456
6 6 0	2.9143(16)	2.9095	2.9105	2.8458
5 5 5	2.8009(21)	2.8008	2.7947	2.7361
7 5 1	2.8006(25)	2.7951	2.7976	2.7341
8 4 0	2.6200(7)	2.6216	2.6219	2.5631
9 1 1	2.5325(8)	2.5232	2.5242	2.4678
7 5 3	2.5274(29)	2.5264	2.5229	2.4688
6 6 4	2.3677(9)	2.3724	2.3733	2.3208
8 4 4	2.1506(24)	2.1572	2.1581	2.1115
8 8 0	1.5325(26)	1.5365	1.5370	1.5095
R/%	-	0.24	0.24	1.66
GOF	-	37	31	1158

Table 5.12: Dynamic form factors from experiment, reconstruction, FLAPW and Pseudopotential calculation.

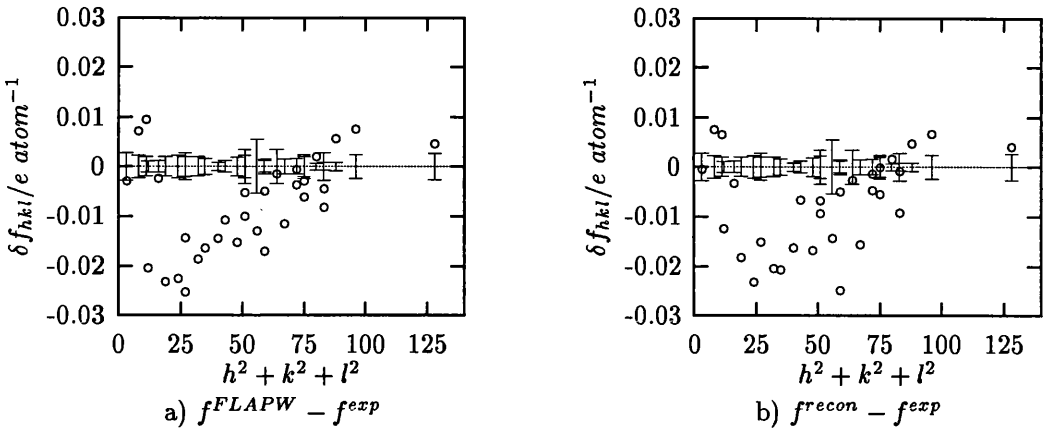

Figure 5.20: Residual error of FLAPW and reconstructed dynamic form factors, with error bars of experimental data shown.

present are largely due to the theory shared by the calculations, specifically the LDA. It should also be noted that the data presented by Zuo is calculated for a lattice constant of $a_0 = 5.4307\mathring{A}$ whereas the reconstruction calculations are carried out for $a_0 = 5.4300\mathring{A}$. This could contribute some of the difference between the results.

A final point is that in Table 5.11 an R-factor and GOF parameter have been calculated comparing the reconstructed and FLAPW results with each other. This shows how good the agreement is, but the GOF parameter of 3.6 indicates that the difference in the results of the two calculations is not quite small enough to be swamped by experimental error.

Introducing spherical symmetry

One of the strengths of the reconstruction method developed here is that it does not require spherical symmetry of the charge density in the reconstruction region near the cores of the atom. By constructing structure factors that include only the spherical part of the charge density within the core region it is possible to assess the importance of the deviations from spherical symmetry to an experimentally measurable quantity.

Figure 5.21 gives the residual error of the reconstructed form factors from the experimental data where only the spherical part of the charge density within each embedding sphere is updated to the reconstructed charge density. The R-factor for the spherical case is 0.64 % with a GOF of 485 - considerably worse than either

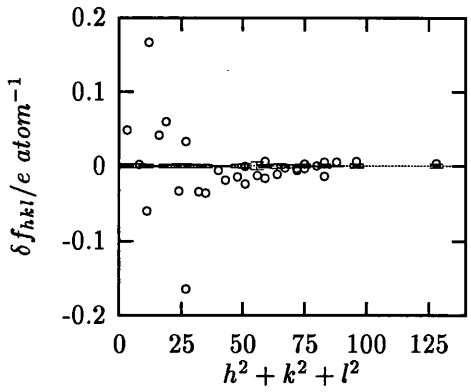

Figure 5.21: Residual error of reconstructed dynamic form factors using the spherical part of the reconstructed charge density within the embedding sphere, $f^{recon,spherical} - f^{exp}$.

the full reconstruction or FLAPW. From this data it is apparent that the correct aspherical components of the charge density are necessary for the calculation of accurate form factors.

5.6 Conclusions

In this chapter all-electron states have been reconstructed successfully from a total energy pseudopotential calculation, giving the correct charge density in the region near atomic sites that pseudopotential results cannot describe.

This reconstruction is carried out using the embedding method described in chapter 2, and the Green functions calculated in chapters 3 and 4. The reconstruction calculation itself describes the valence states scalar relativistically in a fully aspherical potential, using LAPW basis functions. The core states are calculated fully relativistically by direct solution of the Dirac equation in a spherical average of the self consistent potential. It is apparent from this that the self consistent reconstruction method itself has a lot in common with FLAPW methods.

Calculations have been carried out for Aluminium and Silicon, and the convergence of the results of these calculations with various parameters of the calculation described. Good results were obtained for both Al and Si, and the results are converged with the parameters of the embedding potential calculations carried out in chapters 3 and 4. It was found that in order to achieve convergence it was

necessary to:

- Include all bands in the Green function spectral representation for an energy cutoff of 200 eV.
- Carry out the Brillouin zone integral with 240 **k** points within the irreducible wedge.
- Sample the spectral function at $\sim$ 400 points for the convolution integral described in chapter 3.

Increasing the energy cutoff, number of **k** points or sampling of the spectral function provided no decrease in the error.

The critical parameter that limits the error of the calculation is l_{max}, the size of the embedding potential matrix. For $l_{max} = 6$ an accuracy of better than 1 % was achievable. The error is due to the higher l components of the charge density not being converged, and the $l \leq 4$ components were found to be accurate to $\sim$ 0.2 % for Al and $\sim$ 0.9 % for Si. Since only the lowest order components are required for many applications of this method (eg hyperfine structure calculations) this accuracy is probably adequate.

The reconstructed Silicon charge density has been used to derive structure factors for comparison with experimental data and recent FLAPW calculations. Comparison is good, with the reconstructed structure factor showing as good agreement with the experimental data as the FLAPW result. In addition to this the residual errors for both methods of calculation show significant correlation, indicating that they arise from the physical approximations common to both methods.

Another point addressed in this chapter is the importance of not assuming the charge density or self consistent potential are spherical. Assuming this leads to errors in the charge density of up to 30 % (see figure 5.15), and increases the errors in the structure factors by an order of magnitude.

Chapter 6

Conclusions

6.1 Overview

Total energy pseudopotential methods employing plane wave basis functions have dominated *ab initio* calculations of the structure of materials for the last 15 years, and are among the most accurate and efficient techniques available for the theoretical description and prediction of the structure of real systems. These methods excel at *structural optimisation*, that is finding the stable configuration of atoms interacting within a given system, and can be applied to a wide range of problems from simple lattices to surfaces and isolated molecules.

Unfortunately, the efficiency of the pseudopotential method relies on replacing the normal Kohn-Sham valence electrons with pseudo Kohn-Sham valence electrons, and removing the core electrons entirely. These pseudo-electrons form bonds and behave exactly as the real Kohn-Sham electrons between atoms, but act completely differently in the region near the nuclei. Consequently the structure predicted is accurate but the pseudo-electrons behave incorrectly near the nuclei.

This causes no problem provided we are interested only in the interaction of atoms with each other, since this is described accurately. However, extremely accurate crystallography (see chapter 5) allows the charge density for materials to be directly measured, requiring accurately calculated charge densities for comparison. A wide range of methods are also available for measuring the interaction of the atomic nuclei with the surrounding electrons (the hyperfine interaction - see chapter 1), which provides a focused methodology for the identification and characterisation

of the local environment of atomic nuclei in atomic and nano-scale systems. Describing the interaction of the nuclei with surrounding electrons obviously requires an accurate description of the electrons *near* the nucleus, which a pseudopotential method cannot directly provide.

This thesis describes a general method for taking the results of a pseudopotential calculation for a given system and obtaining the correct all-electron states from the pseudopotential calculation. The *reconstructed* all-electron states include correctly relaxed core states (they are not frozen to the isolated atom core states) and are as accurate as current state of the art all-electron methods (such as the Full Potential Linearised Augmented Plane Wave method, or FLAPW). In addition to this the method is applicable to far larger and more complex systems than these standard all-electron methods, since the pseudopotential method can deal with larger and more complex structural optimisation problems.

Reconstructing the correct states from the pseudo-states is a problem that has received some attention in the past, for exactly these reasons. The problem basically reduces to solving the Kohn-Sham equations for all of the electrons near a nucleus, with the boundary conditions provided at the surface of this reconstruction region by the pseudopotential calculation. For standard methods of solving boundary value problems this leads to an infinite set of coupled 2^{nd} order differential equations (non-linear due to self consistency) with an associated set of mixed boundary conditions.

Past approaches (see chapter 1) have all assumed that the self consistent potential is spherically symmetric (and in many cases the boundary conditions are also spherically averaged) in order to decouple the equations requiring solution, and so make the problem tractable. In no case has this been adequately justified, and no comparison between results produced both with and without the assumption of spherical symmetry have been presented. It is also important to note that the potential itself can deviate significantly from spherical symmetry within the region of interest.

The combination of the pseudopotential method and reconstruction procedure presented in this thesis does not require this approximation of spherical symmetry, and in essence makes the same physical and mathematical approximations as state of the art all-electron DFT methods such as the FLAPW method.

Performing the reconstruction from the results of a plane-wave basis pseudopoten-

tial calculation falls naturally into three sections, covered in chapter 2, chapters 3 & 4 and chapter 5 respectively.

6.1.1 Embedding Potential Method

In chapter 2 the *embedding potential method* is described, a method first derived by Inglesfield (1981). This method allows 2^{nd} order partial differential equations to be solved in a localised region of space. The influence of the system outside of this localised region of space (the potential outside of this region and the boundary conditions at infinity) are entirely taken into account by an *embedding potential* added to the Hamiltonian for the localised region, so the solution for the *entire* system in the localised region can be obtained from a completely *localised* calculation. Two different analytic forms for the embedding potential are given in chapter 2, in terms of the Green function of the surrounding system on the surface of the localised region. The first of these expressions has been available in the literature for some time, whilst the second is new.

This embedding approach results in some fairly subtle generalisations of localised quantum systems to extended systems. In view of this, in chapter 2 the method is applied to a new test system, the 1-D square well. This is simple enough to solve analytically and the examination of this model system sheds light on many of the properties of the embedding method. This section is particularly important for interpreting how continuum states are handled, and the importance of resonance states.

6.1.2 The Embedding Potential

Past applications of the embedding potential method have generally been limited to models where the embedding potential is that of free space, or an arbitrary model embedding potential. This is essentially due to the difficulty of obtaining an accurate real space Green function for a realistic system - the handful of cases where a Green function (and so embedding potential) have been obtained from *ab initio* calculations rely on the properties of electron structure calculations that themselves employ a Green function (more specifically the atomic sphere approximation of LMTO and KKR methods), or are inherently only applicable to a very specific problem (see the discussion in chapters 1 & 2).

In view of this it was required to develop a method for the construction of the real space Green function from the results of a total energy pseudopotential calculation, and the embedding potential from this Green function. Since no analogous construction of an embedding potential was available in the literature, the procedure was developed and analysed with the errors and convergence properties investigated carefully. Essentially it was found that in order to construct an accurate Green function (and so embedding potential) using the standard expansion of the Green function in the eigenstates of the system (the spectral representation), Bloch states for *every* energy band must be included, and at *every* **k** point - for a finite number of bands or **k** points the Green function does not possess the correct analytic form, and does not converge to the correct analytic form for increasing numbers of bands and **k** points.

This difficulty is overcome by employing a linear interpolation of the band structure in **k** space - the Linear Analytic Tetrahedron Method, or LATM - and approximating the infinite number of high energy bands that are not available as jellium states. This results in a Green function and embedding potential that will converge to the correct form and that are accurate for a realisable number of bands and **k** points. Chapters 3 & 4 describe how the Green function is calculated and the embedding potential obtained from it, together with an analysis of the convergence behaviour of the method as applied to bulk Aluminium and Silicon.

The most important conclusions of these two chapters are that it is possible to construct an accurate embedding potential from a total energy pseudopotential calculation, and that the embedding potential itself depends strongly on *all* the eigenstates of the substrate system (including the states with energies well above the Fermi energy). Although the contribution from the high energy states is less important than that from the lower energy states this contribution must still be accurate, since the potential outside of the embedding region is represented uniquely in the embedding potential by the value and normal derivative of a *complete* set of states on the surface of the embedding region (see chapter 4).

6.1.3 Reconstruction of Correct All Electron States

The final stage of the reconstruction procedure is the localised all-electron calculation carried out in the embedding region. The first part of chapter 5 describes how this is implemented. The method applied is essentially a standard DFT self-

consistent calculation, with the matrix elements evaluated over a localised region only and with the addition of the embedding potential to take into account the potential outside of the localised region.

An aspherical trial potential is taken as the starting point and from this the core electronic states are obtained using standard techniques (see chapter 5), with the valence electrons represented using LAPW-like basis functions. This method employs the LDA, scalar relativistic Kohn-Sham equations for the valence states, and a fully relativistic solution for the core states, so can be expected to provide results as accurate as state of the art FLAPW techniques provided the pseudopotential approximation is valid and the embedding potential accurate.

6.1.4 Results

Reconstructions of the core region is carried out for bulk Aluminium and Silicon. These materials were chosen as a good starting point for the development of a new calculational procedure, since their convergence behaviour in the context of pseudopotential methods is well understood. Aluminium is a jellium like metal, known to be accurately described by pseudopotential techniques, and also requires a relatively small pseudopotential calculation. Silicon is also a material whose description using pseudopotential methods is well understood and in addition to this, all-electron *ab initio* results and accurate experimental data for the charge density are also available.

Results are presented for two main types of reconstruction calculation. Firstly the reconstructed charge density is compared with the original pseudo-density at the embedding surface. These are found to agree well, with differences typically around 0.5 %.

To provide a more stringent test of the success of the whole embedding procedure, a further calculation is performed *using a pseudopotential in the embedding region.* For a successful embedding this should result in exactly the same charge density in the embedding region as for the original pseudopotential system. This is found to be the case for both Al and Si, with the 'surface error' found to be the same size for both the pseudopotential reconstruction and the all-electron reconstruction calculations. This suggests that the error is almost entirely due to the reconstruction procedure, and that the pseudopotential approximation is valid in these cases.

Another important property of the method requiring assessment is the convergence behaviour of the reconstruction calculations. The embedded reconstruction calculations themselves are found to be quick and relatively computationally cheap to perform, and convergence could be easily reached. The major computational cost of implementing the method is the evaluation of the Green function from the total energy pseudopotential results. In view of this the convergence of the reconstructed core region with the parameters of the Green function construction is investigated in some depth. The central conclusion of the analysis of the convergence behaviour is that the Green function does not need to be perfectly converged in order to obtain an accurately reconstructed core, and that if the contribution of low energy occupied states and high energy unoccupied states are dealt with separately the efficiency of the Green function construction can be greatly increased.

Finally the reconstructed charge density for Silicon has been compared with the charge density resulting from FLAPW calculations (within the LDA) and with extremely accurate experimental results for the structure factors of bulk Silicon. Silicon has received a lot of attention when it comes to determining accurate structure factors, with data available accurate to $3-5\times10^{-3}$ electrons /atom (structure factors themselves range in value from ~ 1 to ~ 11 electrons/ atom).

Comparison of these results show the reconstructed charge density to be as accurate as the FLAPW results, with significant correlation present between the residual errors of the theoretical results (reconstruction and FLAPW). This suggests that these errors are largely due to deficiencies in the LDA, in agreement with the results published by Zuo et al (1997), where different approximations for exchange-correlation effects resulted in significantly different errors, and switching the LDA to a Generalised Gradient Approximation (GGA) improved the agreement with experimental data.

6.1.5 Computational Cost and Applicability to Larger Systems

For both Aluminium and Silicon, starting with the eigenstates from the total energy pseudopotential and using a fairly modest workstation (DEC alpha 3000/600, *c.* 1995), an adequately converged embedding potential takes $\sim$ 1 h to construct, and the core reconstruction calculation itself takes $\sim$ 1/2 h. The total energy pseudopotential calculation using CASTEP took $\sim$ 1/2 hour from start to finish as

implemented here, but it should be noted that this calculation was *over* accurate in the sense that a sufficiently converged set of results could be obtained for a cheaper calculation.

An important question that has received very little attention so far is exactly how the computational cost of the reconstruction will scale with increasing system size. The reconstruction calculation itself should not become more expensive with increasing unit cell size, since it is essentially a localised calculation. Increase in unit cell size will increase the cost of obtaining the pseudo-states in the first place, and the cost of constructing the Green function and pseudopotential from these.

Provided the total energy pseudopotential calculation is of a manageable size to allow a complete (in the subspace of the plane wave basis set) set of eigenstates to be produced once self consistency is achieved (this should be possible for extremely large systems), this should not limit the size of system that can be addressed.

As discussed in chapter 4, the pseudo Green function is constructed from a spectral density function that is sampled across the range of energies where bands exist. The cost of constructing the Green function scales with number of points required to construct an accurate Green function. Since only a low energy resolution is required for the high energy unoccupied states, increasing the energy cutoff of the basis plane from 200 eV to around 1000 eV should only result in an increase of $\times 3.0$ in the time taken to construct the embedding potential. Note that this increase depends on the energy cutoff of the plane wave basis set required for the pseudopotential calculation and not the number of bands this corresponds to, hence the method should be able to handle large unit cells.

Finally the linear interpolation of the eigenstates in $\mathbf{k}$ space required to carry out the Brillouin integration could possibly cause problems in the application of the method to more complex systems. As discussed in chapter 3, band crossing and van Hove singularities do not cause any great difficulty for bulk Aluminium or Silicon. However, for more complex systems this may not be the case and even for Al and Si it may be possible to reduce the number of sample points required in the Brillouin zone by applying an integration method that avoids the complication introduced by these features.

6.2 Applications

In this thesis the reconstruction carried out for Silicon has been compared with experimental structure factors and results of FLAPW calculations, and the method performs well. A desirable future application would be the prediction of hyperfine structure, as discussed in chapter 1. As the method stands it would be applicable to the calculation of hyperfine structure, both magnetic and electrostatic, for a wide range of systems - essentially any system that can be solved for using total energy pseudopotential techniques - and would be particularly useful for systems that are too large for standard all-electron methods, such as defects in large super-cells, adsorbates on surfaces and mono-layers.

The main advantages of this method are that it results in the same accuracy as FLAPW calculations, but allows systems ~ 10 times larger to be dealt with, and the flexibility of total energy pseudopotential calculations in structural optimisation allow the reconstruction method to be applied to a wider range of problems. This combination of the strengths of the pseudopotential and all-electron methods provides the ideal tool for the explanation and prediction of hyperfine interactions in real systems.

6.3 Future Applications and Further Work

As the method stands it is directly applicable to more complex systems using the super-cell approach. However, it is possible that some aspects of the calculation will require improvement for particular systems, and it may be possible to improve the efficiency of the calculation.

The most expensive part of the calculation is the construction of the Green function using the spectral representation, which not only takes up time in itself, but requires all of the bands from the total energy calculation (ie the same number of bands as plane wave basis functions in the total energy calculation). At first sight this seems like an over-description of the problem, since the unoccupied bands should be unimportant. But, it turns out that a knowledge of all the bands is strictly necessary in order to characterise the substrate potential by the eigenstates (and normal derivative) on a bounding surface of the substrate region.

The contribution to the Green function in the region of interest, below the Fermi energy, is dominated by the low energy eigenstates. The contribution from the infinite high energy bands is important, but takes a simple functional form (see chapter 4). In light of this it would be desirable to derive an expression for the contribution from the unoccupied energy bands to the spectral representation explicitly in terms of the *substrate potential* itself, removing the requirement for a full matrix diagonalisation to be carried out once self-consistency has been achieved in the total energy calculation. If this proves to be possible then only the occupied bands would be required in order to obtain a valid embedding potential, and the embedding potential method itself would be far easier to apply to a wide range of problems. A recent paper by Ness and Fisher (1997) may provide a way to implement this, as they discuss a method for *iteratively* obtaining a Green function without applying the spectral representation.

The Brillouin zone integral described in chapter 3 for the evaluation of the spectral representation may require further attention for more complex systems. The band crossing effects, and the misrepresentation of van Hove singularities in the band structure are not important for the relatively simple systems examined in this thesis, but more care may be required for larger systems. Many past workers who have carried out similar Brillouin zone integrals have found the success of different methods can depend quite strongly on the specific properties of the material being investigated. If a more efficient method was required an extrapolative, higher order scheme would probably be the best candidate, as discussed by Pickard (1997).

Prediction of hyperfine structure and comparison with other methods would also be a desirable next step. FLAPW results are available for some materials (Blaha et al (1996); Dufek et al (1995); see discussion in chapter 1) and reproducing these results for comparison would provide an important further test of the success of the reconstruction method.

In addition to the specific problem of core reconstruction, the method for calculating the Green function and embedding potential from a set of eigenstates of a system could be applied to other problems. Examples of the type of problem include substitution of defect systems into lattices, or isolated adsorbates onto surfaces, hence avoiding the super-cell geometry required for the direct application of the lattice methods.

In summary, an accurate method has been developed for the construction of real space Green functions from plane wave pseudopotential calculations, which could

be generalised to other basis sets. The embedding method of Inglesfield (1981) has been implemented using this Green function, and the pseudopotential method successfully extended to provide all-electron results with the same accuracy as FLAPW calculations.

Appendix A

Symmetrisation Matrices

Aluminium possesses a symmorphic space group, O_h^5, which results in the general set of 48 equivalent points in real space given below

$$
\begin{array}{cccccc}
x,y,z & z,x,y & y,z,x & x,z,y & y,x,z & z,y,x \\
x,\overline{y},\overline{z} & z,\overline{x},\overline{y} & y,\overline{z},\overline{x} & x,\overline{z},\overline{y} & y,\overline{x},\overline{z} & z,\overline{y},\overline{x} \\
\overline{x},y,\overline{z} & \overline{z},x,\overline{y} & \overline{y},z,\overline{x} & \overline{x},z,\overline{y} & \overline{y},x,\overline{z} & \overline{z},y,\overline{x} \\
\overline{x},\overline{y},z & \overline{z},\overline{x},y & \overline{y},\overline{z},x & \overline{x},\overline{z},y & \overline{y},\overline{x},z & \overline{z},\overline{y},x \\
\overline{x},\overline{y},\overline{z} & \overline{z},\overline{x},\overline{y} & \overline{y},\overline{z},\overline{x} & \overline{x},\overline{z},\overline{y} & \overline{y},\overline{x},\overline{z} & \overline{z},\overline{y},\overline{x} \\
\overline{x},y,z & \overline{z},x,y & \overline{y},z,x & \overline{x},z,y & \overline{y},x,z & \overline{z},y,x \\
x,\overline{y},z & z,\overline{x},y & y,\overline{z},x & x,\overline{z},y & y,\overline{x},z & z,\overline{y},x \\
x,y,\overline{z} & z,x,\overline{y} & y,z,\overline{x} & x,z,\overline{y} & y,x,\overline{z} & z,y,\overline{x}
\end{array}
$$

The origin is taken to be at the $(m3m)$ symmetry point.

These 48 points can be constructed from unitary transformations of x, y, z, by using a combination of rotations, mirrors and inversions. The expression for the space group operator that transforms x, y, z to the equivalent points takes the form

$$P = I^{n_1} R(001;\pi)^{n_2} R(010;\pi)^{n_3} R(111;2\pi/3)^{n_4} M(001)^{n_5}$$
$$n_1, n_2, n_3, n_5 = 0, 1 \text{ and } n_4 = 0, 1, 2 \tag{A.1}$$

where $R(l_1 l_2 l_3;\theta)$ denotes a rotation of angle θ about an axis in the direction $(l_1 l_2 l_3)$ and through the origin, I denotes inversion through the origin and $M(l_1 l_2 l_3)$ denotes reflection in the plane perpendicular to $(l_1 l_2 l_3)$ and passing through the origin. The powers (n_1, n_2, n_3, n_4 and n_5) denote how many times each operation is applied.

We require these transformations in a spherical harmonic representation to obtain the transformation matrices $\mathcal{U}^{(P)}$ used in chapter 3. The transformations for a spherical harmonic basis are given by (Wigner, 1959)

$$I_{LL'} = \delta_{ll'}\delta_{mm'}(-1)^l \tag{A.2}$$

$$R(001;\theta)_{LL'} = \delta_{ll'}\delta_{mm'}e^{im\theta} \tag{A.3}$$

$$R(010;\theta)_{LL'} = \delta_{ll'}\sum_t (-1)^t \frac{[(l+m)!(l-m)!(l+m')!(l-m')!]^{\frac{1}{2}}}{(l+m-t)!(l-m'-t)!t!(t-m+m')!}$$
$$\times \left[\cos\frac{\theta}{2}\right]^{2l+m-m'-2t} \left[\sin\frac{\theta}{2}\right]^{2t-m+m'} \tag{A.4}$$

where the sum over t is over all values where the arguments of the factorials are non-negative. $M(001)$ and $R(111;2\pi/3)$ can be constructed from these transformations, hence this allows us to construct the matrices $\mathcal{U}^{(P)}$.

For non-symmorphic symmetry we calculate the matrices in the same way except the unitary transformation associated with different translation vectors within the point group are handled separately, as described in chapter 3.

Bibliography

Abramowitz M and Stegun I A 1964 *Handbook of Mathematical Functions* (Washington D.C.: U.S. Government Printing Office)

Aldred P J E and Hart M 1973 *Proc. R. Soc. A* **332** 223

Allen R E and Menon M 1986 *Phys. Rev. B* **33** 8 5611

Altmann S L 1991 *Band Theory of Solids: An Introduction from the Point of View of Symmetry* (Oxford: Oxford University Press)

Anderson O K 1975 *Phys. Rev. B* **12** 3060

Andriotis A N 1990 *J. Phys.: Condens. Matter* **2** 1021

Andriotis A N 1992 *Europhys. Lett.* **17** 4 349

Bachelet G B, Hamann D R and Schlüter 1982 *Phys. Rev. B* **26** 8 4199

Battoceli M , Ebert H and Akai H 1996 *Phys. Rev. B* **53** 15 9776

Benesh G A and Inglesfield J E 1984 *J. Phys. C: Solid State Phys.* **17** 1595

Bellaiche L and Kunc K 1997 *Phys. Rev. B* **55** 8 5006

Blaha P, Schwarz K and Dederichs P H 1988 *Phys. Rev. B* **37** 2792

Blaha P, Dufek P, Schwarz K and Haas H 1996 *Hyperfine Interactions* **97/98** 3

Blöchl P E 1994 *Phys. Rev. B***50** 24 17953

Boero M, Pasquarello A, Sarnthein J and Car R 1997 *Phys. Rev. Lett.* **78** 5 887

Boon M H, Methfessel M S and Mueller F M 1986 *J. Phys. C: Solid State Phys.* **19** 5337

Braspenning P J, Zeller R, Lodder A and Dederichs P H 1984 *Phys. Rev. B* **29** 2 703

Brownstein K R 1995 *J. Math. Phys.* **36** 1 76

Broyden C G 1965 *Math. Comput.* **19** 577

Ceperly D M and Alder B J 1980 *Phys. Rev. Lett.* **45** 566

Chadi D J and Cohen M L 1973 *Phys. Rev. B* **8** 5747

Chen A 1977 *Phys. Rev. B* **16** 8 3291

Cooke J F and Wood R F 1973 *Phys. Rev. B* **7** 2 893

Crampin S, van Hoof J B A N, Nekovee M and Inglesfield J E 1992 *J. Phys.: Condens. Matter* **4** 1475

Cummings S and Hart M 1988 *Aust. J. Phys.* **41** 423

Davis P J and Rabinowitz P 1967 *Numerical Integration* (New York: Academic Press)

Deutsch M 1992 *Phys. Rev. B* **45** 2 646

Dufek P, Blaha P and Schwarz K 1995 *Phys. Rev. Lett.* **75** 19 3545

Economou E N 1990 *Green's Functions in Quantum Physics* (Berlin: Springer-Verlag)

Ehmann J and Fähnle M 1997 *Phys. Rev. B* **55** 12 7478

Fisher A J 1988 *J. Phys. C: Solid State Phys.* **21** 3229

Fisher A J 1990 *J.Phys.: Condens. Matter* **2** 6079

Fuchs M, Bockstedte M, Pehlke E and Scheffler M 1998 *Phys. Rev. B* **57** 4 2134

Ganduglia-Pirovano M V , Kudrnovsky J and Scheffler M 1997 *Phys. Rev. Lett.* **78** 9 1807

Garcia-Moliner F and Rubio J 1969 *J. Phys. C: Solid State Phys.* **2** 1789

Gardner J R and Holzwarth N A W 1986 *Phys. Rev. B* **33** 10 7139

Gemperle C and Schweiger A 1991 *Chem. Rev.* **91** 1481

Gilat G 1972 *J. Comp. Phys.* **10** 432

Gilat G 1973 *Phys. Rev. B* **7** 2 891

Gilat G 1976 *Methods Comp. Phys.* **15** 317

Goringe C M, Bowler D R and Hernández E 1997 *Rep. Prog. Phys.* **60** 1447

Grant I P, McKenzie B J, Norrington P H, Mayers D F and Pyper N C 1980 *Comput. Phys. Commun.* **21** 207

Guo G Y and Ebert H 1996 *Phys. Rev. B* **53** 5 2492

Hahn T (Ed.) 1995 *International Tables for Crystallography: Vol. A Space-group symmetry* (Dordrecht: Kluwer Academic Publishers)

Hedin L and Lundquvist B 1971 *J. Phys. C* **4** 2064

Hohenberg P and Kohn W 1964 *Phys. Rev.* **136** B864

Holzwarth N A W, Matthews G E, Dunning R B, Tackett A R and Zeng Y 1997 *Phys. Rev. B* **55** 4 2005

Illgner M and Overhof H 1996 *Phys. Rev. B* **54** 4 2505

Inglesfield J E 1971 *J. Phys. C: Solid State Phys.* **4** L14

Inglesfield J E 1981 *J. Phys. C: Solid State Phys.* **14** 3795

Inglesfield J E 1981 *J. Phys. F: Metal Phys.* **11** L287

Inglesfield J E 1996 Private Communication

Ishida H 1997 *Surface Science* **388** 71

James R and Woodley S M 1996 *Solid State Commun.* **97** 11 935

Jepson O and Anderson O K 1971 *Solid State Commun.* **9** 1763

Johnson D D 1988 *Phys. Rev. B* **38** 18 12807

Jones R O and Gunnarsson O 1989 *Rev. Mod. Phys.* **61** 3 689

Kaprzyk S and Mijnarends P E 1986 *J. Phys. C: Solid State Phys.* **19** 1283

Katayama-Yoshida H and Hamada N 1987 *Phys. Rev. B* **35** 1 407

Kaufmann E N and Vianden R J 1979 *Rev. Modern Phys.* **51** 1 161

Kerker G P 1980 *J. Phys. C: Solid State Phys.* **13** L189

Koelling D D and Arbman G O 1975 *J. Phys. F: Metal Phys.* **5** 2041

Koelling D D and Harmon B N 1977 *J. Phys. C: Solid State Phys.* **10** 3107

Kohn W and Rostocker N 1954 *Phys. Rev. B* **94** 111

Kohn W and Sham L J 1965 *Phys. Rev.* **140** 1133A

Korringa J 1947 *Physica* **13** 392

Krasovskii E E 1997 *Phys. Rev. B* **56** 20 12866

Kuzmiak V, Zavadil J and Ždánský K 1991 *Phys. Stat. Sol. (b)* **168** 547

Lambin Ph and Vigneron J P 1984 *Phys. Rev. B* **29** 6 3430

Lauer S, Marathe V R and Trautwein A 1979 *Phys. Rev. A* **19** 5 1852

Lehman G and Taut M 1972 *Phys. Stat. Sol. (b)* **54** 469

Lu Z W, Zunger A and Deutsch M 1993 *Phys. Rev. B* **47** 15 9385

MacDonald A H, Vosko S H and Coleridge P T 1978 *J. Phys. C: Solid State Phys.* **12** 2991

Madelung O 1996 *Introduction to Solid State Theory* (Berlin: Springer-Verlag)

Methfessel M S, Boon M H and Mueller F M 1987 *J. Phys. C: Solid State Phys.* **20** 1069

Methfessel M S, Rodriguez C O and Anderson O K 1989 *Phys. Rev. B* **40** 3 2009

Methfessel M S and Frota-Pessô S 1990 *J. Phys.: Condens. Matter* **2** 149

Meyer B, Hummler K, Elsässer C and Fähnle M 1995 *J. Phys.: Condens. Matter* **7** 9201

Miller N C, Lee P M and Inglesfield J E 1985 *Phil. Mag. B* **51** 2 199

Mitchell D W, Das T P, Potzel W, Schiessel W, Karzel H, Steiner M, Köfferlein M, Hiller U, Kalvius G M, Martin A, Schäfer W, Will G, Halevy I and Gal J 1996 *Phys. Rev. B* **53** 12 7684

Monkhorst H J and Pack J D 1976 *Phys. Rev. B* **13** 12 5188

Montalenti F, Trioni M I, Brivio G P and Crampin S 1996 *Surface Science* **364** L595

Morse P M and Feshbach H 1953 *Methods of Theoretical Physics* (New York: Plenum Press)

Müller J E and Wilkins J W 1984 *Phys. Rev. B* **29** 8 4331

Nesbet R K *Phys. Rev. B* **30** 8 4230

Ness H and Fisher A J 1997 *J. Phys.: Condens. Matter* **9** 1793

Ness H and Fisher A J 1997 *Phys. Rev. B* **56** 19 12469

Noguera C 1990 *Phys. Rev. B* **42** 3 1629

Parr R G and Yang W 1989 *Density-Functional Theory of Atoms and Molecules* (Oxford: Oxford University Press)

Payne M C, Teter M P, Allan D C, Arias T A and Joannopoulos J D 1992 *Rev.*

Modern Phys. **64** 4 1045

Pendry J B, Prêtre A, Rous P J and Matín-Moreno L 1991 *Surface Science* **244** 160

Perdew J P and Zunger A 1981 *Phys. Rev. B* **43** 7312

Petrilli H M and Frota-Pessôa 1990 S *J. Phys.: Condens. Matter* **2** 135

Petrilli H M, Blöchl P E, Blaha P and Schwarz K 1998 *Phys. Rev. B* **57** 23 14690

Pickard C J 1997 *Ab Initio Electron Energy Loss Spectroscopy* Phd Thesis, Cambridge University

Press W H, Teukolsky S A, Vetterling W T and Flannery B P 1994 *Numerical Recipes* (Cambridge: Cambridge University Press)

Rath J and Freeman A J 1975 *Phys. Rev. B* **11** 6 2109

Robertson I J and Payne M C 1990 *J. Phys.: Condens. Matter* **2** 9837

Saka T and Kato N 1986 *Acta Crystallogr. A* **42** 469

Schiff L I 1955 *Quantum Mechanics* (New York: McGraw-Hill)

Seeger A, Ehmann J and Fähnle M 1996 *Z. Naturforsch.* **51a** 489

Sher A, van Schilfgaarde M and Bending M A 1991 *J. Vac. Sci. Tecnol. B* **9** 3 1738

Simon B 1972 *Ann. Math.* **97** 247

Spence J C H 1993 *Acta. Cryst.* A**49** 231

Sternheimer R M 1986 *Z. Naturforsch* **41a** 24

Takeda T and Kübler J 1979 *J. Phys. F: Metal Phys.* **9** 4 661

Taylor J R 1972 *Scattering Theory* (New York: John Wiley & Sons, Inc.)

Teworte R and Bonse U 1984 *Phys. Rev. B* **29** 2102

Trioni M I, van Hoof J B A N, Crampin S, Brivio G P and Inglesfield J E 1994 *Surface Science* **309** 41

Trioni M I, Brivio G P, Crampin S and Inglesfield J E 1996 *Phys. Rev. B* **53** 12 8052

Vackář J and Šimůnek A 1994 *J. Phys.: Condens. Matter* **6** 3025

Vosko S H, Wilk L and Nusair M 1980 *Can. J. Phys.* **58** 1200

Weihrich H and Overhof H 1996 *Phys. Rev. B* **54** 7 4680

Wigner E P 1959 *Group Theory* (New York: Academic Press)

Wigner E P 1938 *Trans. Faraday Soc* **34** 678

Williams A R, Feibelman P J and Lang N D 1982 *Phys. Rev. B* **26** 10 5433

Woodley S M 1997 *A Real-Space Approach to Surface and Defect States* Phd Thesis, University of Bath

Wei S and Zunger A 1997 *J. Chem. Phys.* **107** 6 1931

Yaris R and Winkler P 1978 *J. Phys. B: Atom. Molec. Phys.* **11** 8 1475

Zuo J M, Blaha P and Schwarz K 1997 *J. Phys.: Condens. Matter* **9** 7541